Describing and Comparing Variability of Fish and Macrozooplankton Density at Marine Hydrokinetic Energy Sites

Dale A. Jacques II

A thesis

submitted in partial fulfillment of the

requirements for the degree of

Master of Science

University of Washington

2014

Committee:

Dr. John K. Horne

Dr. Sandra Parker-Stetter

Dr. Christian Torgerson

Dr. John R. Skalski

Program Authorized to Offer Degree:

Aquatic and Fishery Sciences

University of Washington

Abstract

Describing and Comparing Variability of Fish and Macrozooplankton Density at Marine Hydrokinetic Energy Sites

Dale A. Jacques II

Chair of Supervisory Committee:
Dr. John K. Horne
Aquatic and Fisheries Sciences

Marine hydrokinetic (MHK) operating licenses require biological monitoring to quantify effects of devices on aquatic organisms, but regulations for instrumentation, measurements, and sampling effort have not been standardized. Assuming stationary acoustic surveys are more cost effective than repeated mobile surveys, the abilities of stationary echosounders, ADCPs, and acoustic cameras to characterize fish densities were compared at a MHK site in Admiralty Inlet, WA. The calibrated echosounder was most sensitive to density changes from vertical migrations, and state-space models confirmed measurements were robust to other variance sources including tidal currents. Peak density variance occurred at a 24-hour period, with cyclic fluctuations in phase with tidal currents and tidal ranges. Six methods used mobile acoustic data to estimate representative spatial ranges of stationary acoustic measurements, resulting in values from 31 to 1,388 m. Design objectives were used to develop a generic framework for the design of distributed monitoring networks at MHK sites.

TABLE OF CONTENTS

LIST OF TABLES

LIST OF FIGURES

Acknowledgements

The following thesis was made possible only through the generous support of many friends, colleagues, teachers, and funding sources. In particular I would like to thank the Fisheries Acoustics Research Lab at the University of Washington, including Beth Phillips, Lauren Wiesebron, Ian Fraser, Emily Runnells, and Sam Urmy, for the constant support and a never-ending stream of new ideas and constructive critiques. I am also thankful to Dave McGowan for endless whiteboard talks and constant encouragement and guidance, regardless of the circumstance. I am convinced that Jen Nomura is Super Woman, and this project would not have been possible without her attention to detail and countless hours of help, both at sea and in the lab. David Barbee never ceased to amaze me with his clever engineering and his uncanny penchant for troubleshooting every problem we encountered. Finally, many thanks to Hannah Linder for help programming and preparing reports.

I am also grateful for the help provided by people affiliated with the University of Washington, including Captain Mark Anderson, Dr. David Duggins, and the crew of the RV Centennial. I am grateful to Brian Polagye and the Northwest National Marine Renewable Energy Center for designing, deploying, and retrieving the stationary acoustic pods and providing travel funding. Many thanks are due to Dr. Eli Holmes, Dr. Mark Scheuerell, Dr. Eric Ward, and Dr. Don Percival for their input and suggestions at various points in the data analysis.

I am also thankful to my committee, including Dr. Christian Torgersen, Dr. John Skalski, and Dr. Sandy Parker-Stetter. Special thanks to Dr. Sandy Parker-Stetter, for always offering an open door, open ears, patience, guidance, and the occasional breakfast. The vision behind this project belongs to my advisor, Dr. John Horne, who took the time and energy to foster this project and help me grow in my personal life as much as my professional life.

Funding for this project was provided by the National Oceanic Partnership Program and the Bureau of Ocean Energy Management. Thanks to BioSonics, Sound Metrics, and Teledyne-Reson for supplying the acoustic instruments used for testing.

Finally, to my family. You've been supportive through the toughest of times and celebrate with me in the best of times. With much love, thank you.

Chapter 1. Spatio-Temporal Biological Monitoring at Marine Hydrokinetic Energy Sites

1.1. Introduction

Ecological communities vary over ranges of spatial and temporal scales (Stommel 1963, Haury et al. 1978, Levin 1992). Historically, ecological variability was treated as a statistical nuisance that limited efforts to identify change in a quantity through space and/or time (Horne & Schneider 1995). A series of papers disseminated the importance of variance as an ecologically significant quantity (Wiens 1989, Levin 1992, Horne & Schneider 1995). Scale-dependent patterns of variance can be used to infer the underlying physical and biological processes influencing an ecosystem (Platt & Denman 1975, Steele 1994, Horne & Schneider 1995), but the ability to identify these patterns is limited by the sampling resolution relative to the extent of a survey (*i.e.* measurement scope; Wiens 1989, Schneider 2009). Even though interpretation of biological variance has become more nuanced, constraints on data storage and processing have historically limited the spatial and temporal scope of ecological surveys (Dickey & Bidigare 2005). Recent technological advancements have enabled fine-resolution (spatial resolution < 1m, temporal resolution < 1 sec), spatiotemporal measurements over months or years (*e.g.* Dickey & Bidigare 2005, Urmy et al. 2012), which were not previously possible (Porter et al. 2005). Surveys conducted at high spatial and temporal scope also enable the identification of transient temporal processes in space (*e.g.* Certain et al. 2007). In reality, repeated high-scope, mobile surveys, such as line-transects, are cost prohibitive to repeat at the temporal resolution required to characterize temporal patterns operating at daily or monthly periods. Sampling through space takes time, convolving spatial and temporal variability, further obscuring the detection of temporal patterns (Stewart-Oaten et al. 1995, Martin et al. 2005). An operational sampling tradeoff between spatial and temporal scope must be made, which may compromise the identification of spatial or temporal patterns through time (*e.g.* Lie et al. 2013).

In contrast to repeated mobile surveys, networks of static, autonomous sensors may be more cost effective to provide high-temporal scope measurements in space and time. Stationary sensor networks are particularly effective for sampling marine environments over months or years due to the expense of repeating mobile surveys at sea. The cost effectiveness of remote monitoring methods are particularly attractive for prolonged studies, such as environmental impact assessments (Brando & Phinn 2007). A recent application requiring long term environmental monitoring is marine hydrokinetic energy (MHK) installations. MHK is a suite of technologies that generate electricity from the kinetic energy of

surface waves, offshore wind, and tidal currents. As MHK technologies progress toward economic viability, dynamic, energy-rich sites are being developed for demonstration projects (*i.e.* one to ten devices) with the intent of scaling pilot project sites to large commercial arrays (*i.e*. tens to hundreds of devices).

The ecological effects of generating electricity in the marine environment on mammals, fish, and macrozooplankton (*i.e.* pelagic nekton) are uncertain. Hypothesized effects of MHK devices on local pelagic nekton communities include direct strikes or impingement (APBmer 2010), repulsion due to operational noise (Halvorsen et al. 2011) or electro-magnetic fields (Öhman et al. 2007, Normandeau 2011), or aggregation as a shelter from predators and tidal currents (*e.g.* artificial reefs or fish aggregation devices; Inger et al. 2009, Polagye et al. 2011). In the United States, MHK operating licenses require monitoring programs to quantify potential environmental effects (FERC 2008), but monitoring requirements and the sample designs have not been standardized, and there are no recommended analytic procedures to design monitoring programs.

The high kinetic energy that makes sites attractive for MHK development also poses challenges to traditional marine sampling techniques. Sampling uncertainties arise at nearly every phase in the design of monitoring programs, including:

1. Choice of instrumentation to measure nekton density through the water column that is robust to sampling in energetic environments
2. Selection of metrics to describe change in the pelagic nekton community that are compatible with the instrumentation
3. Design of platforms and instrumentation density that optimize monitoring sensitivity and cost effectiveness
4. Determining minimum sampling effort that provides adequate sample coverage and statistical power
5. Defining analytic tools to compare baseline measurements to post-installation measurements to quantify the presence and amplitude of biological effects

This study addresses these five uncertainties when developing a biological monitoring plan for MHK installations, and provides a framework to construct monitoring plans. To illustrate the approach and to

resolve these challenges, data from the Snohomish Public Utility District's proposed tidal MHK pilot site in Admiralty Inlet, Puget Sound, WA was used as a case study.

Chapter 2: Active Acoustic Characterization of Pelagic Communities at a Tidal Marine Hydrokinetic Energy Site

2.1. Introduction

Offshore energy resources, such as waves, tidal currents, and offshore wind, are emerging as an economically viable form of carbon-free renewable energy. Marine hydrokinetic energy (MHK) installations convert kinetic energy in waves and tidal currents to electricity, but the biological impact of generating electricity in marine environments is uncertain (Boehlert & Gill 2010, Wilson et al. 2010, Frid et al. 2012). Hypothesized effects of installing and operating MHK devices on the fish and macro-zooplankton (*i.e.* nekton) community include reductions in density due to direct strike or impingement (Wilson et al. 2007, ABPmer 2010), changes in the vertical and horizontal distribution due to noise (Halvorsen et al. 2011), electro-magnetic fields (Öhman et al. 2007, Normandeau 2011), or sheltering from tidal currents (*e.g.* artificial reefs; Inger et al. 2009, Polagye et al. 2011). The strong tides and waves that make sites attractive for MHK developments constrain traditional forms of biological sampling, such as nets, cameras, and optical surveys. These challenges historically made these sites difficult or impossible to sample, creating a gap in knowledge of the local biological community and how it varies through time and space. Uncertainty in the rate and severity of effects of a MHK device is compounded by uncertainty in the density and distribution of nekton. The lack of historical sampling has led to a dearth of baseline knowledge on species composition, density, distribution, and variability of nekton communities at MHK sites needed to make informed decisions about monitoring instrumentation, metrics, and effort. Despite these sampling challenges and the lack of biological understanding, government regulations require MHK developers to monitor the effects of installing, operating, and decommissioning MHK devices (FERC 2008).

In contrast to near-field monitoring, which observes direct interactions between organisms and a device, far-field or domain monitoring quantifies effects of a device or devices on the ecological community. An effect is defined as a statistically significant deviation in a biologically pertinent quantity of the community, determined by comparing pre-installation to post-installation measurements (Smith 1991). When comparing pre- and post-installation measurements, the power to statistically identify biological effects is confounded by natural variability in quantities of interest (Underwood 1989, Morrisey 1993, Hewitt et al. 2001). Baseline variability must be characterized to calculate the minimum detectable effect and properly allocate sampling effort through space and time (Rhodes & Jonzén, 2011). Variability is not

merely a statistical impedance (Horne & Schneider 1995); variability is a biologically significant attribute of a quantity that can be used as a secondary indicator of change (Underwood 1991).

Active acoustics are a suite of non-invasive aquatic sampling technologies that measure fish and macrozooplankton (*i.e.* nekton) density at fine spatial and temporal resolutions. Since light is scattered and absorbed more quickly than sound in water, acoustic technologies have longer effective sampling ranges than optical devices and are more robust to turbid environments. Traditionally, acoustic measurements have been collected from mobile surface vessels (*e.g.* Koslow 2009) to quantify spatial distributions of fish and macrozooplankton. The constraint when measuring spatial heterogeneity in mobile surveys is that sampling space takes time, confounding temporal and spatial variability. Repeating mobile surveys enables the allocation of variance between time and space, but the rate at which mobile surveys can be repeated, which defines the temporal resolution of the data set, is resource limited. Identification of temporal patterns from repeated mobile surveys is constrained by the temporal resolution relative to the temporal extent (*i.e.* temporal scope; Wiens 1989, Schneider 2009) of the data. Recent innovations in power and data storage facilitate the remote deployment of acoustic instruments from stationary ocean observatories, which can be used to quantify temporal variability in nekton density and vertical distribution at high temporal resolution (*e.g.* Urmy et al. 2012). In contrast to mobile acoustic surveys, stationary acoustic surveys measure density and vertical distribution of nekton at a high temporal scope, but in a reduced volume. Based on current MHK monitoring plans (*e.g.* NYSERDA 2011), stationary acoustic surveys are assumed to be preferred for long-term, post-installation domain monitoring due to the added costs of maintenance, fuel, and labor associated with vessel operation in repeated mobile surveys.

Ideally, acoustic technologies deployed for other objectives, such as tidal resource characterization or near-field monitoring, could be used for domain monitoring, reducing monitoring costs by decreasing the number of deployed instrument packages. Several acoustic technologies may be opportunistically available for domain monitoring at MHK sites, but there is a need to vet these technologies against the community standard: calibrated scientific echosounders (Foote et al. 1987, Simmonds & MacLennan 2005). In particular, Acoustic Doppler Current Profilers (ADCP) and acoustic

cameras have been deployed at MHK installations to characterize tidal resources and to track fish as they approach a turbine (Polagye & Thomson 2013, Viehman & Zydlewski 2014).

The primary challenge when designing MHK domain monitoring programs is to identify instrumentation and metrics that can measure nekton densities in energetic environments, maintain cost effectiveness, and are capable of being deployed over extended periods. This study, conducted at a proposed tidal current MHK pilot site in Admiralty Inlet, Puget Sound, WA provides a case study to evaluate acoustic technologies for monitoring densities and vertical distributions of nekton over time and space at MHK sites. To inform future efforts to monitor pelagic communities, including the pilot MHK site in Admiralty Inlet, specific objectives of this chapter are:

1. To characterize species composition, biological diversity, and to identify species of special regulatory concern.
2. To describe spatial and temporal variability in the density and vertical distribution of fish and macrozooplankton in the water column.
3. To identify potential physical processes influencing those patterns, and events of exaggerated biological variability that may pose a risk to either the device or biological community as a whole.
4. To compare the efficacy of an ADCP, an acoustic camera, and a calibrated echosounder to measure nekton density and vertical distribution.

Taken collectively, these objectives form a baseline characterization of pelagic nekton in Admiralty Inlet, WA as a standard to compare to post installation measurements as part of biological monitoring plan.

2.2. Materials & Methods

2.2.1 Overview

Species composition, density, and distribution of the pelagic nekton community are characterized using stationary and mobile acoustic surveys, supplemented by midwater trawls, at the Snohomish Public Utilities District's (SnoPUD) proposed tidal energy site in Admiralty Inlet, Puget Sound. Admiralty Inlet is a shallow shelf connecting Puget Sound to the Strait of Juan de Fuca and the primary inlet into Puget Sound (Figure 2.1). The proposed site is 750m from Admiralty Head at a depth of 55m at mean tide level.

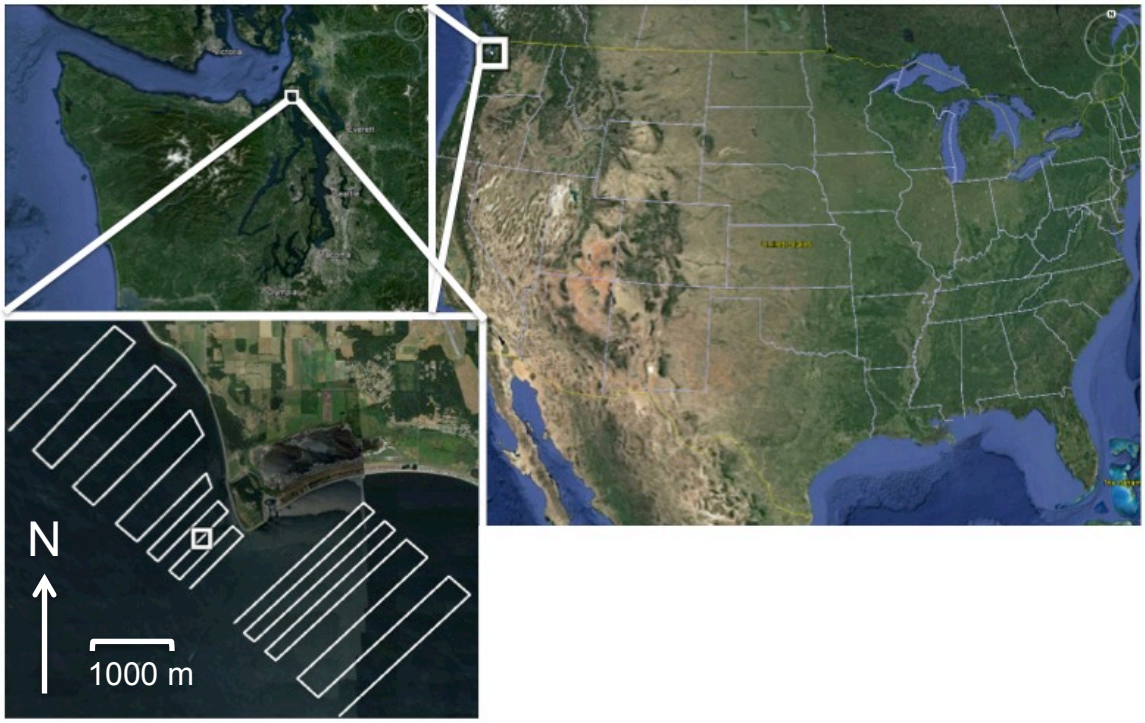

Figure 2.1. Admiralty Inlet, Puget Sound, USA. (top left) Admiralty Inlet at the mouth of Puget Sound. (bottom left) the location of the stationary echosounder, at a proposed tidal energy pilot site, is denoted by the white square in relation to the two spatial grids north and south of the stationary package, each consisting of high and low resolution transects.

Tidal flows in excess of 3.5 m/s have been observed through Admiralty Inlet (Gooch et al. 2009). Previous efforts to catalogue fish in Admiralty Inlet have observed 115 species (DeLacy et al. 1972), including 11 species of special conservation status as defined by state and federal agencies (WDFW 2012). Snohomish Public Utility District has proposed installing two six-meter OpenHydro (www.openhydro.com) tidal current turbines on three-meter foundations in Admiralty Inlet in the summer of 2015.

2.2.2 Acoustic Technology Description

Active acoustics are a diverse set of technologies capable of quantifying densities and vertical distributions of aquatic organisms, characterizing tidal flow regimes, and tracking individual targets through space in aquatic environments (Simmonds and MacLennan, 2005). In general, acoustic technologies emit short (*e.g.* 0.2 - 1ms) pulses of energy (*i.e.* a ping) through the water column at high rates (*e.g.* > 1 sec^{-1}). The emitted sound is reflected by fish and macroinvertebrate targets in the water column back to the transceiver. These reflections, called acoustic backscatter, are used to enumerate or track individual targets through space and time (Simmonds & MacLennan 2005), while the integral of backscatter is used to estimate nekton density (Foote 1983). The fine temporal and vertical resolution (< 1m) of samples from acoustic instruments enable high-resolution measurements of nekton densities distributed throughout the water column (*i.e.* density distributions).

2.2.2.1 Echosounders

Calibrated scientific echosounders are used to measure pelagic nekton density-distributions from mobile (*e.g.* Koslow 2009) or stationary platforms (*e.g.* Doksaeter et al. 2009, Kaartvedt et al. 2009, Urmy et al. 2012). Internationally accepted calibration protocols (Foote et al. 1987) ensure consistent operation and data equivalency among echosounders, surveys, and years. Given the number of validation studies and use by the international community (*e.g.* Love 1971, Nakken & Olsen 1977, Foote 1983, Simmonds & MacLennan 2005), the scientific echosounder is the most vetted acoustic instrument and was used as a benchmark to compare the efficacy of other acoustic technologies in this study.

2.2.2.2 Acoustic Cameras

Acoustic cameras operate at high frequencies (*e.g.* 0.7 to 1.8 MHz) and provide near optical quality images that are used for imaging, counting, and inspection of objects or aquatic organisms

(Simmonds & MacLennan 2005). The added resolution of acoustic cameras comes at the cost of operational range (*e.g.* 15 to 80m). Yet even this range, short by acoustic standards, exceeds that of optical technologies when used in aquatic environments. Stationary acoustic cameras have been used to count migrating salmon (*e.g.* Burwen et al. 2010) and to track individual targets as they approached a tidal turbine (*e.g.* Viehman & Zydlewski 2014). The ability of acoustic cameras to track individual targets at high resolution and precision in turbid water makes them an attractive component of many near-field MHK monitoring programs, providing the ability to detect physical strikes or impingements of individual fish as they approach a MHK device. The use of acoustic cameras in near-field monitoring makes them opportunistically available for domain monitoring at MHK sites, but the accuracy of integrated acoustic backscatter measures of nekton density by acoustic cameras has not been tested.

2.2.2.3 Acoustic Doppler Current Profilers

The ADCP uses the shift in returned frequency due to the movement of suspended passive particles (*i.e.* the Doppler effect) to derive water velocities. Water velocities, collected through time from bottom deployed ADCPs, are used to determine the site feasibility for MHK tidal current installations (Polagye & Thomson 2013). Even though ADCPs were designed to measure current velocities, the returned backscatter can be used as an index of nekton biomass (*e.g.* Flagg et al. 1994, Cochrane et al. 1994, Brierley et al. 2006). The difficulty of calibrating an ADCP for biological use (Brierley et al. 1998) limits the interpretation of backscatter to a relative index.

2.2.3 Mobile Survey

2.2.3.1 Mobile Acoustics

Snohomish Public Utilities District's (SnoPUD) proposed Admiralty Inlet tidal hydrokinetic energy site was split into north and south geographic areas, approximately 1km apart. The north geographic area was located in the main tidal channel, while the south geographic area was shielded from flood tides by Admiralty Head (Figure 2.1). Each geographic area was repeatedly sampled by a systematic acoustic survey, consisting of high (0.25 km) and low (0.5 km) resolution transects encompassing the proposed location of the tidal turbines. Each sampling grid totaled 28 km of transects and covered approximately 8 km^2 (Figure 2.1). Surveys were repeated from May 2nd to May 13th, 2011 and again from June 3rd to June 14th, 2011.

Table 2.1. Acoustic sampling parameters used with each acoustic technology.

Deployment	Mobile	Stationary		
Technology	Echosounder	Echosounder	Acoustic Camera	ADCP
Manufacturer	Simrad	BioSonics	Sound Metrics	Nortek
Model	EK-60	DTX	Didson	AWAC
Frequency	120kHz	120kHz	700kHz	1000kHz
Beam Angle	7^{o}	7^{o}	$.08^{o}$ x 14^{o}	25^{o}
Beam Number	1	1	48	3
Pulse length	512 µs	500 µs	92 µs	unspecified
Ping Rate	1 Hz	5 Hz	1 Hz	1 Hz

A 120 kHz, hull mounted Simrad EK-60 echosounder was used to quantify nekton density and vertical distributions during all mobile surveys. The transducer, with a transmit power of 500 W, had a beam width of 7˚ (between half power points, Table 2.1). Measurements were conducted at 1 Hz with pulse duration of 0.512 ms. The echosounder was calibrated using a 38.1 mm tungsten-carbide sphere following protocols of Foote et al. (1987).

2.2.3.2 Direct Samples

A Marinovich midwater trawl, a 6 m x 6 m box trawl fished with 4.6 m x 6.5 m (5 ft x 7 ft) steel V-doors, was used to identify constituents of observed backscatter during the mobile acoustic survey. Stretched mesh sizes ranged from 7.6 cm in the forward section of the net to 3.1 cm in the codend. The final third of the cod end was lined with a 0.9 cm knotless liner. Fish were identified to species and measured to create length frequency histograms for each species. As a precaution to the integrity of the net, trawling was restricted to times when the current was 1 knot or less, inhibiting species identification and acoustic backscatter partitioning to species or functional groups.

2.2.4. Stationary Survey

An autonomous, upward looking echosounder, ADCP, and acoustic camera were mounted on separate Sea Spider tripods (http://www.oceanscience.com/Products/Seafloor-Platforms/Sea-Spiders.aspx). The tripods were deployed 750 meters from Admiralty Head (Figure 2.1), parallel to the principal axis of tidal flow, separated by 200m. Each tripod was ballasted by 275 kg of lead weights. All acoustic technologies concurrently sampled for 12 minutes every two hours, sampling 10% of the total deployment time (12 minutes sampling / 120 minutes every two hours). The echosounder, a 120 kHz BioSonics DTX, emitted a 0.5 ms pulse five times a second, transmitting 1000 W of power (Table 2.1). The echosounder had a 7˚ beam angle (between half power points), and was factory calibrated by the manufacturer prior to deployment. The acoustic camera, a Sound Metrics DIDSON, sampled in long range “detection mode” (operating frequency 700 kHz) over a range from 2.5 m to 42.5 m. A single ping from the acoustic camera had 24,576 discreet measurement cells, 512 vertical intervals within each of forty-eight 0.8° horizontal and 14° vertical beams spaced 0.6° apart. The ADCP, a 1 MHz Nortek AWAC, sampled three 25˚ beams angled 20˚ off center at 1 Hz. Sampling parameters for all instruments are listed in Table 2.1.

2.2.5. Acoustic Data Processing

Acoustic data, except the ADCP, were processed using Echoview software (Myriax Software, v.5.4.91, http:\\www.echoview.com). Mobile acoustic measurements within 3m of the echosounder transducer face and half-meter from the bottom were excluded to avoid measurements biased by transceiver saturation and backscatter from the bottom. Mobile acoustic returns were dominated by surface turbulence introduced by tidal currents, sometimes extending to more than 80m depth. Surface turbulence was identified and excluded from analysis using Echoview's schools detection algorithm (minimum total school length = 5m, minimum total school height = 3m, minimum candidate length = 5m, minimum candidate height = 3m, maximum vertical linking distance = 10m, maximum horizontal linking distance = 10m). Detected schools that intersected the three-meter surface exclusion were classified as surface turbulence and excluded from further analysis. Echosounder data were exported at a -75 dB threshold, with a 16 dB signal to noise ratio, in order to enhance the surface turbulence exclusion algorithm.

Stationary acoustic measurements were limited to a range of 3 to 26m from the transducer face, corresponding to the maximum range of the ADCP and twice the vertical footprint of the proposed OpenHydro turbine. Stationary backscatter measurements were exported using a -75 dB threshold, identical to the mobile echosounder survey. Cells which failed to meet the signal to noise ratio in the echosounder were filtered from all gears.

Both the acoustic camera and the ADCP data were limited by a lack of a signal to noise range, calibration, and time varied gain (TVG) correction. In the absence of an ambient noise estimate, neither a signal to noise threshold nor calibration could be applied to either technology. A time varied gain (TVG) correction for beam spreading, was retroactively applied to the ADCP measurements following protocols by Nortek (2001). Signal loss due to absorption was restored using an absorption coefficient of 358.4 dB/km (*c.f.* Table 2.3 in Simmonds & MacLennan 2005). A TVG assuming spherical spreading was manually applied to each acoustic camera beam (Simmonds and MacLennan 2005), with an estimated absorption coefficient of 258 dB/km calculated using the equation from Francois & Garrison (1982). Acoustic camera measurements between 15-19 m were excluded to remove a band of continuous noise, attributed to a second acoustic bottom. Since continuous vertical data are required to calculate vertical

distribution metrics, the excluded measurements were filled with the mean measurements of the entire ping.

2.2.6. Data Binning

Observed variability in a quantity is dependent on the scale at which the quantity is measured (Wiens 1989, Schneider 2009). One of the main objectives of this study was to characterize variability in nekton density-distributions. Correlation coefficients, lagged in space or time, were used to determine the minimum spatial or temporal scale at which mobile or stationary measurements of nekton density were independent, and the analysis resolution of each survey was set to these scales (Schneider 1990). The autocorrelation of vertically integrated measurements of mean S_v (units dB re 1 dB re 1 µPa; MacLennan et al. 2002) was used to determine the range at which measurements became statistically independent. This range was used as the horizontal resolution of the data.

Once mobile and stationary horizontal resolutions were determined, mean S_v was exported in 1m vertical bins to match the vertical resolution of the ADCP. Data from these one-meter vertical analysis cells were used to derive four metrics summarizing the vertical distribution of nekton density within each horizontal analysis cell, producing four summary metrics for each spatial or temporal analytic cell.

2.2.7. Metrics to Characterize Nekton Density and Vertical Distribution

Four metrics were used to measure density and vertical distributions of nekton in the water column; mean volume backscattering strength (mean S_v), center of mass, inertia, and an aggregation index. Mean volume backscattering strength (MacLennan et al. 2002) is a depth-independent metric of nekton density integrated through the entire water column. The remaining three metrics, selected from a suite of metrics developed by Burgos & Horne (2008) and further refined by Urmy et al. (2012), summarize the vertical distribution of nekton measured in one-meter increments through the water column. The first of these metrics, center of mass (units: m), is a metric of the mean weighted location of backscatter in the water column relative to the bottom. Inertia (units: m^2) measures nekton dispersion and is analogous to the variance of nekton distribution surrounding the center of mass. The aggregation index (units: m^{-1}) measures the vertical patchiness of backscatter through the water column. The aggregation index is calculated on a scale of 0 to 1, with 1 being aggregated. Collectively these four metrics are referred to as “Echometrics”.

2.2.8. Covariates

Julian day, time of day, tidal speed, daily tidal range (range between high tide and low tide within a day), and tide state (flood vs. ebb) were all hypothesized to affect nekton density and distribution. Time of day was used as a proxy for light intensity, associated with diel vertical migration in nekton (Banse 1964). Both mobile and stationary measurements were categorized as day (06:00 – 18:00), night (22:00 – 02:00), or crepuscular (04:00 and 20:00) based on naval sunrise/sunset times. Mobile measurements were also categorized by month (May/June) and sampling grid (North/South).

Both mobile and stationary acoustic data were linked to tidal velocities measured at ten meters off bottom and collected at ten-minute intervals by the ADCP. Tidal velocities were used to categorize tidal speed and tidal state. Tidal speed was measured as a continuous variable (0.1 m/s bins) and summarized into a categorical variable (slack, moderate, and extreme). Slack (< 0.5 m/s), moderate (0.5m/s < moderate < 1.5m/s), and extreme (> 1.5m/s) tidal categories were identified from modes in the histogram of tidal current speed, allocating the first and fourth quartiles into slack and extreme tidal speed categories. Ebb or flood tidal states were assigned using the dominant tidal heading relative to the principal tidal axis. In addition to instantaneous tidal velocity, tidal range is a proxy for tidal speed integrated through a 24-hour day. The cube of tidal speed, proportional to tidal power (Betz 1966), was used as the covariate of tidal speed.

2.2.9. Characterizing Backscatter Variability

Covariates influencing median nekton densities and vertical distributions in both the mobile and stationary data were categorically analyzed using an approximation of the 95% confidence interval of the median extending +/- 1.57 of the interquartile range divided by the square root of the sample size (Chambers et al. 1983). These confidence intervals, based on asymptotic normality of the median, identify significant differences between covariate categories of approximately equal sample sizes. The insensitivity of this method to the underlying distribution of the covariate makes it particularly useful for Echometric data, because it provides a single statistical tool to analyze each metric, regardless of the underlying distribution and is insensitive to statistical outliers (Chambers et al. 1983).

2.2.10. Wavelet Analysis

Wavelet transformations decompose a time series into frequency domain at every time step in a series, resulting in a two-dimensional heat-map illustrating the variance contributed by each temporal

period at each time step (Torrence & Compo 1998, Figure 2.2). Wavelet power (*i.e.* variance) heat maps, called scalograms, identify the variance at each time step (*x*-axis) across a spectrum of temporal scales (*y*-axis). Localized differences in the scales of peak variances identify transient or transitory patterns in the scales contributing to the variability observed in a time series. Traditional frequency domain analysis techniques, such as spectral power, are constrained to a global analysis of the series and cannot identify localized transient or transitory patterns in variance (Saunders et al. 2005). Localized decomposition of wavelet transforms eliminates assumptions of stationarity that bias or inhibit spectral analysis in many biological contexts (Torrence & Compo 1998, Saunders et al. 2005). Horizontally integrating wavelet power at a single scale through time (*i.e.* the global wavelet spectrum) measures the variance contributed by each scale across the series, analogous to the power spectrum (Torrence & Compo 1998). Vertically integrating all scales within a given time step (*i.e.* scale averaged wavelet power) decouples observed variability from scale, providing an instantaneous estimate of variance across scales.

Assuming that underlying physical processes influencing a data series can be inferred from the periods at which a data series varies (Platt & Denman 1975, Steele et al. 1994), the relative influence of a cyclical physical process can be inferred from the variability measured in its corresponding temporal scale. Leveraging this concept, the wavelet scalogram can be used to identify locally significant physical processes influencing each metric of nekton density or vertical distribution. The global wavelet spectrum provides a statistically rigorous metric of the variability contributed by each scale across the entire time series (*i.e.* power spectrum; Percival 1995, Perrier et al. 1995, Torrence & Compo 1998). Periods contributing statistically significant amounts of variance to the time series can then be included as Fourier series covariates in time series models as a proxy representing the underlying physical processes which could not be directly measured.

A continuous, Morlet mother wavelet-transform was applied to the data to describe the structure of the variability in the stationary Echometric series. Morlet mother wavelets offer precision in the frequency domain at only a slight cost to precision in the time domain (Mallat 1989). A continuous wavelet transform, with twelve steps per octave, increased the scale resolution twelve-fold compared to discrete wavelet transforms. The temporal scales analyzed ranged from 4 hours (twice the resolution of each time series) to 256 hours (35.5% of the total series length), with 84 analyzed scales increasing

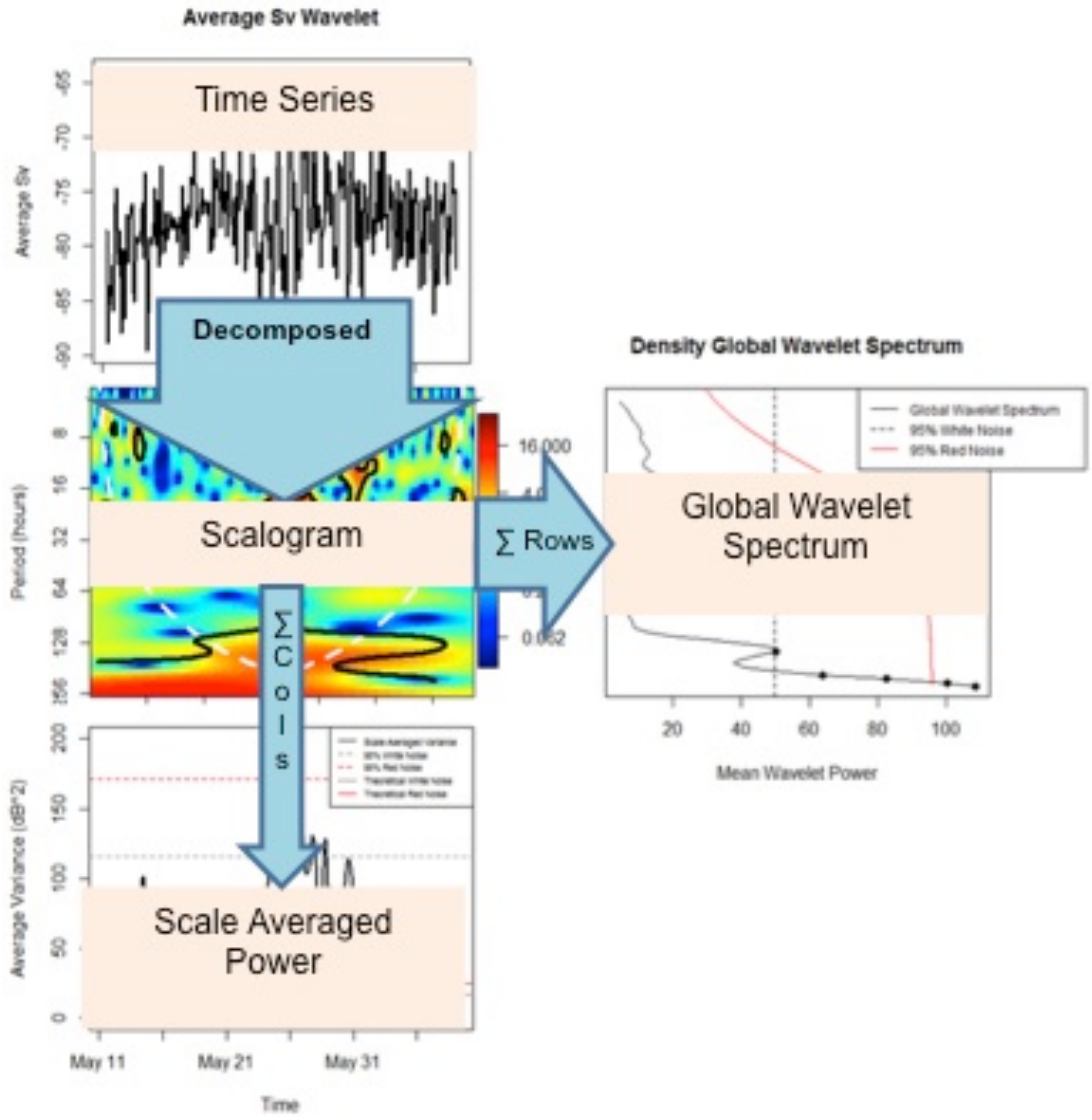

Figure 2.2. Wavelet Analysis and its applications. The data series (top) is decomposed into frequency domain at every time step to create the scalogram (center). The sum of wavelet power across all times within a band of periods is the global wavelet spectrum (right), analogous to spectral power. The scale averaged wavelet power (bottom) is the sum of wavelet power across all periods at each time step. All three panels on the left share a common time series ordinate.

exponentially as $2^{(i+23)/12}$ where *i* is the scale step with 12 steps per octave. The beginning and ending of each stationary Echometric series was padded with zeroes (Torrence and Compo 1998) to facilitate analysis near the start and end of the time series. These zeroes create edge effects, which artificially dampen wavelet power near the edges of the time series. The reduced power near an edge is exaggerated at large scales, decreasing the power to identity large scales as statistically significant. Statistical significance in localized wavelet power in the scalogram was tested against a white noise null hypothesis at a 95% confidence level (Torrence and Compo 1998). A full review of the considerations and calculations when using wavelet analysis is beyond the scope of this paper, but can be found in Torrence and Compo (1998) and Cazelles et al. (2008).

The significance of all 84 discreet scales was tested against white- and red-noise null hypotheses. A white noise null hypothesis is a constant value across all scales, equal to the variance of the time series. The red noise spectrum, a more realistic and conservative spectrum assuming autocorrelation (Torrence & Compo 1998), was modeled as a first order autoregressive process with the variance and autocorrelation empirically derived from the time series. Each theoretical spectrum was multiplied by the 95% confidence χ^2 statistic with two degrees of freedom to create a 95% confidence interval (Torrence & Compo 1998). Statistically significant scales were included in time-series models as Fourier series.

The mean wavelet power across all scales at a given time step (*i.e.* scale averaged wavelet power) is an instantaneous metric of variance across all scales (Torrence and Compo 1998). Volatile periods of a time series (*i.e.* instances of high-localized variability) are characterized by sharp peaks in a quantity and high scale averaged wavelet power. Peaks in quantities such as biological density or mean vertical distribution, are assumed to increase the risk (*i.e.* the probability of occurrence multiplied by the severity) of nekton interacting with a device. Instantaneous variance in nekton density and vertical distribution is an easily measured proxy for the risk of biological interactions. Given that variance is dependent on the scale at which it is measured, variance estimated risk may be exaggerated or dampened by an arbitrary analytical scale. By taking the mean variance across all measurement scales at a given time, the scale averaged wavelet power decouples variance from the measurement scale, creating a time specific index of variance independent of scale (Torrence & Compo 1998). Scale

averaged wavelet power can be used as a proxy for risk that is not biased by measurement scale, creating a time series of biological risk.

Similar to the global wavelet spectrum, peaks in the scale averaged wavelet power can be tested against a white- or red-noise null hypothesis. The white-noise scale averaged wavelet is equal to the variance of the series, while the theoretical red-noise spectrum was modeled as a first-order autoregressive process with known variance and autocorrelation. The 95% confidence interval for both the white- and red-noise spectrum was derived from the 95% confidence χ^2 statistic with two degrees of freedom (Torrence and Compo 1998). Periods of statistically significant peaks in variance were identified as events of greater risk of biological interactions.

2.2.11. MARSS State-Space Time Series Models

Multivariate Auto-Regressive State-Space (MARSS) models are linear, multivariate, first-order autoregressive, time-series models assuming Gaussian error in the modeling of populations (*i.e.* state) and the measurement of those populations (Holmes et al. 2012). MARSS models assume that the true population in the modeled series are hidden by measurement error. Using a maximum likelihood framework, MARSS models apply a Kalman smoother to estimate the state at each time step from measurements represented in the time series. The state model includes four components to concurrently model each population or metric. First, auto-regressive matrices relate population estimates from the previous time step to the current step, and allow for auto-regressive coefficients between different metrics. Multivariate matrices relate each metric to each covariate with a unique coefficient. A linear trend can be added, and the error structure of each population is capable of including the variance and covariance between several modeled populations (Holmes et al. 2012). The observation process includes a linear scaler, multivariate matrices to change the sampling bias as a function of environmental covariates, and an error structure capable of including the covariance between separate concurrently modeled series. The best-fit model, identified by the small sample size corrected Akaike information criteria (*i.e.* AICc; Holmes et al. 2012), estimates the true quantity at each step and provides a 95% confidence interval.

MARSS models have several unique attributes that make them attractive for time series modeling, particularly for modeling nekton density and vertical distribution at tidal current sites. First,

MARSS models don't require concurrently modeled series to be treated independently. Although each metric measures a unique quantity, metrics of vertical distribution may be related due to predictable nekton behavior, such as diel vertical migration. MARSS models enable these inter-dependencies to be expressed as auto-regressive terms in the state equation or covariance terms in the error matrix. The ability to include covariates in the observation process is valuable when measurement precision may be compromised by environmental challenges, such as tidal currents. The best-fit model provides insight to the variability of fish and macrozooplankton distribution in high flow areas, and statistically test if there are non-uniform sampling biases introduced by the environment.

The stationary metric series derived from acoustic backscatter data were modeled through time using MARSS models. To meet assumptions of normality, each metric series was demeaned and normalized using a z-score transformation. An additional $\log_{10}$ transformation was applied to the positively skewed aggregation-index before applying the z-score transformation. Daily tidal range, instantaneous tidal speed, Julian day, and a Fourier series defined by a 24-hour period were included as possible covariates in both the process and observation equations. Twenty-one models increasing in complexity were iteratively tested using forward model selection. Models varied from random walk models to multivariate processes with autoregressive relationships between metrics. The models, listed in ascending order of AICc values in Table (2.3), were forward selected. Model goodness of fit was analyzed from AICc using the quasi-Newton "BFGS" algorithm (Holmes et al. 2012). The distribution of model residuals was scrutinized for randomness using goodness of fit, residual QQ plots, and autocorrelation diagnostic plots.

2.2.12. Acoustic Technology Comparisons

Stationary echosounder measurements functioned as a standard to compare the ADCP and acoustic camera measurements. First, the ability of both acoustic technologies to measure nekton distribution through time and tidal cycles was compared to measurements by the echosounder. This pattern matching assessment assumes that acoustic technologies lacking the sensitivity to identify patterns in nekton density-distributions also lack the sensitivity to identify changes in nekton communities after a perturbation. Second, measurements from both the ADCP and acoustic camera were regressed against concurrent echosounder measurements. Significant, positive relationships at two-temporal and

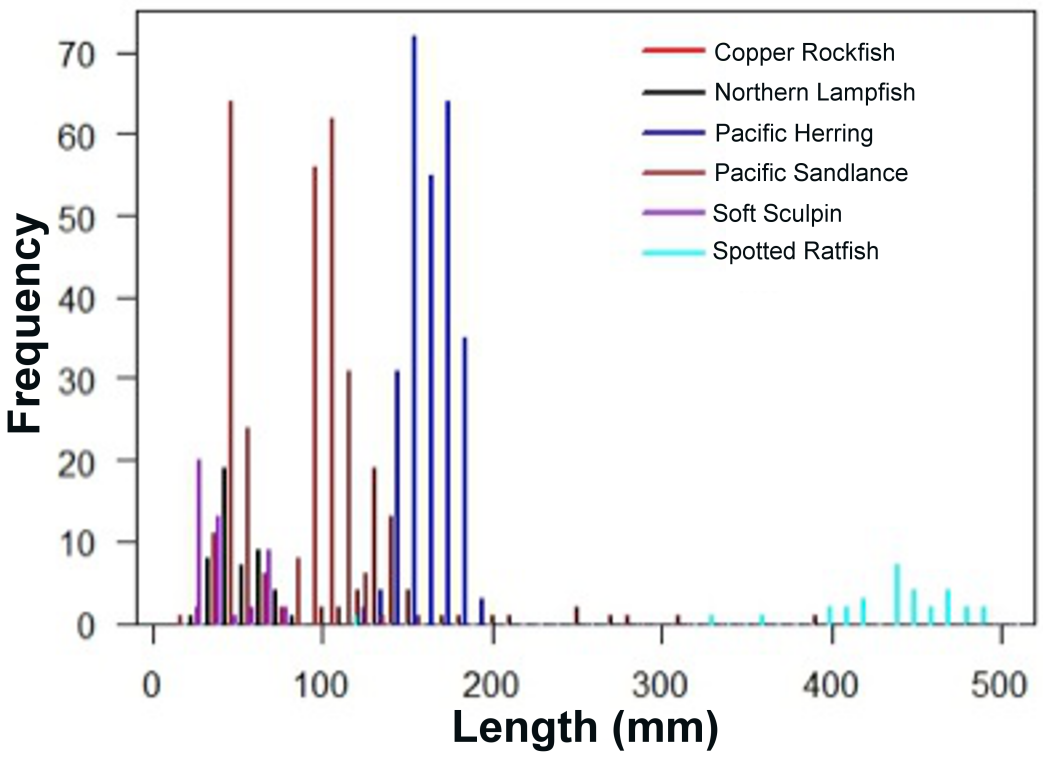

Figure 2.3. Length frequency distribution of the six most abundant species collected in 36 midwater trawls. Trawls targeted aggregations and are representative of species length frequency distributions and not relative abundances.

two-vertical measurement resolutions were tested using a repeated measures ANOVA ($\alpha = 0.05$) with a Bonferroni correction.

2.3. Results

2.3.1. Trawl Catches

A total of 41 fish species were collected by the 36 mid-water trawls that were evenly distributed between May and June, 2011. Six fish species were represented by greater than 30 individuals collected: Pacific herring (*Clupea pallasii*), copper rockfish (*Sebastes caurinus*), Northern lampfish (*Stenobrachius leucopsarus*), Pacific sand lance (*Ammodytes hexapterus*), soft sculpin (*Psychrolutes sigalutes*), and spotted ratfish (*Hydrolagus colliei*) (Figure 2.3). The longest of these dominant species was the spotted ratfish measuring an average of 417 mm. Midwater trawls were not randomly conducted, but targeted at specific aggregations or to characterize the species composition of the fish community, thereby limiting the interpretation of these data to presence/absence and length frequency distributions (as opposed to an independent metric of species abundance). Four species, copper rockfish, Pacific herring, and ratfish were caught in single trawl hauls exceeding 30 individuals. A total of 328 Pacific herring, 275 Pacific sand lance, 353 copper rockfish, and 156 spotted ratfish were collected. The largest specimen sampled was a 870 mm spiny dogfish (*Squalus acanthias*), one of three spiny dogfish collected in the survey.

2.3.2. Patterns in Nekton Density and Vertical Distribution

2.3.2.1. Mobile Acoustic Survey

Mobile acoustic surveys were repeated daily and nightly from May 2nd, 2011 to May 13th, 2011 and June 3rd, 2011 to June 14th, 2011 sampling 56.5 mobile survey grids. Effort was evenly distributed between May (n=28.5) and June (n = 28) and the North and South grids (Table 2.2). The median horizontal autocorrelation of the vertically integrated mobile density measurements reached 0 at 300m, so the horizontal analysis cell size was set at 300m. A 300m analysis cell resulted in at least four cells within each transect, and up to ten in the south grid. Mobile acoustic sampling effort was focused during daylight hours, with 76% of mobile grids conducted during day (13 at night & 43.5 daytime). A total of 5,054, 300m analytic cells were created from the acoustic backscatter data. These cells were approximately equally distributed between the north (n = 2,468) and south (n = 2,568) sampling areas and between the May (n = 2,510) and June (n = 2,544) sampling periods. Mobile acoustic data were

Table 2.2. Allocation of line transects and mid-water trawl effort in Admiralty Inlet, Puget Sound in May and June, 2011.

Month	Activity	Diel Period	North Grid	South Grid
May	Acoustic Grids	Day	12	10.5
		Night	3	3
	Trawling	Day	5	8
		Night	3	2
June	Acoustic Grids	Day	11	10
		Night	3	4
	Trawling	Day	7	8
		Night	1	2
Total	Acoustic Grids	Day	23	20.5
		Night	6	7
		Total	29	27.5
	Trawling	Day	12	16
		Night	4	4
		Total	16	20

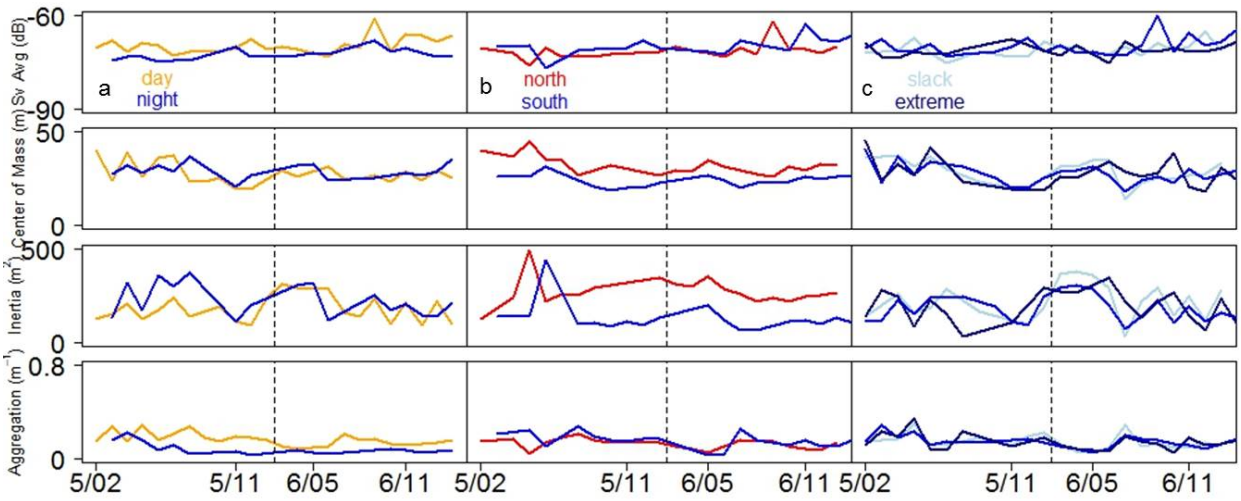

Figure 2.4. Nekton density and vertical distributions measured from repeated mobile surveys illustrating (a) changes between diel periods (day, night), (b) geographic differences between north and south survey grids, and (c) distributional changes as a function of tidal states (slack, moderate, extreme).

collected across a spectrum of tidal current speeds, with a majority of observations in moderate (0.50 m/s < moderate < 1.50 m/s; n = 2751) tidal currents compared to slack (< 0.50 m/s; n = 969) or extreme (> 1.50 m/s; n = 741) tidal current speed categories. Over the mobile survey, the mean metric of nekton density (vertical mean of mean S_v) was -73.45 dB, ranging from -79.87 dB to -39.66 dB. On average, nekton were centered 27.50 m off the bottom and dispersed with a variance of 181.3 m^2. The mean index of aggregation, on a scale of 0 to 1, was 0.159 m^{-1}.

Mean nekton density and vertical distributions differed between the north and south sampling grids. Mean nekton density was 0.477 dB higher in the north than the south (north mean S_v = -73.22 dB; south mean S_v = -73.70 dB, p = < 0.001, Figure 2.4). Nekton in the south sampling grid were, on average, located 8 m closer to the bottom (north center of mass = 31.59 m; south center of mass = 23.61 m, p < 0.001), less dispersed (-144.54 m^2, p < 0.001), and 19.5% more tightly aggregated (north aggregation index = 0.142 m^{-1}; south aggregation index = 0.169 m^{-1}, p < 0.001). Backscatter distributions during repeated mobile measurements were consistent with nekton diel vertical migration behavior. Nekton density did not significantly change across diel periods (day mean S_v = -73.40 dB; night mean S_v = -73.63 dB, p = 0.086), but moved higher in the water column (day center of mass = 27.27 m; night center of mass = 28.27 m, p = 0.027). As expected, nekton became more dispersed (day inertia = 171.57 m^2; night inertia = 213.54 m^2, p < 0.001) and less aggregated at night (day aggregation index = 0.173 m^{-1}; night aggregation index = 0.096 m^{-1}, p < 0.001).

Nekton density distributions measured during mobile surveys changed between May and June. Nekton density increased 43% from May to June (May mean S_v = -74.25 dB; June mean S_v = -72.67 dB, p < 0.001), moved lower in the water column (May center of mass = 28.00 m; June center of mass = 27.00 m, p = 0.011), and became more aggregated (May aggregation = 0.185 m^{-1}; June aggregation = 0.127 m^{-1}, p < 0.001). Nekton dispersion did not change between May and June (p = 0.420).

Using a Tukey's honestly significant difference *post hoc* test, mobile backscatter measurements of nekton decreased by 0.69 dB at extreme tidal current speeds (slack-moderate: p = 0.703, moderate-extreme: p < 0.001), while nekton dispersion increased during slack tides (slack-moderate: p = 0.004, moderate-extreme: p = 0.830). Nekton mean weighted location (slack-moderate: p = 0.141, moderate-

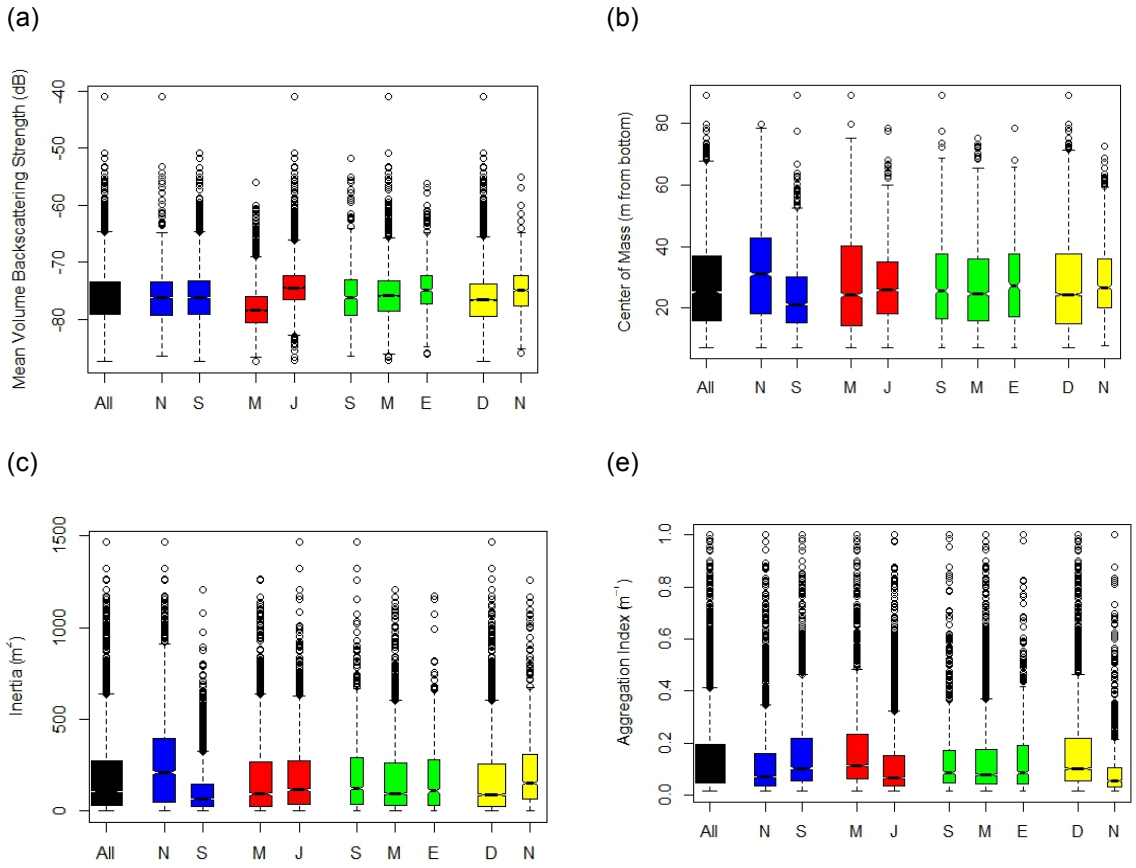

Figure 2.5. Mobile acoustic measurements measuring nekton (a) mean density, (b) mean weighted location, (c) dispersion, and (d) aggregation within each geographic sampling grid (blue; N = North, S = South), month (red; M = May, J = June), tidal speed (green; S = slack (< 0.5 m/s), M = moderate (0.5 < moderate < 1.5 m/s), E = extreme (> 1.5 m/s)), and diel period (yellow, D = day, N = night). Whiskers extend to 1.5 times the interquartile range. Box widths are proportional to the square root of the sample size, with a grand sample size of 5,054 samples. Overlapping notches are used to test significant differences between the medians of categories where notches extend to 1.58 times the interquartile range divided by the square root of the number of samples (*c.f.* Chambers et al. 1983 for technique details).

extreme: p = 0.113) and aggregation (slack-moderate: p = 0.573, moderate-extreme: p = 0.959) remained consistent across tidal currents.

Significant patterns emerged in the median measures of nekton density distributions as the mean, with two exceptions. Median nekton density was nearly identical between the north and south sampling areas (north median mean S_v = -74.22 dB, south median mean S_v = -74.21 dB, Figure 2.5), but increased from day to night (day median mean S_v = -74.34 dB; night median mean S_v = -73.87 dB). All other patterns observed in median nekton density-distributions were consistent with those observed in mean distributions.

2.3.2.2. Stationary Survey

Stationary echosounder measurements were collected for twelve-minutes every two hours from May 9th, 2011 to June 8th, 2011 resulting in 360 sampling periods. Stationary measurements of integrated backscattering strength became statistically independent at a 24-second temporal lag within each sampling period, as determined by autocorrelation. Each sampling period was divided into 30, 24-second horizontal bins, resulting in 10,800 independent sampling periods, 10,130 of which had concurrently collected tidal velocities. Stationary data was also analyzed at the coarser 12-minute temporal scale, creating 360 equally spaced analysis cells for time series analysis. Stationary data were collected across tidal current categories (slack: n = 1894, moderate: n = 5065, extreme: n = 3171), tidal states (flood tides: n = 5216, ebb tides: n = 4914), diel periods (day: n = 6277, night: n = 2719, crepuscular: n = 1815). Nekton density ranged from -90.02 dB to -51.57 dB.

The 360 12-minute sampling bins were used to create a time series for each metric (Figure 2.6). A saw-tooth, diel pattern dominated values in all four series, but a larger periodic wave also appeared to be present in nekton density, center of mass, and dispersion. Nekton density increased 2 dB through the time series (p = 0.007), equating to a 58% increase in nekton density within the month deployment. The center of mass moved 3 m higher in the water column through the deployment (p = 0.007), and nekton became more highly dispersed (p = 0.008). The aggregation index remained close to zero throughout most of the time series, punctuated by an episodic presence of high aggregation values. Statistical tests were not applied to the aggregation index because the data were not normally distributed.

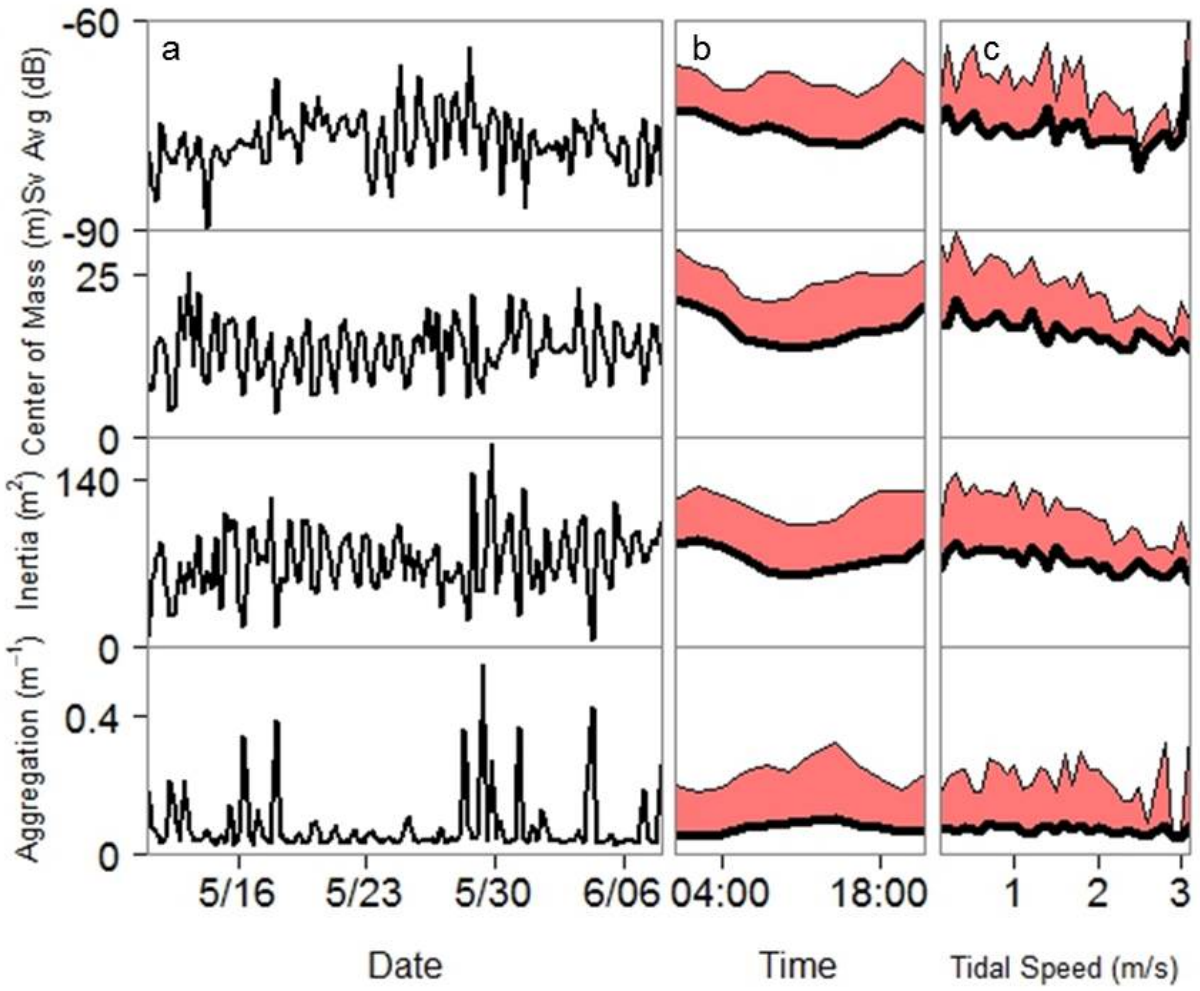

Figure 2.6. Patterns in nekton density and vertical distribution measured from stationary, upward facing echosounder. Density and vertical distributions were indexed as a function of (a) time, (b) time of day (mean + 2 standard deviations), and (c) tidal speed (mean + 2 standard deviations). From top to bottom, the ordinate quantities are density (metric: mean S_v; units: dB, re 1 μPa), mean weighted location from bottom (metric: center of mass, units: m), dispersion (metric: inertia; units: m^2), and aggregation (metric: aggregation index; units: m^{-1}).

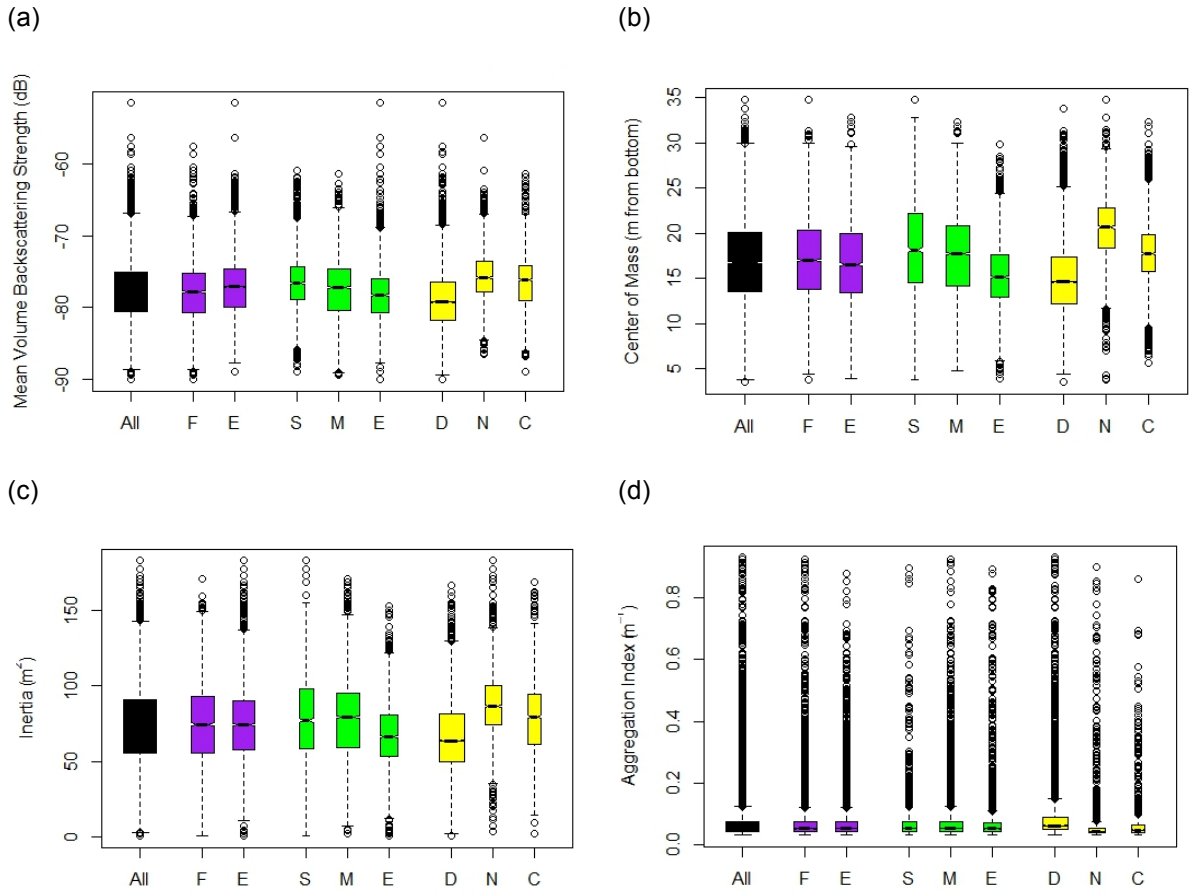

Figure 2.7. Stationary acoustic measurements measuring nekton (a) mean density, (b) mean weighted location, (c) dispersion, and (d) aggregation within each tidal state (purple; F = flood, E = Ebb), tidal speed (green; S = slack (< 0.5 m/s), M = moderate (0.5 < moderate < 1.5 m/s), E = extreme (> 1.5 m/s)), and diel period (yellow; D = day, N = night, C = crepuscular). Whiskers extend to 1.5 times the interquartile range. Box widths are proportional to the square root of the sample size, with a grand sample size of 10,800 samples, and 10,130 in across the tidal categories. Overlapping notches are used to test significant differences between the medians of categories where notches extend to 1.58 times the interquartile range divided by the square root of the number of samples.

Patterns in the density and distribution of backscatter versus time of day were consistent with nekton diel vertical migration behavior (Figure 2.6). Acoustic backscatter more than doubled at night (+3.5 dB at night, $p < 0.001$, n = 10,800), moved higher in the water column (+5.6 m at night, $p < 0.001$), and became more dispersed (+20.5 m^2 at night, $p < 0.001$). Qualitatively, aggregation index values increased during daylight hours. Variability in all metric values remained relatively consistent through the time of day (Figure 2.6). Nekton density decreased as tidal speed increased (-0.70 dB $(m/s)^{-1}$, $p < 0.001$, n = 10,130), and moved closer to the bottom (-1.90 m $(m/s)^{-1}$, $p < 0.001$) while becoming less dispersed (-8.13 m^2 $(m/s)^{-1}$, $p < 0.001$). Nekton aggregation was independent of tidal speed (p value=0.701). In general, variability observed in metric values decreased with tidal speed.

Patterns in the median nekton density and distribution metric values were consistent with mean patterns, varying through time and tidal cycles. Small differences between flood and ebb tides were observed in median nekton densities (-77.8 dB to -77.2 dB, Figure 2.7), center of mass (16.9 m to 16.7 m, Figure 2.7), and dispersion (74.8 m^2 to 73.7 m^2, Figure 2.7).

2.3.3. Wavelet Analysis

The time series (n = 360) was decomposed into time-frequency space using wavelet analysis (Figure 2.2). The cone of influence, denoted by the dotted white line, identifies the extent to which padded zeroes dampen power (*i.e.* edge effects). Statistically significant ($\alpha = 0.05$) areas of the scalogram, tested using a Chi-square distribution assuming white noise, are traced with a black line. Mean S_v, center of mass, and inertia significantly varied at the 24-hour diel period (Figures 2.8, 2.9, 2.10). Nekton density, center of mass, dispersion, and aggregation locally varied over a period of ~256 hours (~2 weeks) within the cone of influence, but the padded zeroes at larger periods weakens the signal near the beginning and end of the time series. Troughs in the daily tidal ranges on May 11th and May 26th, 2011 coincided with an event that caused nekton center of mass to vary at the 12 hour period instead of the 24 hour period. The event on May 26th corresponded to a sharp spike in the variance of nekton density at the 24-hour period, while variance in nekton mean weighted location and dispersion was dampened at the same 24-hour period.

Peaks in the global wavelet spectrum at the 24-hour period suggested that variance in nekton density, center of mass, and dispersion were principally influenced by the diel tidal cycle (Figures 2.8, 2.9,

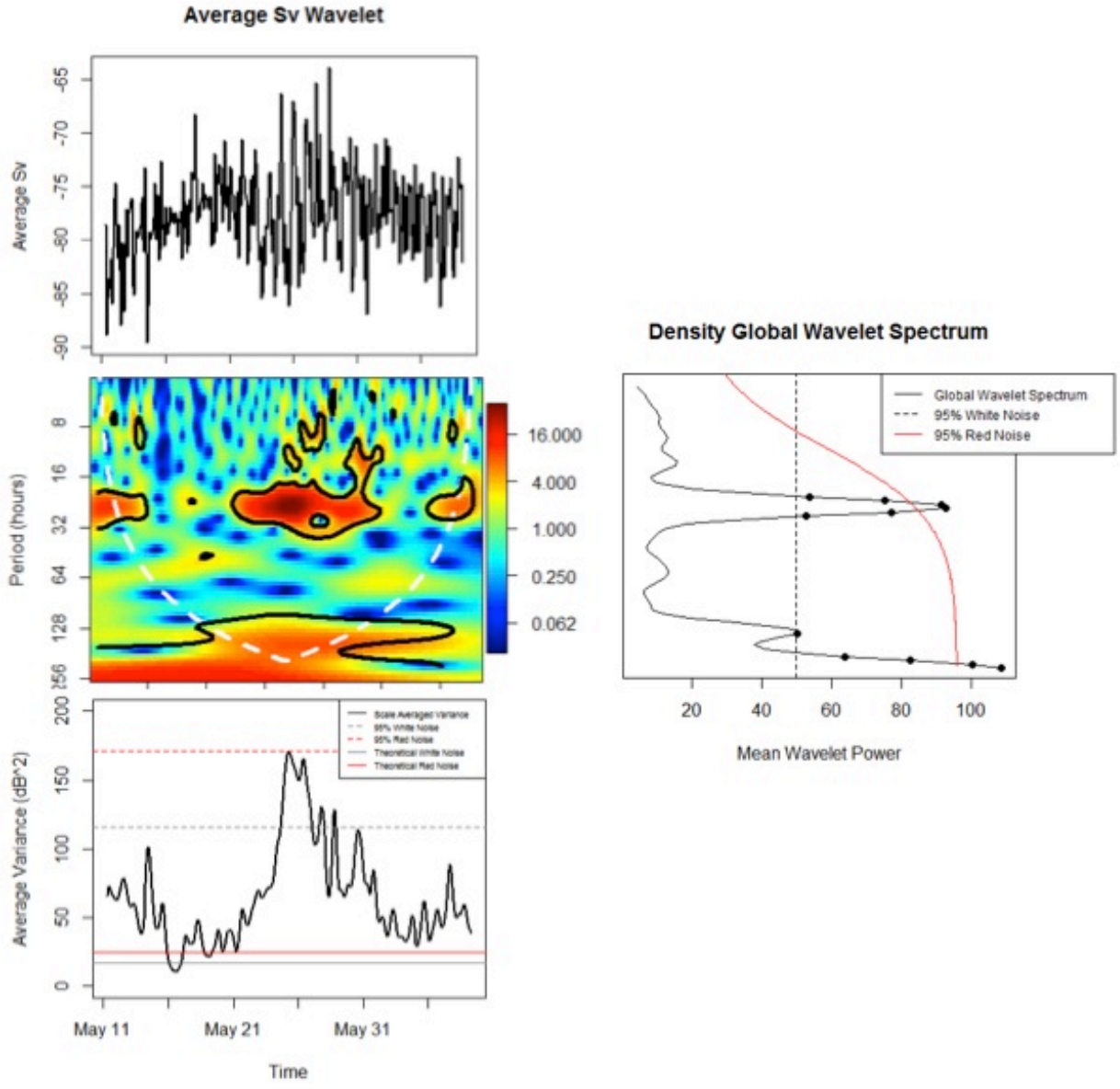

Figure 2.8. Wavelet decomposition of the temporal variability in nekton density. The time series (top panel) is decomposed into the scalogram (center). Summing horizontally across the scalogram yields the global wavelet spectrum (right), analogous to the power spectra. Summing vertically yields the scale averaged wavelet power (bottom), an estimate of variance across scales.

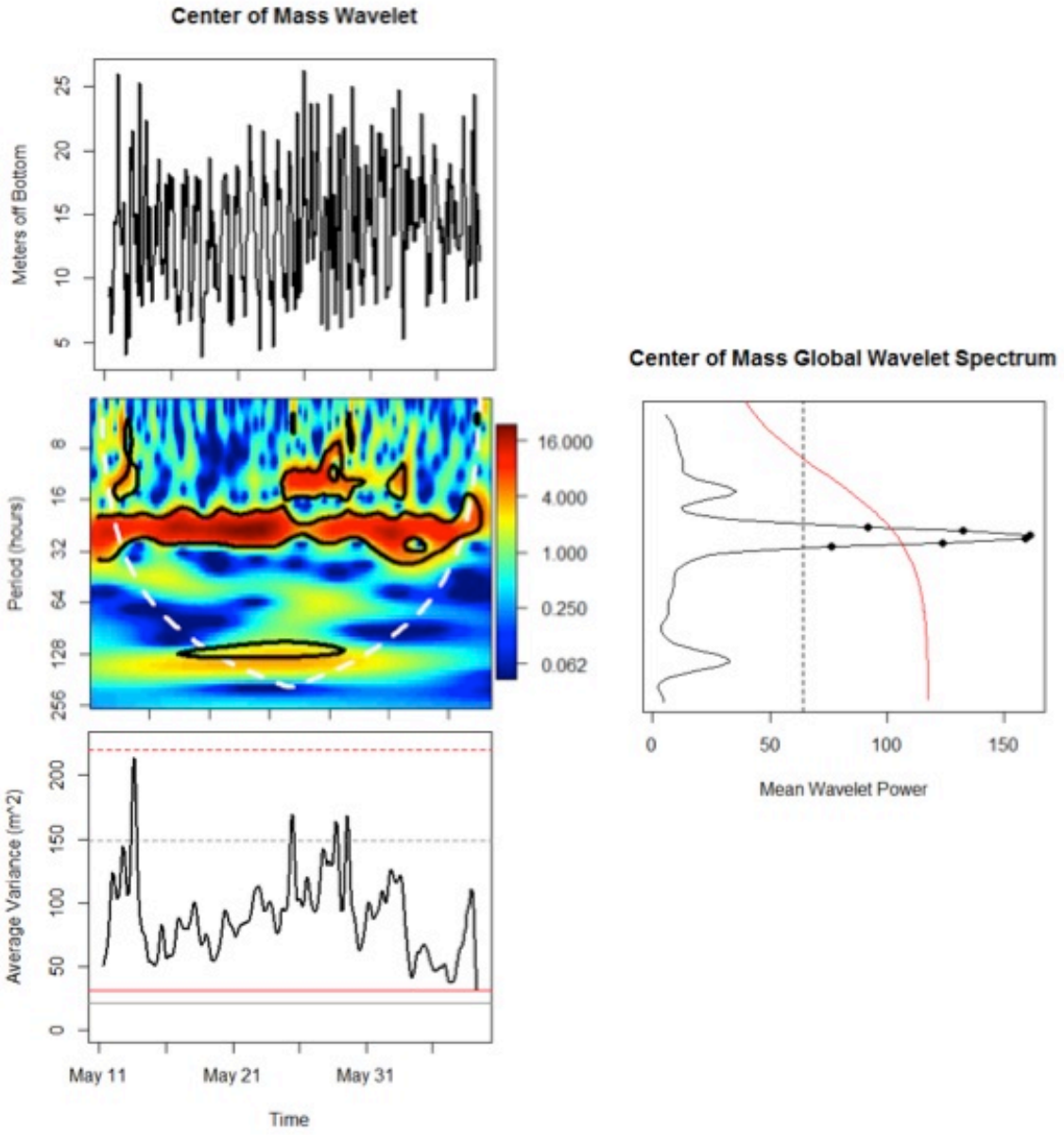

Figure 2.9. Wavelet decomposition of the temporal variability in nekton mean weighted location relative to the bottom. The time series (top panel) is decomposed into the scalogram (center). Summing horizontally across the scalogram yields the global wavelet spectrum (right), analogous to the power spectra. Summing vertically yields the scale averaged wavelet power (bottom), an estimate of variance across scales.

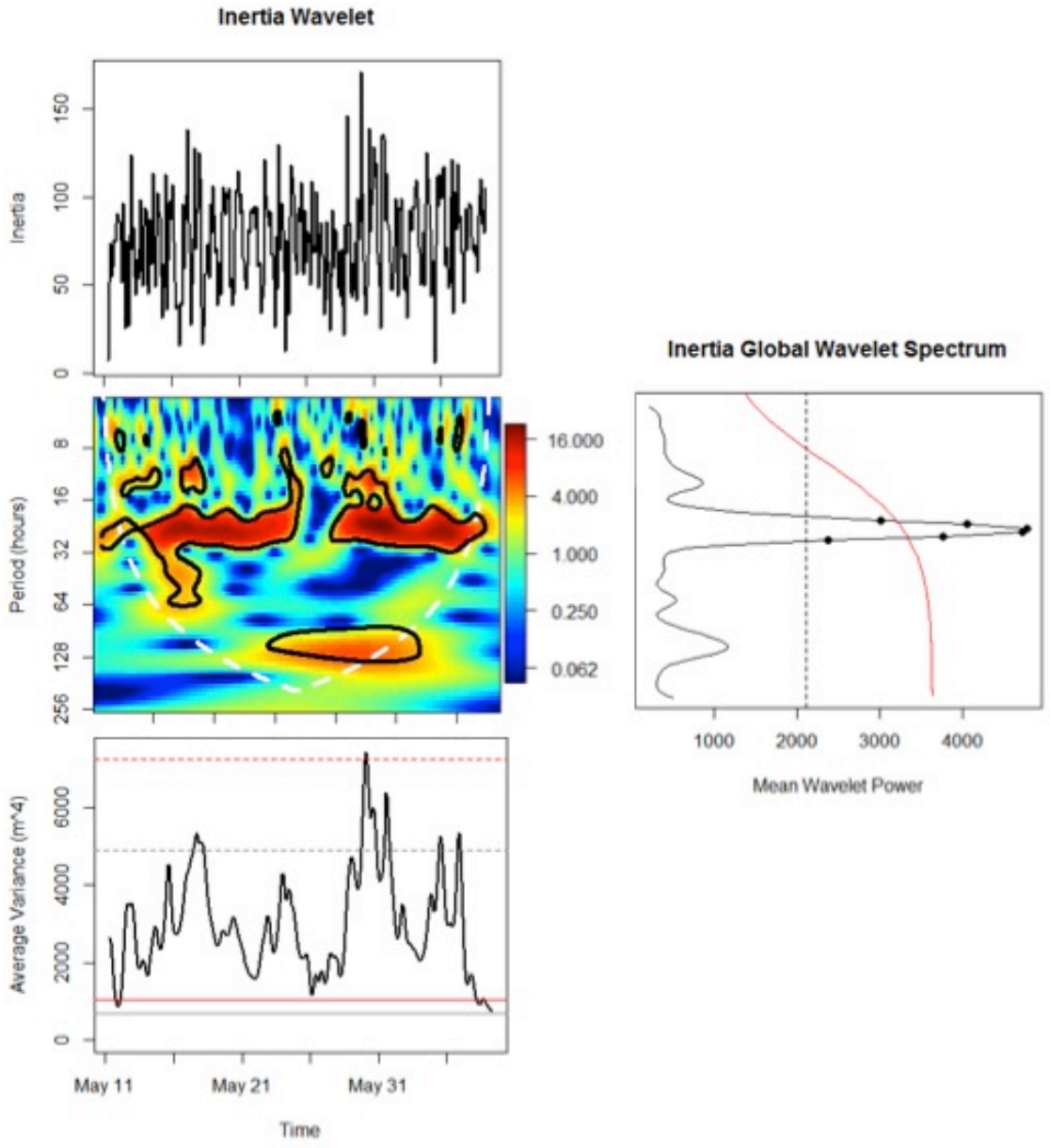

Figure 2.10. Wavelet decomposition of the temporal variability in nekton dispersion. The time series (top panel) is decomposed into the scalogram (center). Summing horizontally across the scalogram yields the global wavelet spectrum (right), analogous to the power spectra. Summing vertically yields the scale averaged wavelet power (bottom), an estimate of variance across scales.

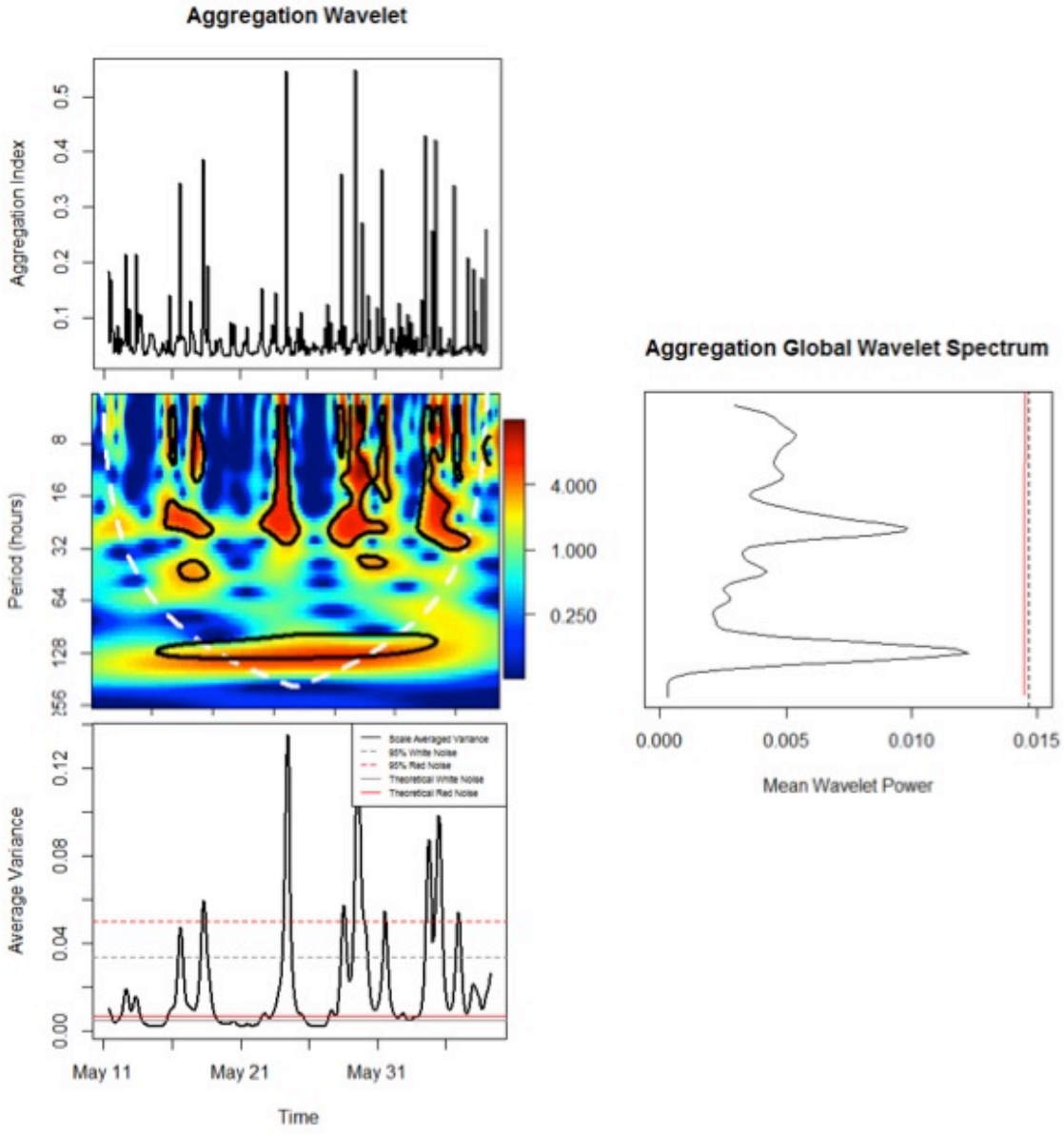

Figure 2.11. Wavelet decomposition of the temporal variability in nekton aggregation. The time series (top panel) is decomposed into the scalogram (center). Summing horizontally across the scalogram yields the global wavelet spectrum (right), analogous to the power spectra. Summing vertically yields the scale averaged wavelet power (bottom), an estimate of variance across scales.

2.10). Tested against both red and white noise null hypotheses, the aggregation index also varied with diel period, but the peak was not statistically significant (Figure 2.11). A peak corresponding to the 256 hour period appeared in each metric's global wavelet spectrum, but was only significant in the spectra of nekton density (Figure 2.8). Peaks in scale-averaged wavelet power exceeding the red noise 95% confidence interval only occurred twice in the density, mean weighted location, and dispersion spectra (Figures 2.8, 2.9, 2.10). Both peaks were related to the trough in tidal range on May 26th, 2011. The scale averaged variance of nekton density exceeded the red noise 95% confidence interval during the tidal trough, while scale averaged variance of nekton dispersion peaked on May 28th. Scale averaged variance of nekton mean weighted location peaked on May 14th, 2011, but did not exceed the red-noise threshold (Figure 2.9).

2.3.4 MARSS Model:

Two time series models were chosen based on AICc values. The best model included nekton density and vertical distribution as a function of the cube of tidal speed, the cube of tidal range, Jullian day, and a 24-hour time period. This model included first order autoregression between the density and three vertical distribution metrics and succeeded in capturing the diel periodicity (large coefficients relating the 24 hour period to nekton distributions). Model residuals of all four metrics were not random. The biased, non-random structure of the model residuals in all four metrics removed this model from consideration.

The second model was built from prior knowledge of nekton behavior in high energy environments. This model included all environmental covariates ([tidal speed]^3, [tidal range]^3, Julian day, and Fourier 24-hour series), auto-regressive density-dependent vertical distributions, and unique observation errors for each metric. This model consistently underestimated observed metric values by a factor of approximately two. This constant bias was corrected by multiplying expected values by the inverse of the slope of the best-fit line relating observed values to expected values. A correction value of two was applied to predicted mean S_v, center of mass, and inertia. A correction factor of 2.5 was applied to predicted aggregation index values. Even though this bias correction was not accounted for in the AICc calculation, this model was still the second best fit (Table 2.3, Figure 2.12) of all models. After applying the model correction, predicted values were highly correlated to observed values in all metrics

Table 2.3. AICc selection criteria for iterations of MARSS model selection. D&U denotes diagonal and unequal matrices, while id denotes identity matrices. The B matrix is the autoregressive coefficients, with off diagonals in the B matrix measuring autoreggressive density dependence. TS3 is the cube of tidal speed, TR3 is the cube of tidal range, DN is Julian day, and 24H is a Fourier series with a period of 24-hours to model diel periods. See Holmes et al. (2012) for description of the structure of MARSS models and how matrices relate mathematically.

Model #	AICc	Structure	Process Covariates	Observation Covariates
16	3339.5*	B off diagonals	All	D: 24H
Theoretical	3352.9	B=off diagonols, Z = D&U	All	None
18	3358.1	B off diagonals	All	D: All
15	3360.2	B off diagonals	All	D: TR3
14	3370.1	B off diagonals	All	D: TS3
11	3371.5	B=D&U, Z=id	TS3, TR3, 24H	None
10	3372.9	B=D&U, Z=id	DN, TS3, 24H	None
7	3374.2	B=D&U, Z=id	DN & 24H	None
8	3374.7	B=D&U, Z=id	TS3 & 24H	None
12	3398.9	B=D&U, Z=id	All	None
9	3401.6	B=D&U, Z=id	TR3 & 24H	None
17	3408.0	B off diagonals	All	D: TS3, TD3, 24H
6	3413.8	B=D&U, Z=id	24H	None
4	3600.3	B=D&U, Z=id	TS3	None
AR-1	3627.5	None	None	None
3	3632.3	B=D&U, Z=id	DN	None
1	3635.1	B=D&U, Z=id	None	None
2	3635.1	B=D&U, Z=id	None	None
5	3643.5	B=D&U, Z=id	TR3	None
Random Walk	3818.1	None	None	None
13	Degenerate	B off diagonals	All	None

Table 2.4. Model parameters of the best MARSS model.

Metric	Model Component	Covariate	Model Estimate
Mean S_v	B (Auto-Regressive)	Mean S_v (t – 1)	0.492
Mean S_v	C (Covariate)	24 Hour (cosine)	-0.439
Mean S_v	C (Covariate)	24 Hour (sine)	0.066
Mean S_v	C (Covariate)	24 Hour (total)	0.444
Mean S_v	C (Covariate)	Day Number	0.107
Mean S_v	C (Covariate)	Tidal Range^3	0.077
Mean S_v	C (Covariate)	Tidal Speed^3	0.017
Mean S_v	Q (Process Error)	Mean S_v	0.060
Mean S_v	Z (Scaler)		1.059
Inertia	B (Auto-Regressive)	Inertia (t – 1)	0.459
Inertia	B (Auto-Regressive)	Density Dependence	-0.640
Inertia	C (Covariate)	24 Hour (cosine)	-0.357
Inertia	C (Covariate)	24 Hour (sine)	-0.102
Inertia	C (Covariate)	24 Hour (total)	0.371
Inertia	C (Covariate)	Day Number	0.049
Inertia	C (Covariate)	Tidal Range^3	0.089
Inertia	C (Covariate)	Tidal Speed^3	-0.205
Inertia	Q (Process Error)		0.114
Inertia	Z (Scaler)		1.046
Center of Mass	B (Auto-Regressive)	Center of Mass (t – 1)	0.264
Center of Mass	B (Auto-Regressive)	Density Dependence	0.231
Center of Mass	C (Covariate)	24 Hour (cosine)	-0.515
Center of Mass	C (Covariate)	24 Hour (sine)	-0.156
Center of Mass	C (Covariate)	24 Hour (total)	0.538
Center of Mass	C (Covariate)	Day Number	0.106
Center of Mass	C (Covariate)	Tidal Range^3	-0.017
Center of Mass	C (Covariate)	Tidal Speed^3	0.076
Center of Mass	Q (Process Error)		0.116
Center of Mass	Z (Scaler)		1.139
Aggregation	B (Auto-Regressive)	Aggregation (t – 1)	-0.079
Aggregation	B (Auto-Regressive)	Density Dependence	-0.502
Aggregation	C (Covariate)	24 Hour (cosine)	0.446
Aggregation	C (Covariate)	24 Hour (sine)	-0.109
Aggregation	C (Covariate)	24 Hour (total)	0.459
Aggregation	C (Covariate)	Day Number	0.025
Aggregation	C (Covariate)	Tidal Range^3	-0.060
Aggregation	C (Covariate)	Tidal Speed^3	0.037
Aggregation	Q (Process Error)		0.203
All	R (Observation Error)		0.462

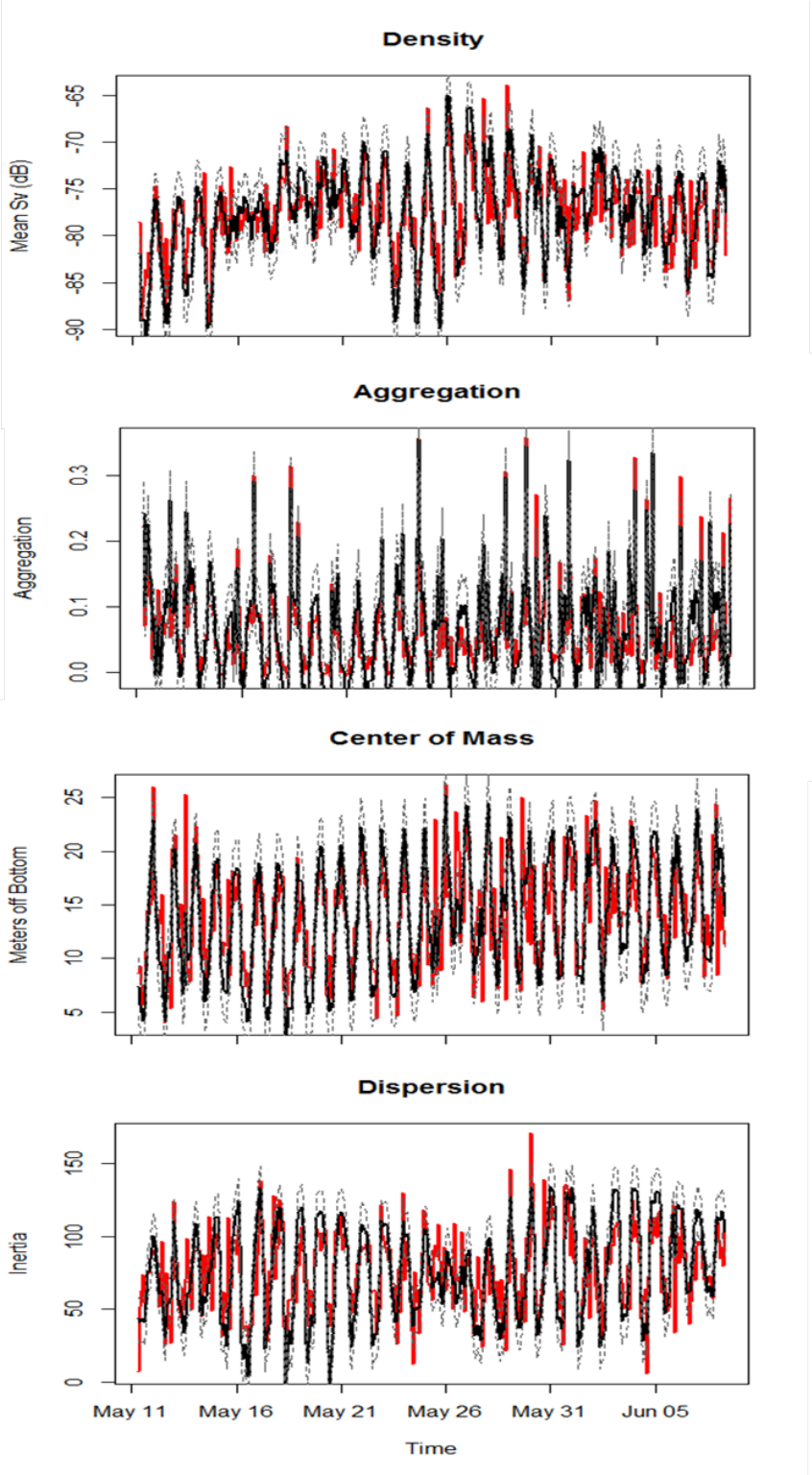

Figure 2.12. Observed (red lines) and MARSS time series models (black lines) of nekton density (top), aggregation (2nd from top), mean weighted location (2nd from bottom), and dispersion (bottom). Modeled values are encompassed by 95% confidence interval (grey dashed line) and generated from best fit Multivariate AutoRegressive State-Space model (MARSS models) as chosen by AICc (Holmes et al. 2012).

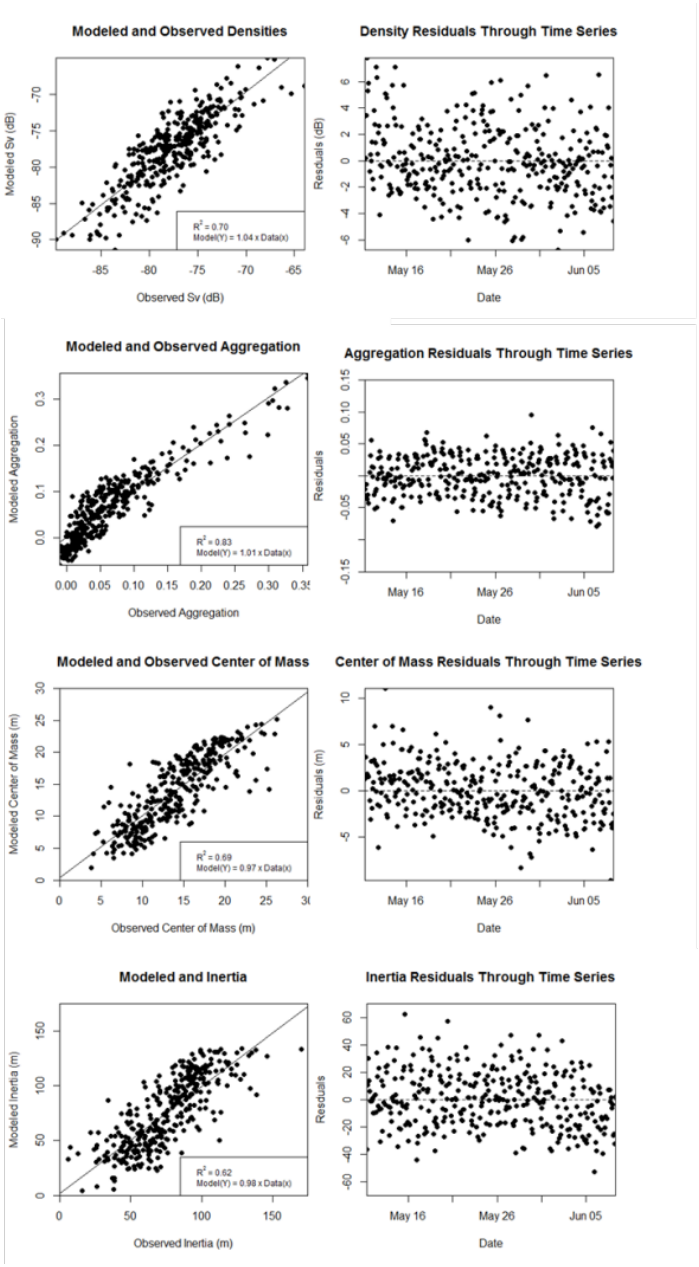

Figure 2.13. (Left) Observed vs. modeled quantities of nekton density and vertical distribution. (Right) Time series of model residuals, demonstrating independence and identical distribution through time.

($R^2_{mean.Sv}$ = 0.70; $R^2_{center.of.mass}$ = 0.69; $R^2_{inertia}$ = 0.62; $R^2_{aggregation}$ = 0.83, Figure 2.13). Caution should be used in interpreting R^2 values due to the presence of the observation error term, artificially inflating the R^2 value.

The relative influence of each environmental covariate on each Echometric series was related by a coefficient (C). The 24-hour Fourier series was the dominant process influencing all four Echometrics ($C_{24.hour(total)->mean.Sv}$ = 0.444; $C_{24.hour(total)->center.of.mass}$ = 0.538; $C_{24.hour(total)->inertia}$ =0.371; $C_{24.hour(total)->aggregation}$= 0.459, Table 2.4). Nekton density increased through time ($C_{day->mean.Sv}$ = 0.107) and to a lesser extent with tidal range ($C_{tidal.range->mean.Sv}$ = 0.077). Nekton mean vertical location was dominated by the 24-hour period, but also increased through time ($C_{day->center.of.mass}$ = 0.106), while decreasing with tidal speed ($C_{tidal.speed->center.of.mass}$ = 0.076). Nekton inertia was inversely related to tidal speed ($C_{tidal.speed->inertia}$ = -0.205), and positively related to Julian day ($C_{day->inertia}$ = 0.049) and tidal range ($C_{tidal.range->inertia}$ = 0.089). Nekton aggregation was dominated by diel period, but was also negatively related to tidal range ($C_{tidal.range->aggregation}$ = -0.060). The autoregressive coefficient (B) between nekton density at sequential time steps was 0.490. Nekton mean-location and inertia were positively autocorrelated ($B_{center.of.mass(t-1)->center.of.mass}$ = 0.264; $B_{inertia(t-1)->inertia}$ = 0.459), while aggregation was slightly negatively autocorrelated ($B_{aggregation(t-1)->aggregation}$ = -0.079). Inertia and aggregation were inversely density-dependent, decreasing proportionally more with nekton density than as an autoregressive function ($B_{mean.Sv(t-1)->inertia}$ = -0.640; $B_{mean.Sv(t-1)->aggregation}$ = -0.502). Nekton center of mass was density-dependent ($B_{mean.Sv(t-1)->center.of.mass}$= 0.231). The error in the process model (Q) was unique for each metric (diagonal and unequal), and relatively small compared to the effects of model parameters ($Q_{mean.Sv}$ = 0.060; $Q_{center.of.mass}$ = 0.116; $Q_{inertia}$ = 0.114; $Q_{aggregation}$ = 0.203). Observation errors (R) were found to be equal across all metrics (R_{all} = 0.462). A complete list of the best fit parameters are summarized in Table (2.4).

2.3.5. Acoustic Technology Comparisons

Echometric series for the acoustic camera (Figure 2.14) and ADCP (Figure 2.15) did not contain the same magnitude of variability as observed in the echosounder series. At night, both the acoustic camera and ADCP characterized significant increases in nekton density (acoustic camera: + 0.57 dB at night, $p < 0.001$, R^2 = 0.010, n = 10,811, Figure 2.14b; ADCP: + 0.45 dB at night, $p < 0.001$, R^2 = 0.009, n = 10,811, Figure 2.15b) and center of mass (acoustic camera: + 0.56 m, $p < 0.001$, R^2 = 0.052,

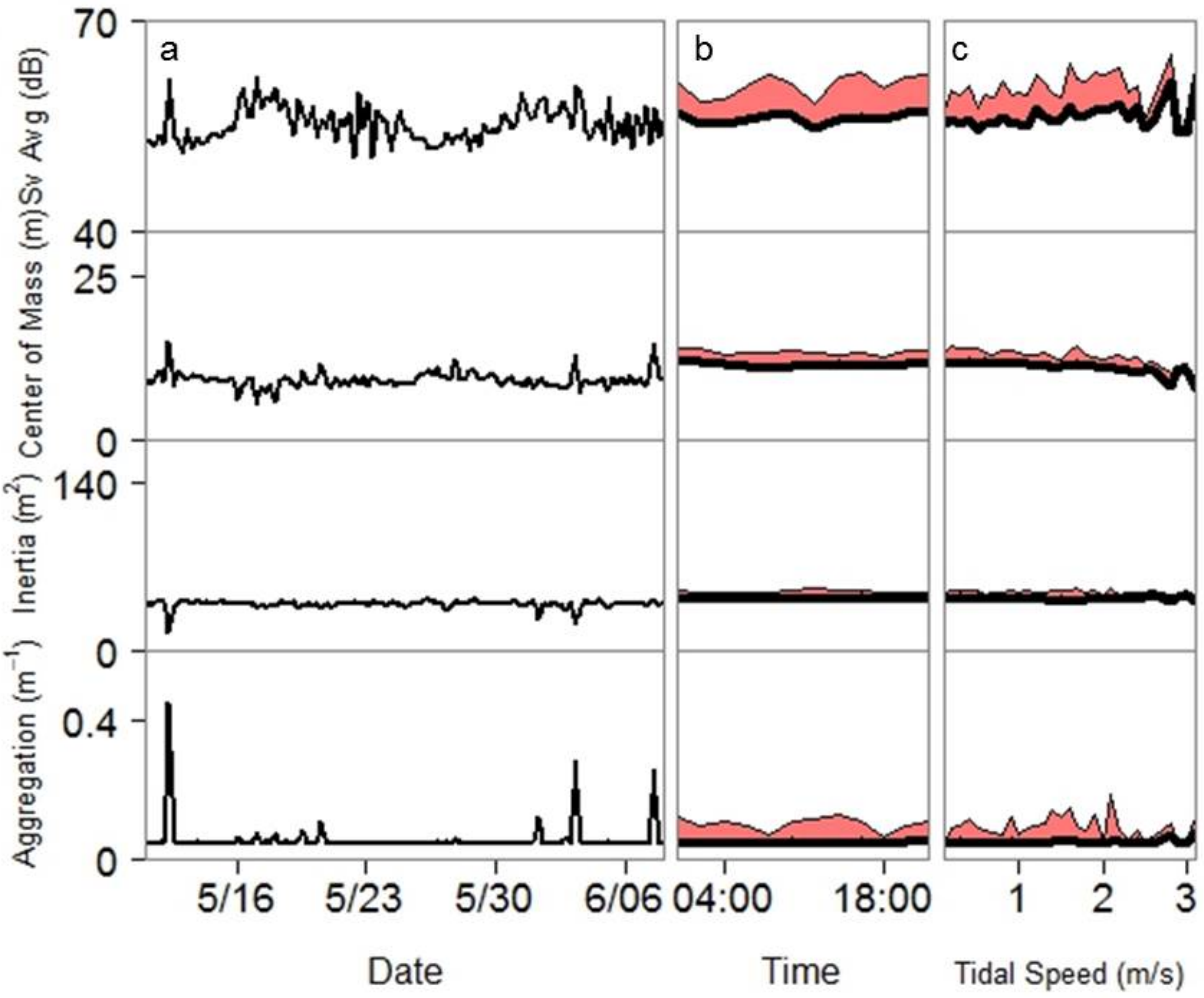

Figure 2.14. Patterns in nekton density and vertical distribution measured from stationary, upward facing acoustic camera. Density and vertical distributions were indexed as a function of (a) time, (b) time of day (mean + 2 standard deviations), and (c) tidal speed (mean + 2 standard deviations). From top to bottom, the ordinate quantities are density (metric: mean S_v; units: dB, re 1 µPa), mean weighted location from bottom (metric: center of mass, units: m), dispersion (metric: inertia; units: m^2), and aggregation (metric: aggregation index; units: m^{-1}).

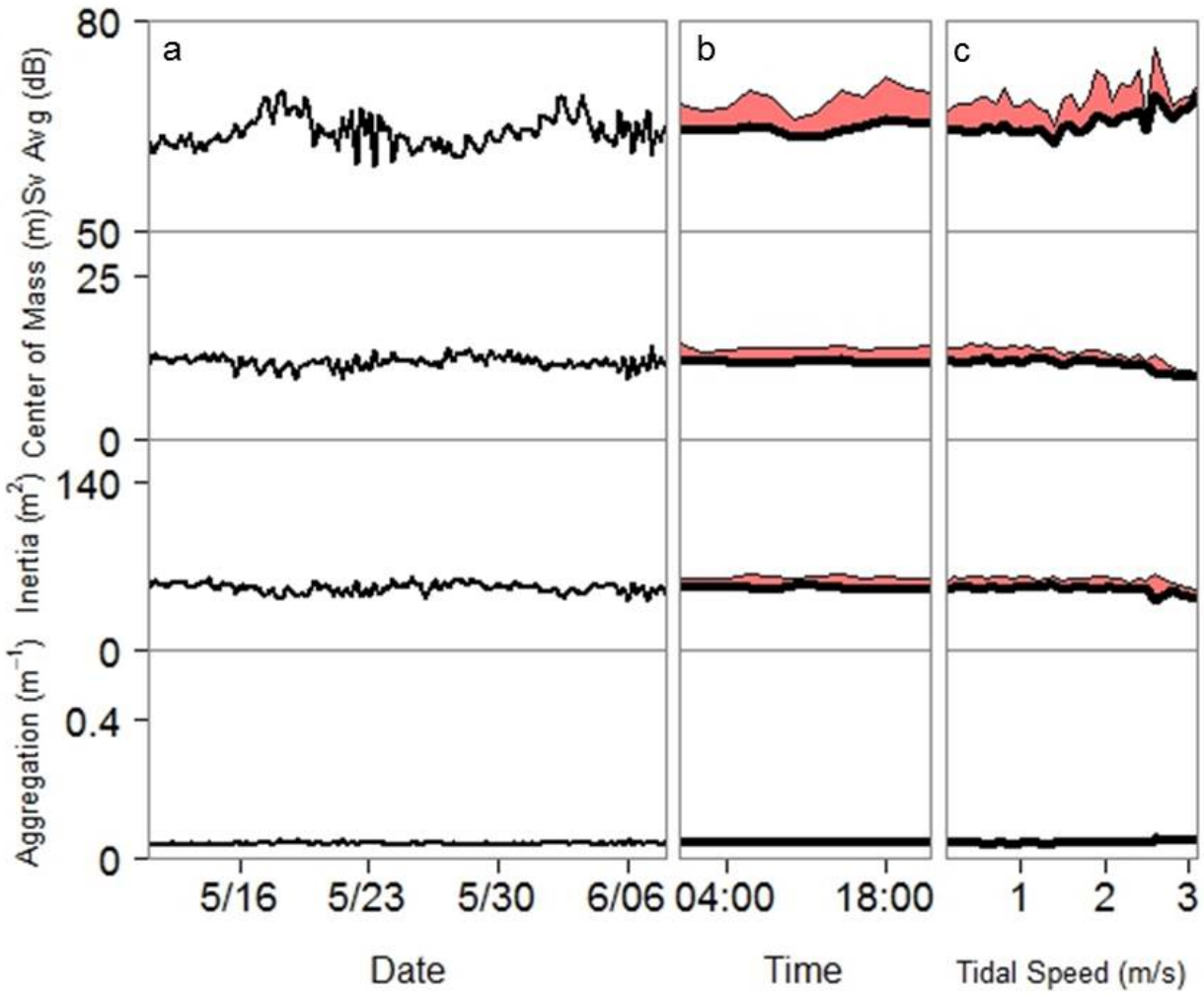

Figure 2.15. Patterns in nekton density and vertical distribution measured from stationary, upward facing ADCP. Density and vertical distributions were indexed as a function of (a) time, (b) time of day (mean + 2 standard deviations), and (c) tidal speed (mean + 2 standard deviations). From top to bottom, the ordinate quantities are density (metric: mean S_v; units: dB, re 1 µPa), mean weighted location from bottom (metric: center of mass, units: m), dispersion (metric: inertia; units: m^2), and aggregation (metric: aggregation index; units: m^{-1}).

n = 10,811 Figure 2.14b; ADCP: + 0.36, $p < 0.001$, $R^2 = 0.019$, n = 10,811, Figure 2.15b), but not the same magnitude as the echosounder (+ 3.51 dB, + 5.61 m). Both the acoustic camera and ADCP observed lower dispersions of nekton at night, which contrasts with the pattern in the echosounder echometric series.

In contrast to the echosounder, nekton density (*i.e.* mean S_v) increased with tidal speed in the acoustic camera (slope = 0.87 $dB(m/s)^{-1}$, $p < 0.001$, $R^2 = 0.053$, n = 10,130) and ADCP data (slope = 0.70 $dB(m/s)^{-1}$, $p < 0.001$, $R^2 = 0.041$, n = 10,130). Yet, both technologies observed significant decreases in nekton center of mass (acoustic camera: slope = -0.55 $m(m/s)^{-1}$, $p < 0.001$, $R^2 = 0.114$, n = 10,130; ADCP: slope = -0.30 $m(m/s)^{-1}$, $p < 0.001$, $R^2 = 0.033$, n = 10,130) and dispersion (acoustic camera: slope -0.20 $m^2(m/s)^{-1}$, $p < 0.001$, $R^2 = 0.002$, n = 10,130; ADCP: slope = -0.50 $m^2(m/s)^{-1}$, $p < 0.001$, $R^2 = 0.005$), consistent with the echosounder.

At the finest resolution (24 s by 1 m analysis cell), mean S_v measured by the echosounder was positively related to the relative mean S_v measured by the acoustic camera ($p < 0.001$, $R^2 = 0.016$, Figure 2.16a) and the ADCP ($p < 0.001$, $R^2 = 0.008$, Figure 2.16b). Variance in nekton density increased in both the acoustic camera and ADCP measurements as the echosounder mean S_v measurements increased.

The relative ability of the stationary acoustic technologies to characterize vertical distributions of nekton through the water column at a given time was examined by comparing pairs of echometric values between the echosounder and the acoustic camera (Figure 2.17) or the ADCP (Figure 2.18) at a resolution of 24 s temporal and 1 m vertical bins. A significant and positive relationship between coincident measures of density ($p < 0.001$, $R^2 = 0.018$) and center of mass ($p < 0.001$, $R^2 = 0.023$) occurred between the echosounder and the acoustic camera. There were no significant relationships in the inertial and aggregation index values between the echosounder and the acoustic camera (Figure 2.17, Table 2.5). Relationships in echometric values between the echosounder and the ADCP differed depending on the metric (Figure 2.18, Table 2.6). Mean S_v was positively related between the two technologies ($p < 0.001$, $R^2 = 0.009$) with the variance increasing with the amplitude of the echosounder. There were no positive relationships in the center of mass, or aggregation index comparisons (Table 2.5).

Table 2.5. Correlation between stationary acoustic camera or ADCP with stationary echosounder in quantities of nekton density and vertical distribution at a 24 second temporal resolution. CoM represents center of mass and AI represents aggregation.

	Acoustic Camera				ADCP			
Metric	Density	CoM	Inertia	AI	Density	CoM	Inertia	AI
P-value	< 0.001	< 0.001	0.374	0.301	< 0.001	0.087	< 0.001	0.052
R^2	0.018	0.023	< 0.001	< 0.001	0.009	< 0.001	0.013	< 0.001

Table 2.6. Correlation between stationary acoustic camera or ADCP with stationary echosounder in quantities of nekton density and vertical distribution at a 12-minute temporal resolution. CoM represents center of mass and AI represents aggregation.

	ADCP				Acoustic Camera			
Metric	Density	CoM	Inertia	AI	Density	CoM	Inertia	AI
P-value	0.033	0.523	0.175	0.292	< 0.001	0.005	0.097	0.938
R^2	0.010	< 0.001	0.002	< 0.001	0.029	0.019	0.005	-0.003

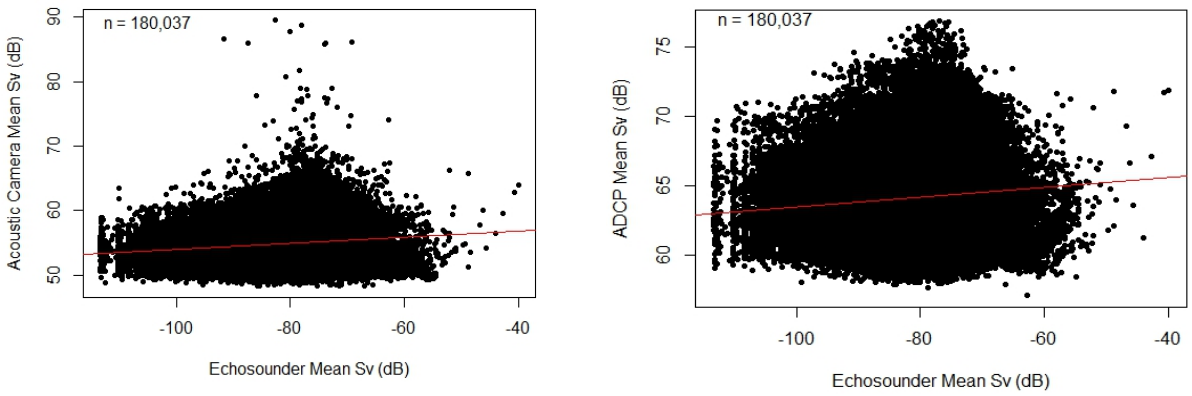

Figure 2.16. Concurrent measurements of nekton density from the stationary echosounder and acoustic camera (left) or ADCP (right) collected at a temporal resolution of 24 seconds and vertical resolution of one meter.

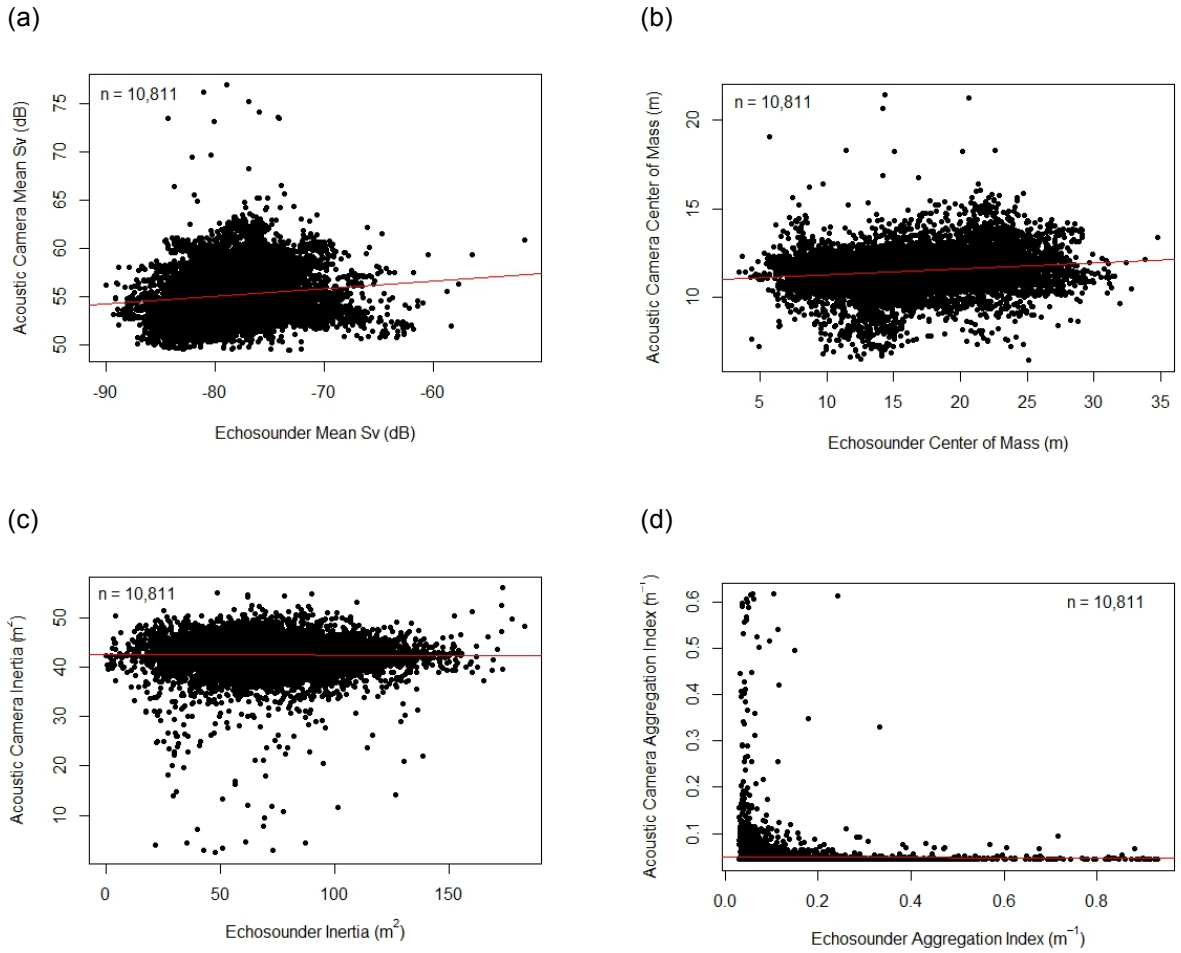

Figure 2.17. Concurrent water column summary statistics of nekton (a) density (units: dB re 1 µPa), (b) mean weighted location (units: m), (c) dispersion (units: m^2), and (d) aggregation (units: m^{-1}) between a stationary, upward facing acoustic camera and echosounder collected at a 24-second temporal resolution.

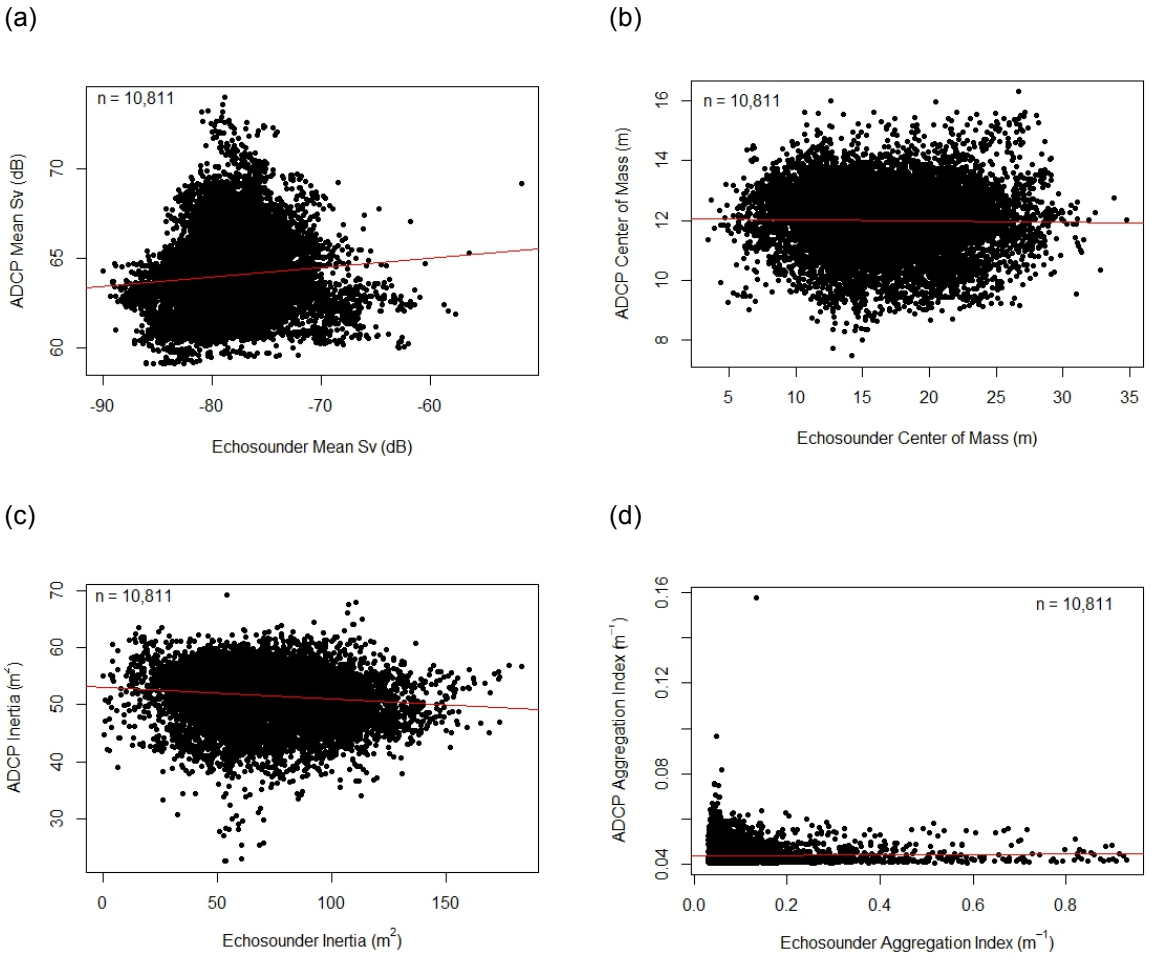

Figure 2.18. Concurrent water column summary statistics of nekton (a) density (units: dB re 1 µPa), (b) mean weighted location (units: m), (c) dispersion (units: m^2), and (d) aggregation (units: m^{-1}) between a stationary, upward facing ADCP and echosounder collected at a 24-second temporal resolution.

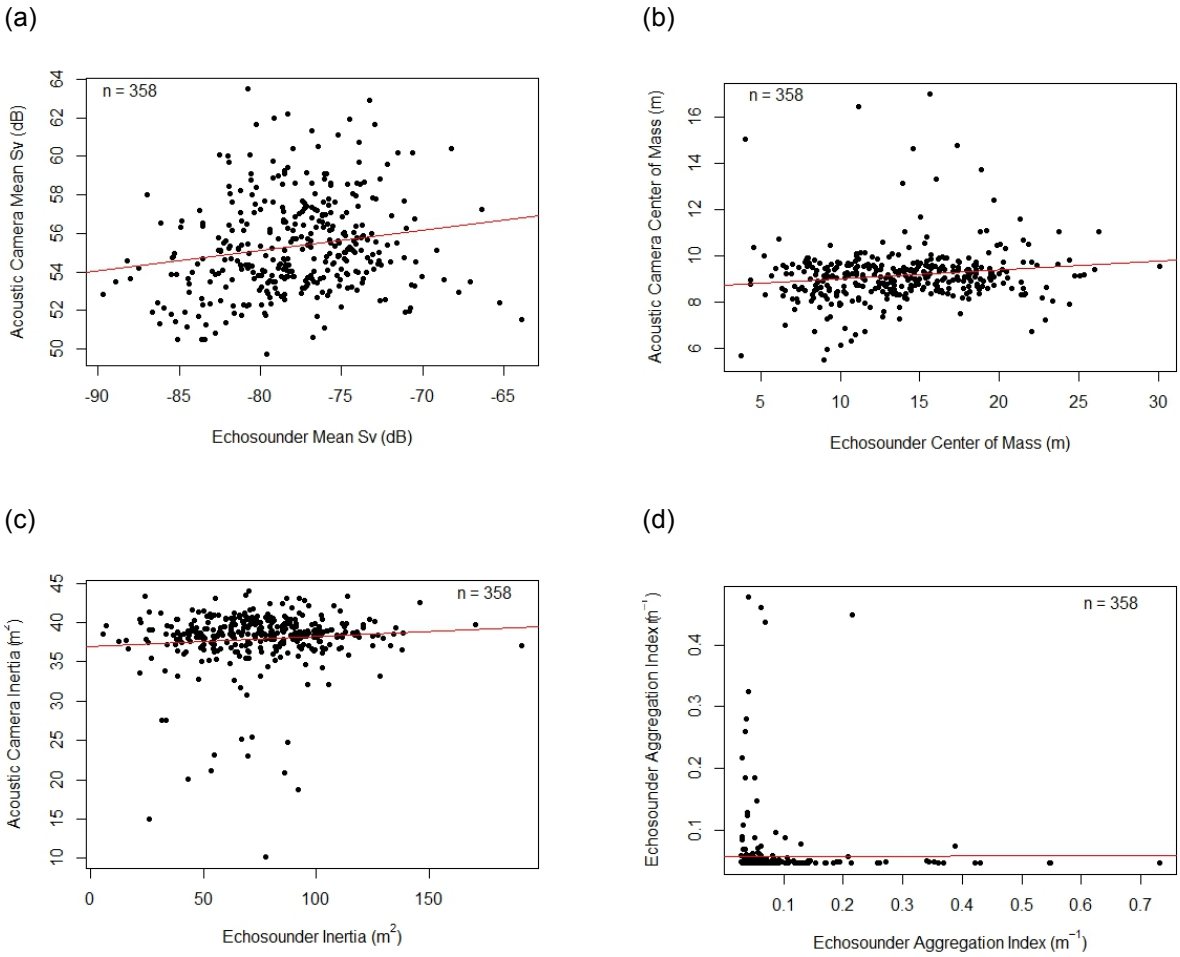

Figure 2.19. Concurrent water column summary statistics of nekton (a) density (units: dB re 1 µPa), (b) mean weighted location (units: m), (c) dispersion (units: m^2), and (d) aggregation (units: m^{-1}) between a stationary, upward facing acoustic camera and echosounder collected at a 12-minute temporal resolution.

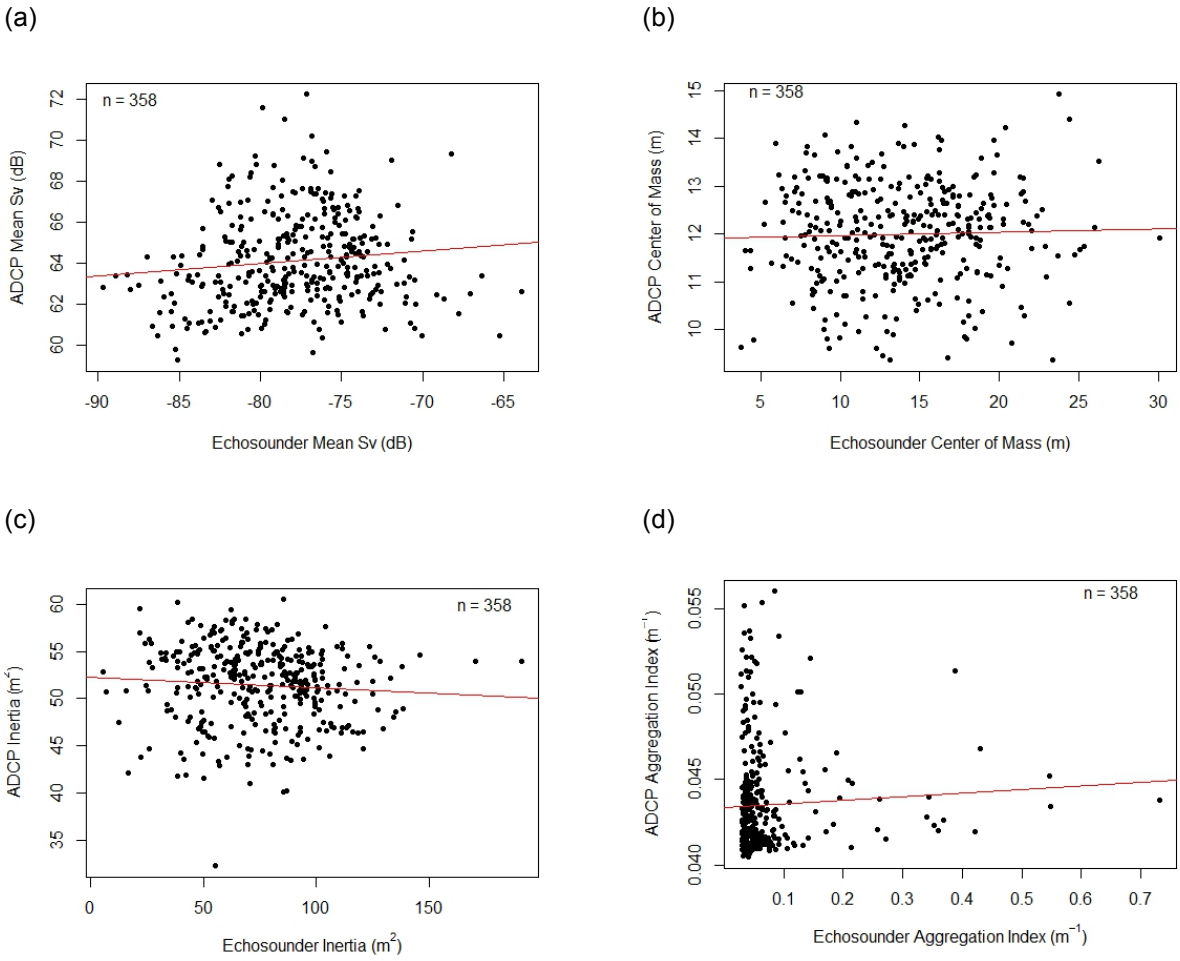

Figure 2.20. Concurrent water column summary statistics of nekton (a) density (units: dB re 1 µPa), (b) mean weighted location (units: m), (c) dispersion (units: m^2), and (d) aggregation (units: m^{-1}) between a stationary, upward facing ADCP and echosounder collected at a 12-minute temporal resolution.

Comparisons between the echosounder and the acoustic camera (Figure 2.19) and ADCP (Figure 2.20) were also conducted using 12-minute temporal bins to investigate the presence of a scale-dependent pattern. The decrease in resolution decreased variability in measurements of nekton density and distribution that may have confounded relationships at the finer (*i.e.* 24 second) temporal resolution. Decreasing the temporal grain size reduced the sample to 358 concurrent samples. When comparing the acoustic camera to the echosounder, there were significant relationships in the mean S_v (Figure 2.19a, Table 2.5; $p < 0.001$, $R^2 = 0.029$) and center of mass (Figure 2.19b, Table 2.5; $p = 0.005$, $R^2 = 0.019$), but no relationships in inertia (Figure 2.19c, Table 2.5) or aggregation index (Figure 2.19d, Table 2.5). Probability and significance values are summarized in Table (2.5).

Comparison of ADCP to echosounder data binned at 12 minute intervals resulted in significant relationships with the mean S_v (Figure 2.20a, Table 2.6; $p = 0.033$, $R^2 = 0.010$). Variance in the ADCP measurement of nekton density increased as nekton density increased. No trends were significant in the center of mass (Figure 2.20b, Table 2.6), inertia (Figure 2.20c, Table 2.6), or aggregation (Figure 2.20d, Table 2.6) comparisons.

2.4. Discussion

Tidal currents at MHK sites add a layer of complexity to temporal patterns of nekton density and vertical distribution. Nekton densities and vertical distributions at the Admiralty Inlet site varied through time, but were in phase with periodic physical processes at the site. If coincident cycles in physical and biological processes are assumed to be evidence of bio-physical coupling, then the relative influence of physical processes can be inferred from the amplitude of variance at corresponding temporal periods (Platt & Denman 1975, Steele et al. 1994). The global wavelet spectrum measures the variance contributed by each period, and thus can be used as one measure of the relative influence of physical processes on nekton density distributions. MARSS models with z-score standardized metrics and environmental covariates allowed for the direct comparison of influence of each covariate on each metric, providing two independent measures of the influence of each period or covariate. Both the global wavelet spectrum and the MARSS models identified the 24-hour period as the dominant source of nekton variability, consistent with diel vertical migrations (Neilson & Perry 1990, Axenrot et al. 2004, Benoit-Bird & Au 2004). This result contrasts to the observation that nekton density and vertical distributions were

predominantly influenced by tidal velocities at a tidal current MHK site in New York's East River (NYSERDA 2011).

Even though tidal speeds were hypothesized to dominate nekton density distributions based on previous measurements (NYSERDA 2011), both the global wavelet spectrum and MARSS models identified tidal speed and tidal range as secondary influences. The global wavelet spectrum identified similar magnitudes of variance in nekton vertical distributions at the fortnightly lunar period (*i.e.* tidal-range) as at the 12.5 hour, semi-diurnal period of tidal cycles, or 6.25 hour period of tidal velocities, suggesting that tidal range may also influence nekton density distributions. However, the ability to identify fortnightly periods in the global wavelet spectrum was constrained by the short sampling extent relative to fortnightly tidal cycles. The time series was padded with zeroes to analyze the wavelet power near the beginning and end of the series, dampening the global wavelet spectrum at large periods. For this reason, the MARSS model may be a better indicator of the true influence of tidal range compared to tidal speed. The MARSS models included tidal range in the best-fit model, with higher influence over nekton density and aggregation than tidal speed. Fish behavior and availability to sampling is known to change as a function of lunar period (*e.g.* Bos & Gumanao 2012), but was not thought to strongly influence nekton density distribution at MHK tidal sites (NYSERDA 2011). But the influence of tidal cycles extends beyond the observed fortnightly periodicities, as changes in the period of variance in mean S_v, center of mass, and inertia were observed during the neap tide on May 26th. With only one neap tide in the series it is impossible to know if the corresponding deviation in variability was a coincidence or a pattern. A longer sample series is required to identify whether patterns of nekton density and vertical distribution change as a result of neap tides.

Although the MARSS models and global wavelet spectrum identified similar processes, the MARSS models had a analytical advantages when compared to global wavelet spectrum. The most pronounced advantage was the MARSS model's increased sensitivity to identify tidal speed, tidal range, and Julian day, which were not identified by the global wavelet spectrum. Unlike the global wavelet spectrum, which only measures the amplitude of variance, MARSS models identify whether there is a positive or negative relationship between covariates and metrics, and quantifies the error in both the process model and observation. The observation component of MARSS models did not identify any

environmental covariates as significantly influencing the measurements of nekton density or vertical distribution, reinforcing that the echosounder is a viable tool for domain monitoring at tidal MHK sites and that there was no bias in the results due to the method.

This baseline characterization of nekton density distribution through time can be used to identify instances of high risk of biological interactions with a MHK device. Risk is the product of the probability of an event occurring and the severity of that event. Using this definition, the probability of a fish-device interaction is related to the vertical distribution of nekton and the severity to nekton density. Assuming that nekton densities and vertical distributions are not changed by the presence of a device, then the probability and severity of biological interactions are related to the both the mean and variance of nekton density. Increases in the mean nekton density or a decrease (i.e lowering) in the mean weighted, vertical location increase the severity and the probability of occurrence of an event (*i.e.* the *mean* risk of interaction). Increases in the variance of a metric increases the likelihood of an extreme interaction such as a dense aggregation of fish close to the bottom. Using this logic, the risk given a set of environmental conditions can be inferred from the MARSS models of nekton density and vertical distribution. MARSS models indicated that nekton are more dense and concentrated lower in the water column at high tidal speeds and at maximum tidal ranges occurring during daylight hours. These conditions coincide with peak energy production periods, indicating that the mean risk of biological interactions is related to potential energy production. In contrast, the statistically significant peak in scale-averaged variance of nekton density was associated with troughs in the tidal range, a day in which potential energy production would be minimized. If troughs in tidal range are associated with peaks in the variance of nekton density (*i.e.* the variance of risk), then we'd expect a heightened risk of extreme biological interactions occurring fortnightly during neap tides. Taken together, I conclude that the mean risk of biological interactions is increased in environmental conditions associated with peak potential energy production, while the risk of an extreme event is maximized during low energy production, neap tides.

Using estimates of risk to predict biological interactions with MHK devices makes several assumptions. First, that nekton densities and vertical distributions will not be altered by the presence of a MHK device. Second, that risk scales with nekton density, vertical distribution, and variance in density. Notably, risk estimates do not make assumptions about any mechanisms through which nekton and a

device interact, only that nekton within the vertical footprint of a device have a greater probability of interacting with a device. The small error in both the process and observation models of MARSS time series models of nekton density distributions relative to the influence of covariates suggest that the time series model could be used in a limited predictive capacity. The predictive capacity of the best-fit time series model was not tested, and would likely break down quickly due to the auto-regressive framework that compounds modeling errors through time. Given continuous near-real-time monitoring, predictions of risk, even a few hours in advance, could be used to modify operation of MHK devices to minimize or mitigate potential biological interactions. Even if MARSS models are not used to predict, knowledge of how environmental covariates influence nekton density and vertical distributions can be used to identify environmental conditions associated with potential increases in nekton density or vertical overlap with a device. Scale-averaged wavelet power, a proxy for risk of extreme events, cannot be calculated in real-time due to the limitations of edge effects in wavelet analysis. Still, future research could model scale-averaged wavelet power to identify the environmental conditions that increase the probability of extreme events.

Similar patterns in nekton density distributions were observed between mobile and stationary surveys. The stationary survey, consistent with its higher temporal scope, was able to identify temporal patterns in nekton behavior due to diel vertical migrations and tidal currents that could not be resolved in the mobile survey. The observed biodiversity in trawl catches are difficult to compare to other sites due to the lack of historical direct sampling at tidal MHK sites. The trawls collected 41 different species of fish, compared to 115 that have historically been observed at the site (DeLacy et al. 1972), and there is no record of where those species were sampled relative to the pilot MHK site. Trawl catches were included in this thesis to help identify species observed within acoustic backscatter and to inform future Admiralty Inlet monitoring programs of the dominant fish species, and their length distributions.

The omission of environmental covariates describing observation error in the final MARSS model provides evidence that echosounder measurements were not significantly biased by tidal currents, reaffirming that the echosounder is the standard by which to compare other acoustic technology's ability to monitor MHK sites. Nekton density and vertical distribution measured by the stationary echosounder varied as a function of time of day and tidal currents. These patterns were not observed in the backscatter

data from the acoustic camera or the ADCP. Coincident measurements of nekton density and vertical distribution measured by the ADCP and acoustic camera were loosely correlated to measurements from the calibrated echosounder, suggesting either fine scale (< 200 m) spatial heterogeneity in nekton between devices or imprecise measurements by the ADCP and acoustic camera. Patterns in the observed variability of nekton density and vertical distribution measured by the acoustic camera and ADCP were either inconsistent with or smaller in magnitude than those measured by the echosounder. Based on the ability of the calibrated scientific echosounder to identify patterns not present in the ADCP or acoustic camera data, the echosounder is recommended as the technology to monitor pelagic nekton density and distribution at MHK sites. Acoustic cameras and ADCPs will be deployed at MHK sites to characterize tidal flow properties and to monitor near-field nekton interactions with devices, regardless of pelagic monitoring requirements, but they cannot be relied on to characterize nekton distribution patterns.

This study provides a case study for baseline domain monitoring at a proposed MHK tidal site. Results from this study also provide a framework to analyze baseline data, and to compare post-perturbation measurements during energy production or decommissioning MHK sites. Changes in the mean or median of metrics can be tested using an ANOVA or notched box-plot, respectively. Unfortunately, ANOVA models comparing pre- and post-installation measurements are confounded by variability in nekton as a function of covariates. MARSS time-series models can decouple the added variance in nekton density distributions from environmental covariates, and can identify perturbations in nekton communities once devices are installed. Wavelet analysis can be used to quantify cyclical variability, including measuring differences in the amplitude of the variance or the scales at which communities change after MHK device installation. Finally, baseline data can be used to infer conditions of heightened risk. During periods of heightened risk, monitoring efforts can be increased or pre-emptive operational changes can be initiated to mitigate interactions. When data collection rates potentially overwhelm analysis rates, one alternative to taking random subsamples of data for monitoring analyses would use results from MARSS models to identify high-risk conditions for important variables and increase monitoring efforts or alter operations during these times.

These methods provide a framework to characterize baseline nekton density and vertical distributions at MHK sites, but the general approach is applicable to other marine monitoring programs.

Advances in remote sensing are shifting the approach to environmental monitoring in coastal areas from direct surveys to remote sensing technologies (Brando & Phinn 2007), enhancing both the cost effectiveness and resolution of monitoring programs. Remotely deployed stationary echosounders measured nekton density and vertical distribution at fine spatial and temporal resolution, enabling the quantitative description of patterns through time. Quantitative descriptions of patterns and periodicities in baseline measurements of pertinent quantities can be used to make inferences about potential biological effects of any marine development, broadening the application of this approach.

Chapter 3: Comparison of Methods to Calculate the Representative Range of Point Measurements: Implications for Ecological Network Design

3.1. Introduction

Regional questions of aquatic community distribution patterns and influencing processes are large and complex, with species varying and interacting through space and time over a range of scales (Steele et al. 1994, Wu 1999). Regional ecological complexity precludes the ability to measure all interacting variables, so inferences must be drawn from samples. Sampling effort, instrumentation, and deployments are limited by logistics (*i.e.* time and resources). Samples are indexed by time, space, or a combination of the two depending on the variable of interest and the sampling technology. Traditionally aquatic species distributions have been sampled using mobile surveys (*e.g.* ship-based, abundance estimates), collecting discreet or continuous spatially-indexed measurements of density, abundance, or biomass. However, it takes time for a vessel to survey space, potentially convolving spatial and temporal variability when the geographic sampling domain is large. Depending on the magnitude of spatial and temporal variability within the domain, the convolution of time and space can bias observed patterns (Martin et al. 2005). Technological advancements in remote sensing technologies, computer processing, data storage, and data management have broadened the array of available sampling techniques for large spatial domains, which increases the range of possible ecological analyses (*e.g.* Barau & Ludin 2012). As an example, biological samples can be obtained from spatially distributed, point-source sensors within integrated networks to provide high temporal resolution, spatially distributed samples over time (*e.g.* Porter et al. 2005).

The enhanced temporal scope (*i.e.* the resolution of measurements relative to the range) of stationary sensor networks increases the statistical power to identify ecological patterns across temporal scales. Since ecosystem management depends on the ability to understand ecosystem patterns and processes (*e.g.* Thiel et al. 2007), increased statistical power increases the ability to detect change in the mean (Fairweather 1991, Mapstone 1995, Osenberg et al. 1994) and variance (Underwood 1991, Morgan et al. 1994, Landres et al. 1999) of ecologically pertinent variables. In a monitoring context, pre-perturbation measurements are used as a baseline to provide a post-perturbation comparison to quantify the magnitude and assess the impact of change (Underwood 1991). Each stationary sensor, collecting data before and after a

perturbation, functions as paired pre- and post-installation measurements controlled for spatial variability. Increasing the number of paired pre- and post-perturbation measurements for comparison increases the statistical power to identify effects of change in monitored variables (Underwood & Chapman 2003).

Organism distributions are patchy (Levin 1992) and autocorrelated in space (Legendre 1993), adding complexity when interpreting point source density or abundance data. Since biological similarity decays with geographical distance (Legendre 1993, Soininen et al. 2007), uncertainty is introduced when interpolating point source measurements across space. The decay in similarity with distance has been attributed to heterogeneity in physical habitats (Nekola & White 1999), biological aggregation (Roughgarden 1977), predation (Wiens 1976), and patchiness produced by environmental constraints on organismal dispersal (Garcillán & Ezcurra 2003) or physiological limitations (*e.g.* neutral theory, Hubbel 2001). Distance decay in similarity within biological communities and their environment leads to the observed scale-dependence of biological variability (Wiens 1989), compared to random processes, which demonstrate uniform variation across all spatial and temporal scales (*i.e.* scale-independence; Gilman et al. 1962). The consequence of distance decay is that the degree to which sample *A* resembles sample *B* decreases with increasing distance until point measurements can no longer be considered homogenous. Interpolation of point measurements beyond this range increases uncertainty and interpretation errors (Milewska & Hogg 2001, Martin et al. 2005, Anttila et al. 2008). If the objective is to represent an area or volume, efforts to collect additional measurements within this range (*i.e.* at finer spatial resolutions) are sub-optimally allocated and could be used to increase the extent of the survey. Rooted in Tversky and Kahneman's (1974) psychological concept of "representativeness heuristics", the maximum range to which point-measurements can be used to resolve spatial variability in the surrounding domain has been termed the "spatial representativeness" of point-source samples (Janis & Robeson 2004). When solving complex problems in uncertain circumstances, "people typically rely on the representativeness heuristic, in which probabilities are evaluated by the degree to which A is representative of B, that is, by the degree to which A resembles B" which creates predictable and systematic errors (Tversky &

Kahneman 1974). Rather than using the term “spatial representativeness”, we will use “representative range” to avoid the wrath of our secondary education English teachers who forbade the use of derivational suffixes in a non-discriminatory manner (*e.g.* “ness monsters”).

The concept of representative range evolved in meteorology to optimize networks of rain gauges and thermometers (Brooks 1947, Huff & Neill 1957). At the onset, it was realized that optimum sensor density was dependent on the focal quantity (*e.g*. temperature, rainfall.) and objective, forecasting or hindcasting of a monitoring network (Brooks 1947). Early studies of meteorological network design focused on the required number of sensors or gauges randomly placed to achieve a predetermined accuracy of the mean of a quantity through a spatial field (*e.g.* Rycroft 1949). It was soon realized that spatial structure influenced the representative range of sensors within networks, and the focus shifted from the number of sensors to the spacing between sensors (Hershfield 1965, Hutchinson 1969). Representative range estimates calculated using spatial autocorrelation assumes homogenous or smooth decay between sensors (Hutchinson 1969). In the late 1960s, the focus of network optimization changed from spatial autocorrelation between sensors to the relative error introduced by spatially interpolating points (Gandin 1970) or areas (Kagan 1966). Meteorological networks are often composed of sensors that must be stationary (*e.g.* rain gauges), inhibiting *a priori* measurements of spatial variability to estimate network representative range. This limitation prompted Rodda (1971) to identify *a priori* optimization of sensor density as the principal objective of network design. Despite this shortcoming, methods proposed in 1960s and 1970s have recently been used for sensor network optimization (*e.g.* Milewska & Hogg 2001, Ciach & Krajewski 2006). Since the 1970s, representative range studies diversified to focus on the effects of spatial and temporal analytic cell size (*i.e.* binning; Ciach & Krajewski 2006), and *post-hoc* network optimization such as cluster analysis (*e.g.* Sulkava et al. 2011) and variogram nugget time series (*e.g.* Janis & Robeson 2004). Approaches developed within other disciplines’ specific applications were derived in isolation, producing a spectrum of sampling and analytical approaches, and collectively lacking a standardized threshold or definition of “representative” (Janis & Robeson 2004, Ciach & Krajewski 2006). A consensus has yet to be reached on the best technique to calculate

representative range of static sensor networks (*c.f.* Milewska & Hogg 2001, Janis & Robeson 2004, Anttila et al. 2008).

A considerable amount of effort has also been dedicated to examining the correlation, coherence, and permanence of ecological quantities in time and space (Legendre 1993, Posadas et al. 2006, Soininen et al. 2007), but few ecological studies have incorporated this structure to spatial and temporal design of monitoring programs (*e.g.* Rhodes & Jonzén 2011). Several studies, rooted in the reality that monitoring networks are usually resource limited, have quantified the optimal spatial and temporal allocation of a pre-determined pool of sampling effort based on spatial and temporal biological variability (*e.g.* Gray et al. 1992, Kitsiou et al. 2000, Rhodes & Jonzén 2011), or have optimized sensor density or allocation of established networks (*e.g.* Siljamo et al. 2008). The challenge when applying representative range calculations to ecological point sensors is identifying a threshold of what is considered "representative" with a meaningful biological interpretation. The first study to focus on the implications of representativeness range in ecological modeling was Jacobs (1988), who used autocorrelation models to investigate the representativeness of an arctic climate sensor network that was incorporated in muskoxen and caribou population models. The United Nations' Food and Agriculture Organization (FAO) released a technical paper (Gray et al. 1992) devoted to the biological assessment of marine pollution effects on benthos, which described quantitative and qualitative techniques to estimate the number of replicate and the optimal spatial allocation of random samples. Anttila et al. (2008) incorporated both autocorrelation and interpolation error in a study of water quality sensors in inland lakes. In another study, structure functions were used to quantify the independence of measurements in space as a function of range to estimate the spatial and temporal representativeness of the timing of birch tree blooming events in Europe (Siljamo et al. 2008). To our knowledge, the first *a priori* optimization of an ecological sampling network occurred in 2013, where cluster analyses were used to identify homogenous Alaskan eco-regions for sensor placement (Hoffman et al. 2013). Even though temporal variance is known to change through space (Damian et al. 2003, Certain et al. 2007), estimates of representative range have focused on the distance decay of the mean of a quantity and not the variance.

This study was undertaken to compare six methods used to define representative ranges of point measurements using fish densities collected by active acoustic echosounders in Puget Sound, WA.

3.2. Materials & Methods

Six methods were chosen to quantify the representative range of temporal point measurements (Table 3.1). Four of these methods estimate the representative range of the mean of a quantity, with the remaining two estimating the representative range of the variance. The six methods mirror the evolution of techniques used to optimize meteorological sensor networks, and can broadly be categorized into four approaches: 1). Distance between sensors based on the spatial correlation, 2). Sample size calculations assuming random sampling to detect a minimum threshold of change, 3). Scales at which spatial and temporal variability are equivalent, and 4). Maximization of spatial variance.

The first approach calculates the optimum distance between sensors based on the relationship of spatial measurements. Only one method was examined within this approach, using empirical measurements to model the decay of spatial autocorrelation with distance (*e.g.* Anttila et al. 2008). The range at which measurements become independent is the range that measurements are considered representative. This method evolved in the mid- to late 1960s in meteorology (Hershfield 1965), and has the most widespread acceptance in biological or ecological studies (*e.g.* Jacobs 1988, Anttila et al. 2008).

Historically, spatial autocorrelation models of representative range evolved to models of interpolation error (*e.g.* Kagan 1966, Gandin 1970, Milewska & Hogg 2001). Lacking a meaningful error threshold to determine representative range, the interpolation error was not explicitly used to calculate a representative range, but was used to describe the uncertainty introduced by adopting each approach or method. In this study, interpolation error curves, for linear and areal interpolation, are used to quantify the error introduced by each of the four methods used to quantify the representative range of the mean.

The second approach assumes a random sampling framework to identify biological changes through space or time (*e.g.* Rycroft 1949). Assuming sensors collect data at fixed points

Table 3.1. Properties of all six methods examined to estimate the representative range of ecological point sensors.

Method	Quantity Property	Spatially Explicit?	Analytical Approach	Root or Reference
Gray's Sample Size Calculation	Mean	No	Paired *t*-test/Repeated Measures ANOVA	Gray et al. (1992)
t-test Sample Size Calculation	Mean	No	Paired *t*-test/Repeated Measures ANOVA	Sullivan (2006)
t-test Power Analysis	Mean	No	Paired *t*-test/Repeated Measures ANOVA	Zar (2010)
Coefficient of Determination Model	Mean	Yes	Autocorrelation	Anttila et al. (2008)
Theoretical Spectra	Variance	Indirectly	Modeled Spatial Power Spectra	See: Gilman et al. (1962)
Equivalent Spatial and Temporal Scales	Variance	Indirectly	Empirical Spatial and Temporal Power Spectra	See: Wiens (1989)

before and after a perturbation, the number of sensors can be calculated from a paired *t*-test sample size calculation. Three proposed methods fit within the random sampling approach: Gray et al. (1992) calculated the number of required replicates using a derivative of minimum sample size calculations for a paired *t*-test or repeated measures ANOVA (Sullivan 2006), the repeated measures, paired *t-test* was used as the second method, and the third method is a sample size calculation for a paired *t*-test including statistical power (Zar 2010).

Although changes in temporal variance can be used as a secondary metric of biological change (Underwood 1991), there is no reason to assume that temporal variance matches the spatial structure of the mean (as spatial models of temporal variance differ from spatial models of the mean; *c.f.* Damian et al. 2003, Sampson et al. 2001). To illustrate using examples, Certain et al. (2007) demonstrated spatial heterogeneity in the temporal variance of seabird populations and Damian et al. (2003) provided a method to assess spatial heterogeneity in the temporal variance of precipitation. No studies have proposed methods to quantify the representative range of temporal variance measurements.

Point measurements of temporal variance have an equivalent spatial range over which they can be interpolated. The third and fourth approaches quantify representative ranges (*i.e.* spatial period) of temporal variance, which necessitates a switch from the spatial to frequency domain. The third approach modeled the theoretical power spectrum as a function of the spatial autocorrelation model developed for the second approach. The spatial period at which 95% of the maximum observed variance in fish density was observed was set as the representative period of variance. The final approach compared the empirically derived spatial and temporal power-spectra to identify equivalent scales of spatial and temporal variability by identifying periods at which identical magnitudes of spatial and temporal variability were observed.

3.2.1. Representative Range of the Mean

3.2.1.1. Correlation Coefficient Models

The most intuitive methods used to quantify representative range are lagged autocorrelation functions (*i.e.* correlograms) and semi-variograms (Jacobs 1988), which describe the positive or negative relationship among measurements in a series through time or space

(Legendre 1993, Mønness & Coleman 2011). Lagged Pearson's product-moment correlation coefficients ($\dot{\hat{\rho}}$) define the correlation between all measurements at a given lag (*h)*, which can be simplified as the covariance ($\widehat{C}$) of measurements at lag *h* standardized by the variance ($\widehat{\sigma}^2$):

$$\dot{\hat{\rho}}(h) = \frac{\widehat{C}(h)}{\widehat{\sigma}^2} \qquad [1]$$

where covariance is a quantity used to measure similarity. The lagged autocorrelation can be interpreted as the degree to which measurement *A* resembles measurement *B* relative to the variance in the system as a whole, which can be modeled using an exponential model:

$$\dot{\hat{\rho}}(h) = \dot{\hat{\rho}}(0)e^{-\alpha d} \qquad [2]$$

where $\dot{\hat{\rho}}(0)$ is the autocorrelation at lag 0, *d* is the number of lags, and α is the inverse scale height, the range at which the autocorrelation decays by a value of *e* (Kagan 1972). In theory, $\dot{\hat{\rho}}(0)$ should always be one, indicating a perfect autocorrelation at lag-0. In practice, these lags often deviate from one due to variability operating below the sampling grain that cannot be resolved. Lagged correlation coefficients are used to estimate biological patch sizes (Legendre 1993), and to determine analysis resolutions that do not violate statistical assumptions of independence (Schneider 1990). The squared correlation coefficient is mathematically identical to the coefficient of determination (R^2), which quantifies the proportion of variability described from spatial correlation.

In contrast, semi-variograms (γ) measure the dissimilarity at each lag (*h*) as half the average squared difference of all measurements (z) at each lag:

$$\gamma(h) = \frac{1}{2N(h)}\sum_{i=1}^{N(h)}[z(x_i + h) - z(x_i)]^2 \qquad \textbf{[3]}$$

Dissimilarity typically increases with distance, until semi-variance asymptotically approaches half the variance of the series. Semi-variograms are usually described by three parameters, the range, sill, and nugget (Gringarten & Deutsch 2001). The range parameter is the lag at which the semi-variance approaches half the variance, or the sill. Beyond this range, measurements

become statistically independent and the variance will no longer increase with distance. In theory, there should be no dissimilarity (semi-variance) at a range of zero, as measurements should be perfectly autocorrelated. In practice, there is often semi-variance below the grain size, quantified by the nugget. Covariance and semi-variance are quantities that measure similarity and dissimilarity, which sum to the variance (Gringarten & Deutsch 2001).

$$\widehat{\boldsymbol{C}}(\boldsymbol{h}) + \mathbf{2}\boldsymbol{\gamma}(\boldsymbol{h}) = \widehat{\boldsymbol{\sigma}}^{\mathbf{2}} \qquad [\mathbf{4}]$$

The lagged correlation coefficient inversely mirrors the semi-variance, and is the complement to the semi-variance standardized by the variance (Mønness & Coleman 2011):

$$\dot{\widehat{\boldsymbol{\rho}}}(\boldsymbol{h}) \,\mathbf{x}\, \widehat{\boldsymbol{\sigma}}^{\mathbf{2}} = \widehat{\boldsymbol{\sigma}}^{\mathbf{2}} - \mathbf{2}\boldsymbol{\gamma}(\boldsymbol{h}) \qquad [\mathbf{5}]$$

$$\dot{\widehat{\boldsymbol{\rho}}}(\boldsymbol{h}) = \mathbf{1} - \frac{\mathbf{2}\boldsymbol{\gamma}(\boldsymbol{h})}{\widehat{\boldsymbol{\sigma}}^{\mathbf{2}}} \qquad [\mathbf{6}]$$

In Equation [6], the lagged correlation coefficients approach zero at the same range as the semi-variance approaches the sill, and $\dot{\widehat{\boldsymbol{\rho}}}(\mathbf{0})$ is the compliment of twice the semi-variogram nugget standardized by the variance. Spherical semi-variogram models are analogous to the exponential decay model of spatial autocorrelation. Selection of correlograms or semi-variograms is largely a matter of preference and precedent within a discipline when analyzing one-dimensional data (Mønness & Coleman 2011). Semi-variograms are slightly more robust to departures from stationarity than lagged autocorrelation functions and can describe two-dimensional, irregularly spaced measurements. Semi-variogram analysis and interpretation has been hampered by ambiguity in terminology (Bachmaier & Backes 2008) and statistical testing in the absence of permutations (*c.f.* Walker et al. 1997). Autocorrelation functions, mathematically identical to lagged correlation coefficients, remain more intuitive to a broad audience. For this reason, modeled variograms parameters have previously been used to fit correlation coefficient models to parsimoniously and intuitively describe the decay of representativeness with range (Anttila et al. 2008).

Assuming a random data series, lagged-correlation coefficients are distributed around zero with a variance of 1/*n*, with *n* bins the length of the data series. Assuming a random distribution, the 95% confidence interval of lagged correlation coefficients is 2/√*l*, where *l* is the number of lags in the series. Substituting 2/√*l* for $\hat{\rho}(h)$ in Equation [2], and then solving for the representative range (r_{rep}) as the range given by the number lags (*d)* of grain size *g*:

$$r_{rep} = -g\left(\frac{ln\left(\frac{\left(\frac{2}{\sqrt{l}}\right)^2}{\hat{\rho}(0)}\right)}{\alpha}\right) \qquad [7]$$

A coefficient of determination model was applied to describe how similarity in fish density decayed with distance in Admiralty Inlet. Lagged Pearson's correlation coefficients were calculated within each transect (n=547), then squared to create lagged coefficients of determination (R^2). An exponential decay model was fit to the lagged correlation coefficients and coefficients of determination across all transects using a least squares algorithm. Once the range was calculated, the area of a circle defined by the representative radius was calculated. These areas were scaled to a square kilometer to make inferences about the number of required packages within each square kilometer of the sampling domain.

3.2.1.2. Random Sampling Sample Size Calculations

Gray et al. (1992) created a framework to optimize spatial sampling effort and allocation when analyzing the effects of marine pollution on benthos. The focus of the sampling effort was the number of stations *n* needed to detect a difference in community abundance at lag *t.* The sampling effort was given by:

$$n = \frac{s^2}{RPE^2\bar{x}^2} \qquad [8]$$

where *s* and $\bar{x}$ are the standard deviation and mean taken from a pilot study, and *RPE* is the minimum effect size as a proportion of the mean. Equation [8] appears to be a derivative of the sample size calculation for detecting the mean difference in paired means (Sullivan 2006), where measurements are paired through time:

$$\boldsymbol{n_{pairs} = \left(\frac{Z_{1-\alpha/2} * \sigma_d}{E}\right)^2} \qquad [9]$$

The critical value, $Z_{1-\alpha/2}$, for a 0.95 significance level (α= 0.05) is 1.96. The σ_d is the standard deviation of the paired differences between times at each station. The variance of differences between normal distributions is the sum of both variances. Assuming variance remains constant through time, σ_d can be expressed as:

$$\boldsymbol{\sigma_d = \sqrt{2 * \sigma_t^2}} \qquad [10]$$

where σ_t^2 is the spatial variance at time *t*. If Equation [8] is a derivative of Equation [9], Equation [8] underestimates the required sample size by a factor of $(Z_{1-\alpha/2})^2$, (3.84 assuming α= 0.05) by not including the squared Z test statistic in the numerator and by another factor of two for not accounting for the increased variance of the normal difference distribution. *E* in Equation [9] is the absolute effect size, which when standardized by the mean, $\bar{x}$, produces the *RPE* from [8]:

$$\boldsymbol{RPE = \frac{E}{\bar{x}}} \qquad [11]$$

Given a known sampling domain *S* over which σ_t was measured, and assuming a relatively even distribution of sensors, the representative area can be can be calculated as:

$$\boldsymbol{a_{rep} = \frac{S}{n_{pairs}}} \qquad [12]$$

Combining Equations [9] and [12] by substituting Equation [9] for n_{pairs} in Equation [12]:

$$\boldsymbol{a_{rep} = \frac{S}{\left(\frac{Z_{1-\alpha/2} * \sigma_d}{RPE * \bar{x}}\right)^2}} \qquad [13]$$

The range *r* to represent an area *a* is defined by the area of circle:

$$\boldsymbol{a_{rep} = \pi r_{rep}^2} \qquad [14]$$

which can be combined with Equation [13]:

$$\boldsymbol{r_{rep} = \sqrt{\frac{S}{\pi * \left(\frac{Z_{1-\alpha/2} * 2\sigma_t}{RPE * \bar{x}}\right)^2}}} \qquad [15]$$

Equation [15] is used to avoid Type I errors associated with a false positive test. In monitoring networks, failures to recognize Type II errors are more egregious than a false positive (Underwood 1997, Underwood & Chapman 2003), as Type II errors are unidentified biological impacts that cannot be mitigated. Power analysis calculations can be used to identify the sample size required to identify effects with adequate statistical power (Zar 2010). The required number of pairs in a paired *t*-test power analysis is expressed as:

$$\boldsymbol{n_{pairs} = \frac{\sigma_d^2 \left(Z_{1-\alpha/2} + Z_\beta\right)^2}{E_d^2}} \qquad [\mathbf{16}]$$

where σ_d^2 can be calculated following Equation [10]. Both $Z_{1-\alpha/2}$ and Z_β represent critical Z-statistics corresponding to subjectively chosen alpha and beta values, which are commonly set at 1.96 (α = 0.05) and 0.84 (β = 0.80). E_d is analogous to the effect size introduced in Equation [9]. The representative range can then be calculated by substituting n_{pairs} into Equations [12-14].

This method calculates the required sample size for measurements paired through time, and analyzed using a paired t-test, where the number of pairs is the number of spatially distributed sensors. Measurements are only compared at two distinct times, pre- and post-installation. T-tests assume normal distribution of paired differences, which is satisfied if both paired sets are normally distributed by the normality of normal difference distribution (Zar 2010). T-test sample size calculations do not consider the structure or gradients contributing to the spatial variability, but treat spatial variability as the variance of a normal distribution to be sampled. A *t*-test sample size calculation assumes random sampling, which treats all spatially distinct stations as random samples of the mean. The sampled population may be non-randomly distributed through space, but the spatial structure is assumed to be identical at both sampling times. Unlike autocorrelation analysis which describes the range to which inferences can made, the sample size calculation calculates the number of stations required to make statements about the domain if spatial variability is treated as random variance. Statistical power to identify change through time is compromised by randomly sampling and ignoring spatial structure. Sample size calculations require estimates of spatial variability, which must be acquired from some form of

mobile survey. The more baseline mobile data that are collected, the more certain estimates of the spatial variance become.

In the case study, estimates of r_{rep} were calculated independently using Gray's sample size, *t*-test sample size, and power analysis formulas. To remove the spatial autocorrelation from the series due to non-random fish distributions (Bence 1995), sample size calculations were conducted at statistically independent grain sizes over the extent of an entire grid (*n* = 57). Sequentially sampled line-transects were used to minimize the confounding of spatial and temporal variance. The minimum effect size, *E,* was subjectively established as 1dB, which equates to a 25.9% change in fish density. A one dB re 1µPa at 1m change compared to the grand mean of -77dB effect size of 1dB translates to a *RPE* of 0.0129 ($\frac{\pm 1\ dB}{-77\ dB}$). Alpha was constant, 0.05, and beta in the power analysis was conservatively set to 0.90.

3.1.1.3. Relative Standard Interpolation Error

Rather than estimating the range to which a measurement can be interpolated through space, it is often beneficial to model departures from the interpolated estimate. These departures, called interpolation errors, increase with distance from a point and thus increase as the density of sensors within a domain is decreased. Sensor density can be optimized by the predetermined magnitude of allowed interpolation error in the linear (Gandin 1970) or areal interpolation (Kagan 1966). A more detailed derivation can be found in Milewska & Hogg (2001). The relative standard interpolation error (*RSIE*) is significantly different in the calculation and interpretation from the *RPE* presented above. *RSIE* is the error introduced by interpolating point measurements to distant points or areas. When linearly interpolating between two points, the *RSIE* is maximized at the midpoint of the vector defined by those points. *RSIE* of linear interpolation (Gandin 1970) can be calculated as:

$$\boldsymbol{RSIE_{interpolation.point}} = \sqrt{\mathbf{1} - \frac{\mathbf{2\rho^2(\frac{d}{2})}}{\mathbf{1} + \boldsymbol{\eta} + \boldsymbol{\rho(d)}}} \qquad [\mathbf{17}]$$

where $\boldsymbol{\rho(d)}$ is the modeled exponential decay function from Equation [2], and η is defined as:

$$\boldsymbol{\eta = 1 - \rho(0)} \qquad [\mathbf{18}]$$

Using a predetermined acceptable *RSIE*, Equation [17] can be solved to give the maximum interpolation distance *d*.

The objective of spatially distributed networks is often to estimate the mean of a quantity within a domain as opposed to the value at a given point in space. Areal interpolation of a point measurement produces a different interpolation error. Assuming the representative area is a circle, the representative range will be the radius of a representative circle. The areal interpolation error (Kagan 1966) is quantified as:

$$\boldsymbol{RSIE_{interpolation.area}} = \sqrt{\boldsymbol{\sigma_\varepsilon^2 + 0.23\sigma_p^2 \frac{\sqrt{S}}{D_0}}} \qquad [\mathbf{19}]$$

where $\boldsymbol{\sigma_p^2}$ is the temporal variance at the point sensor, *S* is the area over which the point source is interpolated, $\boldsymbol{D_0}$ is the inverse of *a* in Equation [2], and σ_ε^2 is defined as:

$$\boldsymbol{\sigma_\varepsilon^2 = \eta\sigma_p^2} \qquad [\mathbf{20}]$$

Given a predetermined $RSIE_{interpolation.area}$ in Equations [17], the equation can be solved for the area *S*, which is the area of the circle defined by radius r_{rep}:

$$\boldsymbol{S = \left(\frac{D_0(RSIE^2 - \sigma_\varepsilon^2)}{0.23 * \sigma_p^2}\right)^2} \qquad [\mathbf{21}]$$

Then solved for the r_{rep} as a function of *S,* similar to Equations [12-15]:

$$\boldsymbol{r_{rep} = \sqrt{\frac{\left(\frac{D_0(RSIE^2 - \sigma_\varepsilon^2)}{0.23 * \sigma_p^2}\right)^2}{\pi}}} \qquad [\mathbf{22}]$$

Relative standard interpolation error (*RSIE*) analysis is based on the modeled exponential decay in spatial autocorrelation. Even if *RSIE* isn't used to determine the representative range of biological networks, it can be used to estimate interpolation errors. In the absence of a meaningful *RSIE* threshold, *RSIE* curves were calculated to describe the error introduced at the four representative ranges identified by correlation coefficient models, Gray's sample size calculation, *t*-test sample size calculations, and power analysis. *RSIE* analysis can be conducted on any data that has been used to estimate autocorrelation. The only additional requirement is the temporal variance when interpolating a point measurement to the surrounding area (see Equation [19]). Except for Equation [19], every parameter is derived from the spatial

autocorrelation, derived from the mobile acoustic survey. In this case, temporal variance, in Equation [19], was calculated from the stationary acoustic survey (*i.e.* echosounder), but could also be calculated using repeated mobile data.

3.2.2. Representative Range of Variance Measurements

3.2.2.1. Theoretical Spectra

Temporal variability, like the mean, varies through space (Damian et al. 2003). The spatial heterogeneity of temporal variance is visualized by Hovmöller diagrams (Hovmöller 1949), which illustrate variability across space and time. Temporal variability is structured in space (*e.g.* Fig. 10c in Torrence & Compo 1998, Certain et al. 2007, Hocke & Kampfer 2011), such that loci demonstrating high temporal variability are spatially aggregated. Point measurements used to estimate the temporal variance of a quantity also have a representative range. To transition from the representative range of a mean to the variance of a quantity, the analytical approach shifts from the time or distance domain to the frequency domain.

The first technique to estimate the representative range of temporal variance is a combination of autocorrelation and spectral power. Due to autocorrelation in a series, the power spectra of a red-noise, first order auto-regressive process is minimized at small periods and increases logistically with period (Gilman et al. 1962):

$$\boldsymbol{L_f = \frac{1 - \rho^2(1)}{1 + \rho^2(1) - 2\rho(1) * \cos\left(\frac{2\pi * k}{l}\right)}} \qquad [23]$$

where L_f is the ratio of the predicted variance relative to the variance of a random, white-noise process and multiplying L_f by the white noise variance produces an estimate of the true predicted variance. $\rho(1)$ is calculated by substituting 1 for *d* in Equation [2]. The factor of two within the cosine argument was not included in Gilman et al.'s (1962) original derivation, but included in subsequent applications (*e.g.* Torrence & Compo 1998) so that L_f approaches the maximum variance at frequencies approaching zero. In Equation [23], *l* is the maximum lag distance, and k/l is the frequency as a function of the maximum lag distance *l*, which is equivalent to the inverse of the period:

$$\boldsymbol{frequeny = \frac{k}{l}} \qquad [24]$$

$$\boldsymbol{period = \frac{1}{frequency}} \qquad [25]$$

The autocorrelation at lag 1, $\rho(1)$, was first modeled in Equation [2]. Note that at frequencies approaching zero (*i.e.* maximum period), the cosine term approaches zero and the maximum predicted variance in a red-noise spectrum simplifies to:

$$\boldsymbol{L_{f.max} = \frac{1 - \rho^2(1)}{1 + \rho^2(1) - 2\rho(1)}} \qquad [26]$$

The normalized variance increases logistically over observation scales as a function of the first order correlation coefficient. The scale to which the variance can be considered representative is the scale at which a suitably high proportion *b* of the maximum variance, expressed in Equation [26], is expected to be observed. Equation [23] can be set equal to the proportion *p* of the maximum predicted variance in Equation [26] and then solved for the frequency. The inverse of the frequency is the period at which measurements of the variance are considered representative, and can be calculated from Equation [25]. The frequency from Equation [23] at which we expect to see *p* described in Equation [25] is the scale at which measurements of variance are considered representative. This relationship can be quantified by combining Equations [23] and [26]:

$$\overbrace{\boldsymbol{p * \left(\frac{1 - \rho^2(1)}{1 + \rho^2(1) - 2\rho(1)}\right)}}^{\textbf{Equation [26]}} = \overbrace{\boldsymbol{\frac{1 - \rho^2(1)}{1 + \rho^2(1) - 2\rho(1) * \cos\left(\frac{2\pi * k}{l}\right)}}}^{\textbf{Equation [23]}} \qquad [27]$$

Which is further simplified to:

$$\boldsymbol{period_{rep} = \frac{l}{k} = g * \left(\frac{2\pi}{\operatorname{acos}\left(\frac{\left(\frac{1 + \rho^2(1) - 2\rho(1)}{p}\right) - 1 - \rho^2(1)}{-2\rho(1)} \right)} \right)} \qquad [28]$$

Modeled power spectra assume that the scale at which the variance approaches the maxima is the scale at which the variance can be considered representative. The only spatial parameter included in the model is the first order autocorrelation, assuming a red-noise random walk model.

In the example, power spectra were modeled using the best-fit autocorrelation model previously described. This model assumes fish densities are distributed around a uniform field with first order autocorrelation. This assumption is more easily explained in a one-dimensional time series, where the value at interval *n* is only dependent on the previous value and a variance *Y,* without any trends, covariates, or natural cycles in the data.

$$\boldsymbol{X_n = \rho(1) X_{n-1} + Y_n, \text{ for all } n \text{ lagged by distance } t} \qquad [29]$$

Red-noise spectra were modeled using the lagged correlation coefficients fit to an exponential decay model. The proportion of the maximum variance deemed representative, *p*, was subjectively set at 95%. The scale at which the predicted variance reached 95% of the maximum variance was calculated from Equation [28]. The maximum period described in spectral analysis is usually limited by the Nyquist frequency to half the extent of the series (Denman 1975), but the theoretical spectra was empirically derived from the first order autocorrelation, assuming a random walk over large periods, and can be modeled over longer periods than the Fourier power spectra. The result is that the modeled spectra can be extrapolated beyond the constraints of the Nyquist frequency.

3.2.2.2. Equivalent scales of space and time

Biological communities vary through a spectrum of spatial and temporal periods. Linkages between the spatial and temporal periods at which biological and physical systems vary are well established (NASA 1988, Steele et al. 1994, Wu 1999). In general, quantities varying over large spatial periods will also vary over large temporal periods. Although the relationship between periods of spatial and temporal variability is highly variable (*c.f.* Steele et al. 1994, NASA 1988, Wu 1999), the linkage between spatial and temporal period suggests that an equivalent spatial period exists for every temporal period. To maintain predictive power, spatio-temporal modeling of processes or communities must be conducted at equivalent spatial and temporal periods (Wiens 1989, Wu 1999).

The observed variance of a quantity is dependent on the grain or period at which a quantity is measured (Wiens 1989). Spatial and temporal variability must be treated as equivalent when scaling between mobile and stationary measurements of a quantity. Assuming

spatial and temporal variability can be directly compared, the spatial and temporal periods at which equal magnitudes of variance are observed are equivalent. Point source measurements of temporal variance, collected over a known temporal extent and period, can be considered spatially representative at the equivalent spatial period. Measurements of temporal variance collected from a point sensor can then be considered representative of spatial variability at the equivalent spatial period.

The period-dependent variance has historically been quantified using spectral power. In general, spectral power (*i.e.* variance) increases with period following a power-law. Assuming linearity in the spatial and temporal power-law spectra, the variance at the largest resolvable temporal period, limited by the Nyquist frequency (Platt & Denman 1975), can be compared to the spatial spectra to identify the corresponding spatial period at which equivalent amounts of variability are expected to be observed.

Averaging the localized wavelet spectra across all instances yields the global wavelet spectra, mathematically analogous to the Fourier power spectra (Hudgins et al. 1993, Percival 1995, Perrier et al. 1995). Like the Fourier power spectra, the global wavelet spectrum assumes the series is stationary, limiting the spatial and temporal analysis to relatively short extents. The advantage of using wavelet analysis over traditional spectral density is that wavelet analysis allows the visualization of non-stationary dynamics before integrating through time or space to identify transient spatial or temporal scales of variance. Continuous wavelet transforms, which analyze periods at redundantly small intervals, were used to increase period resolution (Torrence & Compo 1998), and averaged through time using:

$$\boldsymbol{w(T)} = \frac{\overline{\boldsymbol{W}}^{\boldsymbol{2}}\boldsymbol{(T)}}{\boldsymbol{\delta^2}} = \frac{\boldsymbol{1}}{\boldsymbol{N}} \sum_{\boldsymbol{n=0}}^{\boldsymbol{N-1}} |\, \boldsymbol{W_n(T)}|^{\boldsymbol{2}} \qquad [\boldsymbol{30}]$$

where $\overline{W}^2$ is the mean wavelet power, T is the bandwidth over which wavelet powers are averaged over n times to N length. The analyzed spatial and temporal scales increased with 12 steps per octave, a common period resolution in ecological contexts (Urmy et al. 2012), from twice the resolution of the series to the Nyquist frequency as:

$$\underset{\boldsymbol{2g \rightarrow Nyquist}}{\boldsymbol{T}} = \boldsymbol{g} * \boldsymbol{2}^{\boldsymbol{(i+11)/12}} \qquad [\boldsymbol{31}]$$

where *g* is the spatial or temporal grain of the measurement, and the maximum scale is limited by ½ the extent of the series (i.e. Nyquist frequency; Platt & Denman 1975). Wavelets were decomposed using a Morlet wavelet of frequency 6, with a known dilation of 1.03 to translate the wavelet scale to the equivalent Fourier power spectra period (Torrence & Compo 1998). Peaks in the global wavelet spectrum artificially inflate the power of peaks observed at large periods relative to small periods compared to the true Fourier power spectra (Liu et al. 2007). This potential bias was not corrected here because the bias is a uniform factor of the wavelet scale in both the spatial and temporal series (Liu et al. 2007). The uncorrected global wavelet spectrum approaches the Fourier spectral power as both are smoothed with increasingly large bandwidth, suggesting that the global wavelet spectrum best-fit line will be less biased than any individual peak intensity.

Finding equivalent scales of spatial and temporal variability require high scope measurements covering the spatial extent of the domain or at twice the extent of the proposed interpolation range. Linearity in both the spatial and temporal spectrum must be empirically verified across all spatial and temporal periods of interest as the best-fit spectrum can deviate from linearity due to localized variance or the presence of patches (Platt & Denman 1975). Periods cannot be analyzed larger than the inverse of the Nyquist frequency, one half of the total extent (Platt & Denman 1975). Therefore interpolation distance will always be limited to at least half the survey extent.

Wavelet analysis was used to quantify the localized period dependent variance spectra within a series (Torrence & Compo 1998). The global wavelet spectrum was calculated for all 547 spatial transects and 360, 12-minute stationary sampling periods. The mean global wavelet power was calculated at each spatial and temporal period. Global wavelet power was calculated as a function of period instead of frequency to standardize irregularities in line-transect length. Both wavelet power and scale were log normalized, and a best fit line was regressed using linear least squares for both mobile and stationary data:

$$\boldsymbol{Spatial\ Power\ Spectrum}\text{: } \mathbf{log_{10}}\left(\frac{\overline{W_s^2}(T_s)}{\delta_s^2}\right) = m_s * \mathbf{log_{10}}(T_s) + b_s \qquad [32]$$

$$\textbf{\textit{Temporal Power Spectrum}}: \mathbf{log_{10}}(\frac{\overline{\boldsymbol{W}}_{\boldsymbol{t}}^{\mathbf{2}}(\boldsymbol{T_t})}{\boldsymbol{\delta}_{\boldsymbol{t}}^{\mathbf{2}}}) = \boldsymbol{m_t} * \mathbf{log_{10}}(\boldsymbol{T_t}) + \boldsymbol{b_t} \qquad [\mathbf{33}]$$

where *m* and *b* are the slope and intercept of the best-fit lines. The maximum temporal power spectrum can be defined as the power spectrum at the Nyquist frequency, or a period of ½ the temporal series length N:

$$\mathbf{max}\big(\boldsymbol{w_t}(\boldsymbol{T})\big) = \boldsymbol{m_t} * \mathbf{log_{10}}(\boldsymbol{T}_{\frac{\mathbf{1}}{\mathbf{2}}\boldsymbol{N(t)}}) + \boldsymbol{b_t} \qquad [\mathbf{34}]$$

This equation can be substituted into Equation [32] to find the spatial scale at which spatial variance matches that observed at the largest temporal scale:

$$\mathbf{max}\big(\boldsymbol{w_t}(\boldsymbol{T})\big) = \boldsymbol{m_s} * \mathbf{log_{10}}(\boldsymbol{T_s}) + \boldsymbol{b_s} \qquad [\mathbf{35}]$$

and then solved for T_s to yield the representative spatial scale of the variance $T_{s.rep}$:

$$\boldsymbol{T_{s.rep}} = \mathbf{10}^{\left(\frac{(\mathbf{max}(\boldsymbol{w_t}(\boldsymbol{T}))-\boldsymbol{b_s})}{\boldsymbol{m_s}}\right)} \qquad [\mathbf{36}]$$

This is the scale at which an equivalent amount of spatial variability is observed at the maximum temporal scale. The spatial and temporal sampling grain should approach equivalence to facilitate unbiased comparisons. Here, fine spatial (20m) and temporal (1.2 seconds) grains were used, which each incorporated six acoustic pings. The suitability of spatial and temporal grain size can be checked by the difference in the *y*-intercept of each log-normalized modeled spectrum after the fact, if not then caution should be used in scaling between spatial and temporal variance.

3.2.3. Interrelationship and Independence of proposed methods

All of these methods are linked, but provide independent estimates of the representative range based on unique assumptions and interpretations. Lagged coefficients of determination are equivalent to the square of the lagged correlation coefficients, produced by the autocorrelation function. The autocorrelation function is the autocovariance standardized to the variance of the series. A cosine transformation of the autocovariance yields the red-noise modeled Fourier spectra (Denman 1975). The global wavelet spectrum is the empirically derived version of the modeled power-spectrum based on the first order autocorrelation. The modeled power spectrum forms the backbone of significance tests of peaks in the global wavelet

spectrum. All of these methods are linked, but provide independent estimates of the representative range based on unique assumptions and interpretations.

3.2.4. Case Study: Fish Densities in Admiralty Inlet, WA

Two six-meter diameter tidal turbines will be installed into Admiralty Inlet, Puget Sound, WA in the summer of 2016 as part of a tidal MHK energy pilot project. Puget Sound is a complex, tidally dominated estuarine system in Washington state, covering more than 1,988 km^2 (NOAA 1987). Admiralty Inlet is a shallow sill forming the major entrance to Puget Sound (Figure 3.1) with average tidal flux in excess of 1.5 x 10^4 cubic meters of water per second (Babson et al. 2006) at speeds in excess of 3.5 ms^{-1} (Gooch et al. 2009). The pilot tidal energy site has been proposed ~750m from Admiralty Head in 55m of water (FERC 2014). Tidal energy is a relatively new suite of technologies with unknown effects on local fish communities. Due to this uncertainty, the Federal Energy Regulatory Commission (FERC) requires approval of site-specific monitoring plans before issuing development permits. To date, requirements of all environmental monitoring plans lack specific guidelines and are not standardized across sites (*c.f.* Copping et al. 2014). Active acoustics are a common tool for measuring fish and macrozooplankton densities in marine environments, and are commonly deployed at MHK sites (*e.g.* NYSERDA 2011). In its infancy, MHK installations are capital limited, making the cost effectiveness of biological monitoring critical to the success of the industry. Repeated active acoustic mobile surveys for long-term (>5 years) biological monitoring are cost prohibitive. Stationary sensor networks are assumed to be more cost effective than repeated mobile surveys. A network of static active acoustic sensors has been proposed to monitor the effects of tidal energy converters on fish density, but the number of sensors and their placement is uncertain. Historically, regulators have erred on the side of precaution when facing uncertainty in designing monitoring programs (Underwood 1997, Underwood & Chapman 2003), sometimes deploying numbers of sensors and sampling effort that would be cost prohibitive in a long (> 5 year) monitoring program (*e.g.* NYSERDA 2011).

In a baseline demonstration project, spatiotemporal fish density distributions were measured from concurrent mobile and stationary acoustic surveys. Measurements of spatial and

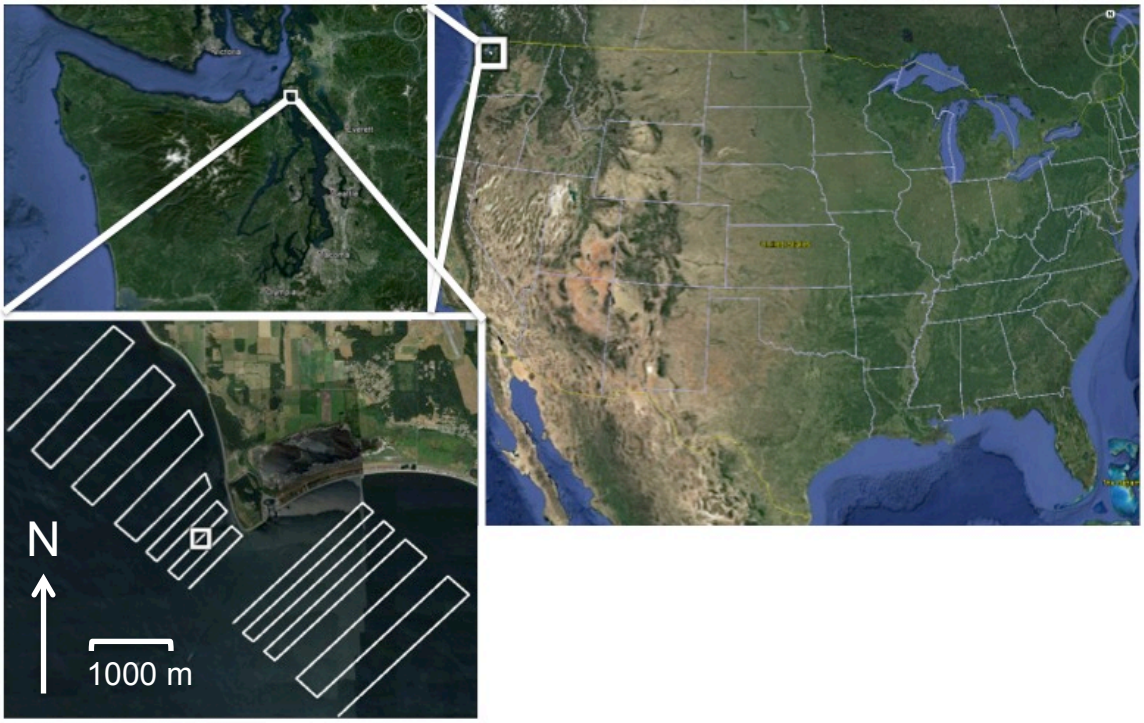

Figure 3.1. Admiralty Inlet, Puget Sound, USA. (top left) Admiralty Inlet at the mouth of Puget Sound. (bottom left) the location of the stationary echosounder, at a proposed tidal energy pilot site, is denoted by the white square in relation to the two spatial grids north and south of the stationary package, each consisting of high and low resolution transects.

temporal mean and variability of fish density were used to estimate the representative range using the previously described six approaches. Fish densities were quantified using mean volume backscattering strength (S_v; units: dB re 1 μpa), a log-normalized acoustic metric of density (MacLennan et al. 2002). The second approach calculates the number of sensors needed to monitor a site, while the remaining three approaches calculate the spacing between sensors. The number of sensors can be converted to the representative range to create a common metric used to compare estimates from each method. The area of the domain divided by number of sensors is the average representative area of each sensor. If the representative area of each sensor is a circle, then the radius of a circle of the average representative area is the representative range.

3.2.4.1. Mobile Acoustic Survey

Two mobile acoustic surveys were conducted from May 2nd to May 13th and June 3rd to June 14th, 2011. Each survey repeatedly sampled two grids of transects, one at and one south of the proposed pilot site, during day and night. A total of 57 sampling grids were completed over both surveys encompassing all tidal states, with a total of 547 transects. Transects were oriented perpendicular to the shore and the flow of the predominant tidal current (Figure 3.1), surveyed at approximately 3.6 m/s (7 knots). The grids covered an area of 16.1 km^2 with transects spaced ¼ km apart near the proposed pilot site switching to lower resolution transects spaced ½ km apart. Analysis was constrained to within 25m of the bottom, approximately twice the vertical footprint of the proposed turbines.

Mobile acoustic data were collected at 1 Hz using a 120 kHz transducer with a 7° beam width (between half power points) traveling at 7 knots, transmitting at 500 Watts and a 512 ms pulse duration. Surface turbulence due to tidal currents was a major feature in the acoustic data record and was identified using the schools detection algorithm in Echoview (v5.4.91 Myriax Inc.) acoustic data processing software. School detection parameter settings were: minimum total school length = 5m, minimum total school height = 3m, minimum candidate length = 5m, minimum candidate height = 3m, maximum vertical linking distance = 10m, and maximum horizontal linking distance = 10m. Identified schools that intersected the 3m depth surface

exclusion range were excluded as turbulence. Noise was removed from data using a -75 dB threshold, which corresponded to a 16 dB signal to noise ratio. The threshold was set to assist the turbulence removal algorithm and to exclude microzooplankton from the analysis. The echosounder was calibrated prior to surveys using a tungsten carbide sphere following the protocols outlined in Foote et al. (1987).

3.2.4.2. Stationary Acoustic Survey

An autonomous, bottom-deployed, upward facing 120 kHz splitbeam echosounder sampled at 5 Hz for 12 minutes on a 2 hour duty cycle from May 10th to June 9th, 2011, collecting 357 twelve-minute samples (Figure 3.2). Similar to the mobile survey, the transducer had a 7° beam angle (between half power points) and transmitted at 1000 Watts. The stationary echosounder was deployed at the location of the proposed pilot energy site, located in the high-resolution portion of the north spatial survey grid in ~55m of water and ~750m from Admiralty Head. Noise was removed using a -75 dB threshold, identical to the spatial survey, and data was constrained to 25m from the bottom.

3.2.4.3. Grain, Extent, and Scope

Distance decay, and hence representative range, is dependent on the spatial or temporal grain (*i.e.* analysis resolution) and extent of measurements (*i.e.* range; Ciach & Krajewski 2006, Nekola & McGill 2014). Acoustic backscatter cannot be analyzed at a grain of a single transmission as backscatter varies between individual samples, but stabilizes as pings are averaged following the central limit theorem (Simmonds & MacLennan 2005). Six pings were averaged to create analytical cells, which resulted in a 20m grain in the mobile survey and a 1.2 second grain in the stationary survey. Each mobile line-transect and stationary 12-minute sampling period was analyzed independently, creating 547 mobile and 357 stationary samples. The extent of line-transects ranged between 1,300m and 3,100m, depending on the line-transect, which yielded a scope range of 65 to 155. The extent of each stationary sampling period was 12 minutes, with a corresponding temporal scope of 600.

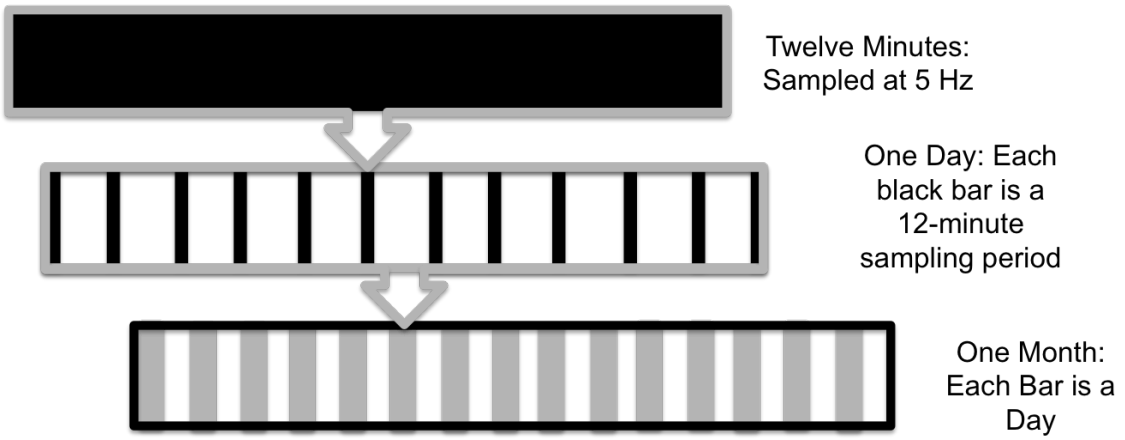

Figure 3.2. Static sensor sampling strategy. The static echosounder was deployed for 30 days (May 9th, 2011 to June 8th, 2011) and sampled fish densities at 5Hz for 12 minutes on a two hour duty cycle. Data was analyzed at a 1.2 second grain size (six pings), yielding 600 analysis cells per 12 minute sampling period.

3.3. Results

3.3.1. Representative Range of the Mean

3.3.1.1. Correlation Coefficient Model

The autocorrelation of nekton density measurements decayed rapidly as a function of distance (Figure 3.3). Exponential decay models were fit to both the lagged Pearson's correlation coefficient (Figure 3.3, top) and lagged coefficient of determination models (Figure 3.3, bottom). Following Anttila et al.'s (2008) assumption that the lagged coefficient of determination is analogous to "representativeness", the coefficient of determination decayed exponentially following ($\rho(h) = 0.3392e^{-0.168d}$). The y-intercept at lag 1 ($\rho(1) = 0.286$) demonstrated that less than a third of the variability between sequential observations was explained by autocorrelation. The median data series length of all transects was used to calculate a threshold for significance (2600 m transect sampled at a 20m resolution, yielding $l = 130$ samples), because correlation coefficients were calculated for each transect. Therefore the 95% CI for a lagged, correlation coefficient given the median transect length was 0.175. The square of the lagged correlation coefficient 95% CI yields the 95% CI for the coefficient of determination, which was 0.0307 for the fish density data. This threshold corresponds to the range at which observations became approximately independent. Based on an empirically derived threshold of $R^2 = 0.0307$, the representative range of stationary sensors measuring fish density was estimated to be 285.65 meters in Admiralty Inlet. Based on the area defined by a circle with a radius of 285.65m, 3.9 sensors per square kilometer would be needed to monitor the domain (Table 3.2).

3.3.1.2. Sample Size Calculation

The number of required sensors was calculated individually within each sampling grid (n = 57) following both Gray et al.'s (1992) formula (Equation [8]), and the derived sample size calculation in Equations [15-16]. The mean representative range using Gray et al.'s (1992) formula in each grid was 403.9 m, with a median value of 366.0 m (Figure 3.4, left). The statistically derived sample size calculation from Equation [15] yielded a representative range of 30.57 m and a median representative range of 21.7 m (Figure 3.4, middle). The power analysis holding alpha constant ($\alpha = 0.05$), and with beta set at 0.90 (Equation [16]), resulted in a mean

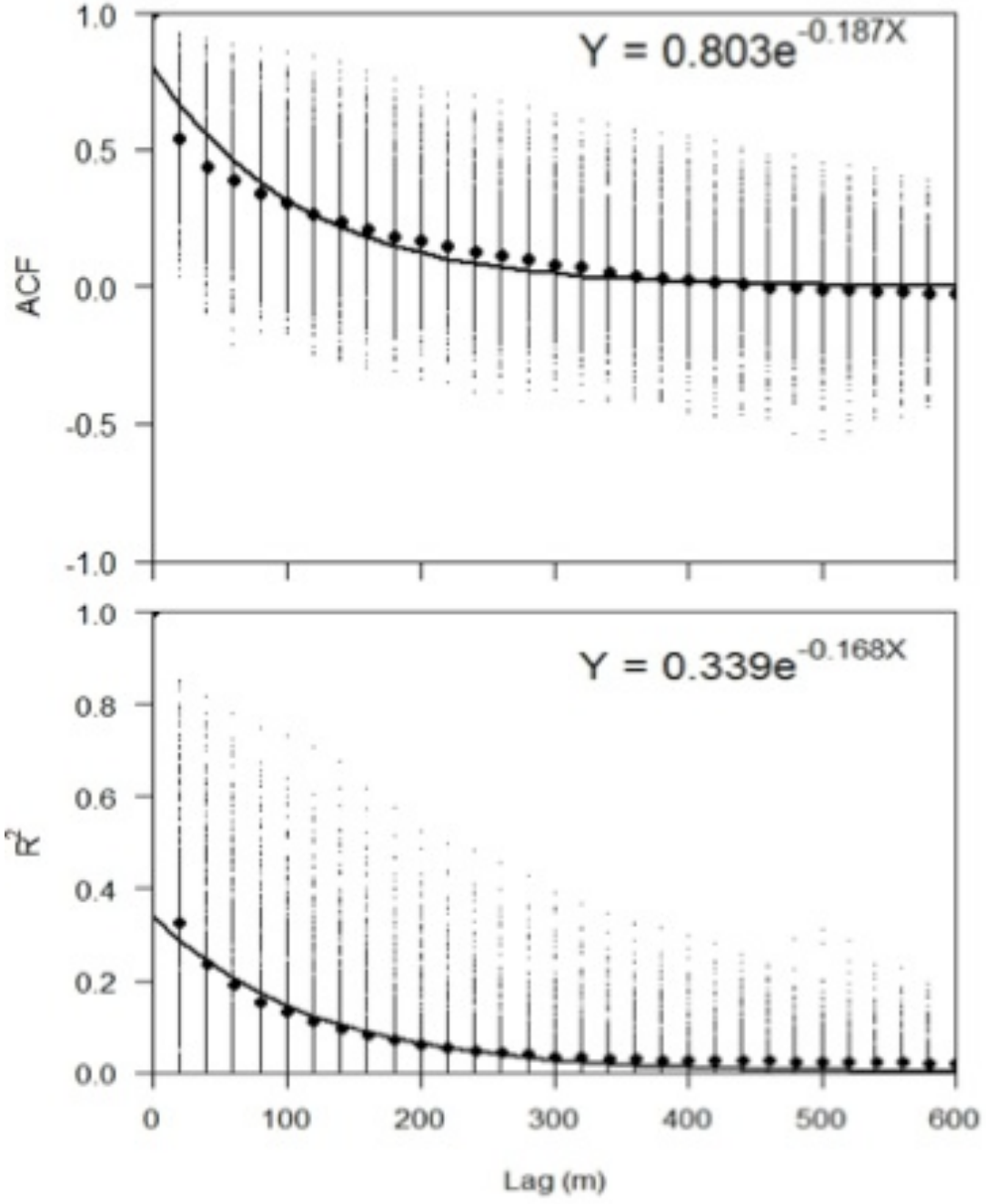

Figure 3.3. Lagged coefficient of determination model. Black points denote the mean (top) lagged correlation coefficient or (bottom) coefficient of determination across all 547 transects at each lag distance. The individual correlation values for all 547 transects are marked by the fine points.

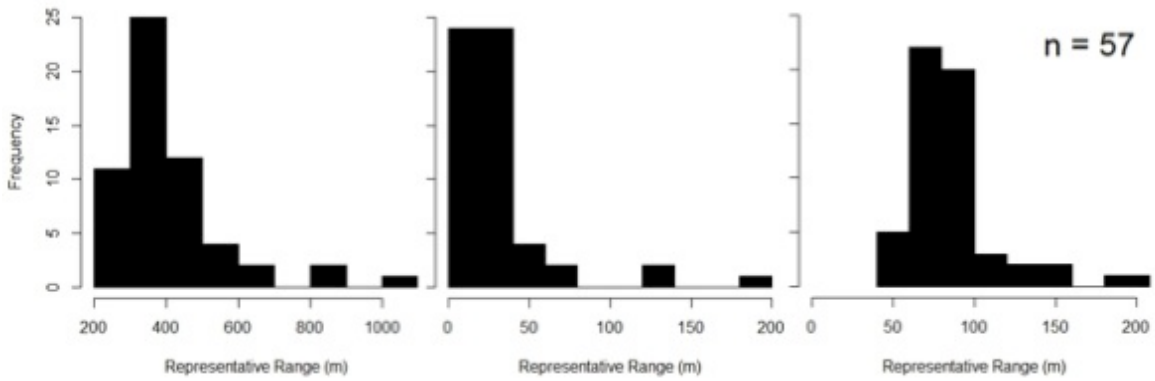

Figure 3.4. Distribution of representative ranges calculated for each sampling grid required to identify a 1 decibel change from (left) Gray et al.'s 1992 formula, (center) sample size calculation to identify mean paired differences, and (right) using a power analysis assuming alpha = 0.05 and beta = 0.90.

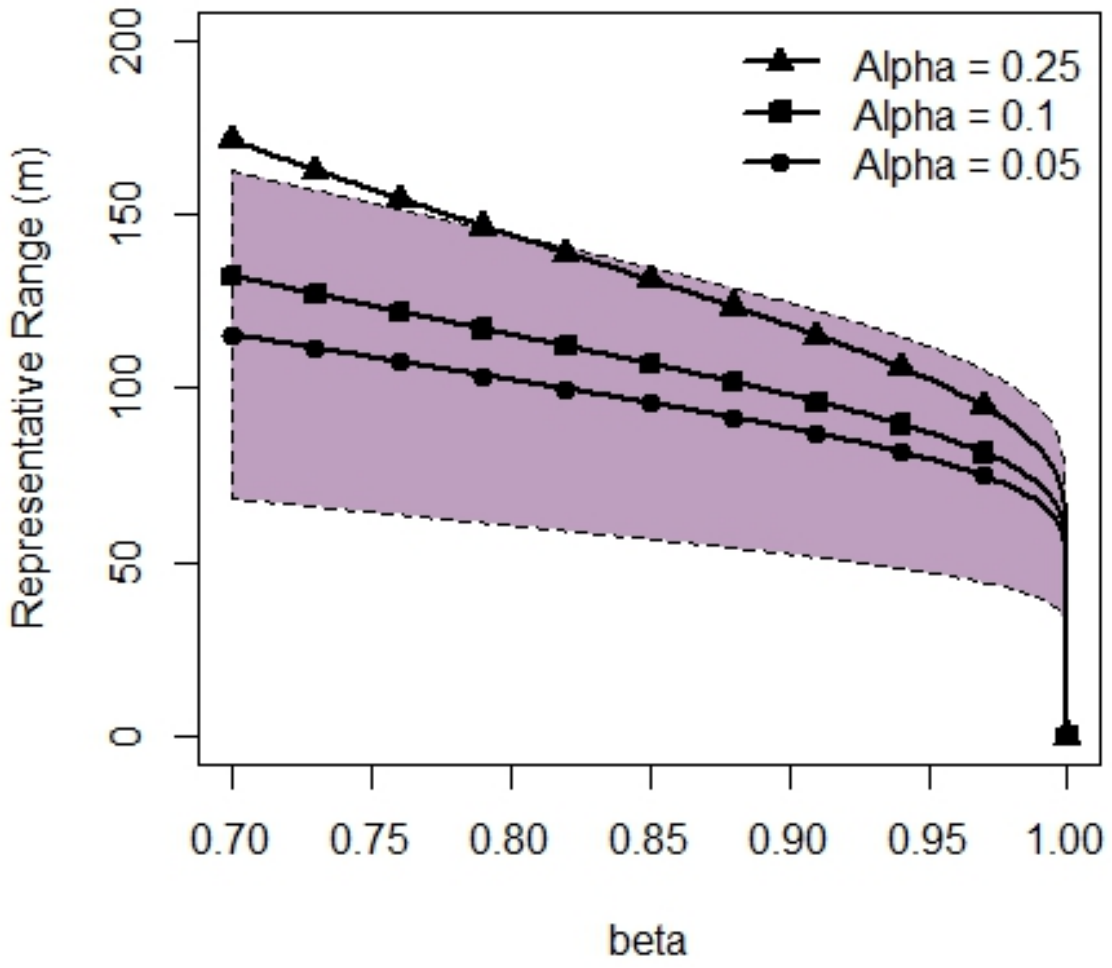

Figure 3.5. The mean representative range of each sensor calculated from paired t-test power analyses conducted on each spatial grid (n=57). The polygon envelops the mean range at alpha = 0.05 +/- one standard deviation.

representative range of 88.45 m and a median range value of 81.9 m (Figure 3.4, right). Representative ranges of 403.9, 30.57, and 88.45 meters corresponded to a sensor density of 1.95, 340.6 and 40.68 per square kilometer (Table 3.2).

Holding alpha (α = 0.05) and the effect size constant (*E* = 1 dB), representative range increased 30% from 88.45 m to 115.41 m by decreasing beta from 0.90 to 0.70 (Figure 3.5). This increase in representative range was smaller than the standard deviation of independently calculated representative ranges (α = 0.05, β = 0.90) for each sampling grid (σ = 36.17 sensors, n = 57). If beta is held constant at a conservative value (β = 0.90), and alpha increased from 0.05 to 0.1, and the representative range increased from 88.45 m to 97.98 m (Figure 3.5).

3.3.1.3. Relative Standard Interpolation Error

Interpolating point measurements of fish density over any representative range introduced interpolation errors (Figure 3.6). The absolute interpolation error, analogous to the standard deviation surrounding the interpolated estimate, is 2.93 dB at the shortest representative range, 30.57 m. Given that decibels is a logarithmic scale, an error of +/- 2.93 dB equates to a 96% increase or a 49.93% decrease in fish density at the interpolated point. The next smallest representative range, calculated from the power analysis, resulted in an interpolation error of 3.44 dB (+120% or -54.7%) at a range of 84.45 m. The interpolation error stabilized and asymptotically approached the average standard deviation, 4.32 dB. Differences in interpolation error between the larger two representative ranges, 285.65 m and 403.9 m, were proportionately smaller compared to the interpolation error at shorter representative ranges. At 285.65 m, the absolute interpolation error was 4.16 dB (+160.6% or -61.6%), compared to 4.27 dB (+167.3% or -62.6%) at 403.9 m.

Areal interpolation errors increased following a power function with a fractional exponent (Figure 3.7). The absolute error when estimating the density of fish over an area defined by a representative range of 30.57 meters (2.9×10^{-3} km^2) was 2.4 dB (+73.8% to -42.5%), compared to an error of 3.69 dB (+133.88% or -57.24%) over an area defined by a range of 88.45 meters. The interpolation error increased to 6.37 dB (+333.5% to -76.9%) within the area defined by a radius of 285.65 meters and 7.53 dB (+466.2% to -82.3%) at a range of 403.9 m.

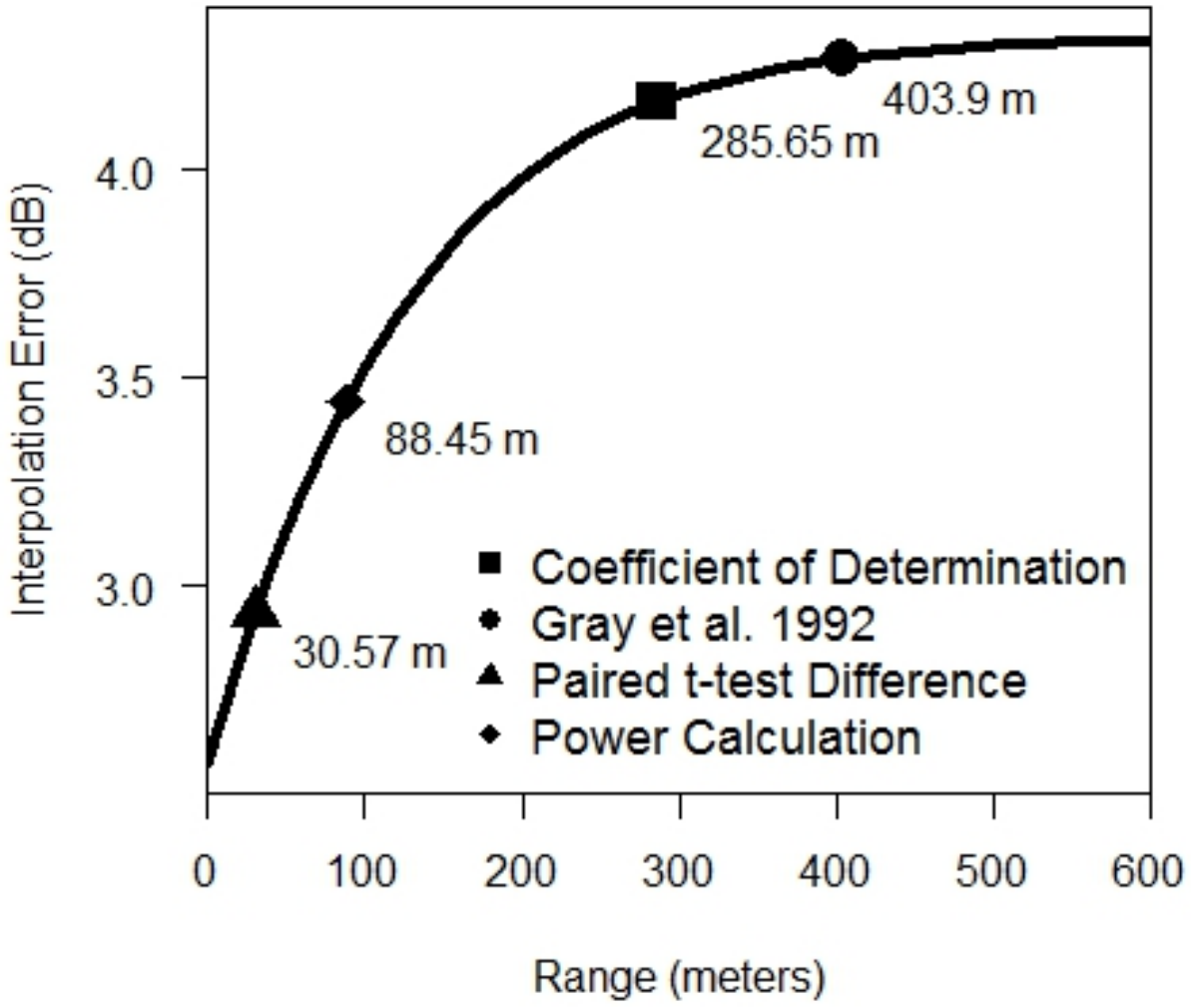

Figure 3.6. The error introduced by interpolating point measurements to spatially discreet points. The four representative ranges of the mean are marked along the curve.

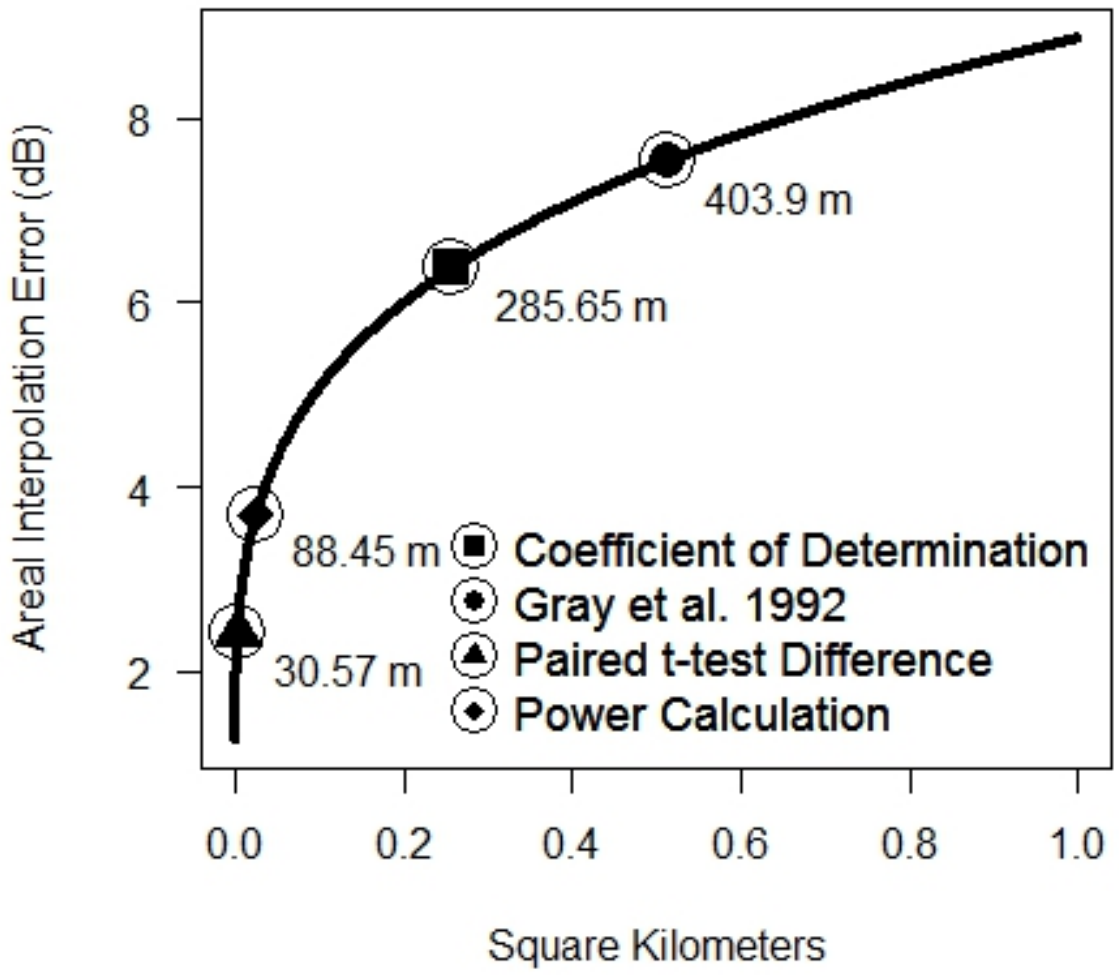

Figure 3.7. The error introduced by aerially interpolating point measurements to spatially discreet points through space. The four representative ranges of the mean, corresponding to the area of the circle defined by its radius, are marked along the curve.

3.3.2. Representative Range of the Variance

3.3.2.1. Theoretical Spectra

The relative variance modeled from the first order autocorrelation of fish densities asymptotically approached a maximum value of 4.98 times the white noise variance over infinite periods. The scale at which 95% of the maximum variance, 4.74, was measured is considered the representative scale of the variance. The relative variance exceeded the 95% maximum threshold at a period of 1,338 m (Figure 3.8, Table 3.2). Data analyzed over larger periods than 1,338 m would see negligible increases in variance.

3.3.2.2. Equivalent Periods of Spatial and Temporal Variance

As expected, both spatial and temporal spectral power increased with period (Figure 3.9). The spatial and temporal spectra had a near identical *y*-intercept (0.34 and 0.33 $\log_{10}(dB^2)$), strengthening the argument that the spatial and temporal grains were comparable. Since there is no relationship between spatial and temporal units, it is not possible to statistically test differences between the two spectra. Ordinate units were set relative to the 20m and 1.2 second grain of the spatial and temporal surveys. At these resolutions, the spatial spectra (Y = 0.34 + 0.777X) increased more rapidly than the temporal spectra (Y = 0.33 + 0.478X). The modeled maximum temporal variance at the Nyquist frequency, equivalent to a period of six-minutes, was 1.51 $\log_{10}(dB^2)$. The corresponding spatial variability was observed at a period of 648.71 meters. Anecdotally, an approximately equal amount of variance was seen within the 547 spatial and 360 temporal spectra, as denoted by the standard deviation envelopes in Figure (3.9).

3.3.3. Summary of Representative Ranges

The representative spatial range of static temporal sensors is dependent on the quantity measured, the derivation method, and associated assumptions. Six methods were used to quantify the tradeoff between sensor density and statistical precision. The representative range of the mean fish density was 30.57 m, 88.45 m, 285.65 m, or 403.9 m depending on the analytic method. The representative range of the variance was estimated at 648.7 m and 1,388.1 m (Table 3.2). Converting the representative radii of the means to areas and assuming complete spatial coverage of a static network translated to 340.61, 40.68, 3.90, or 1.95 sensors per square

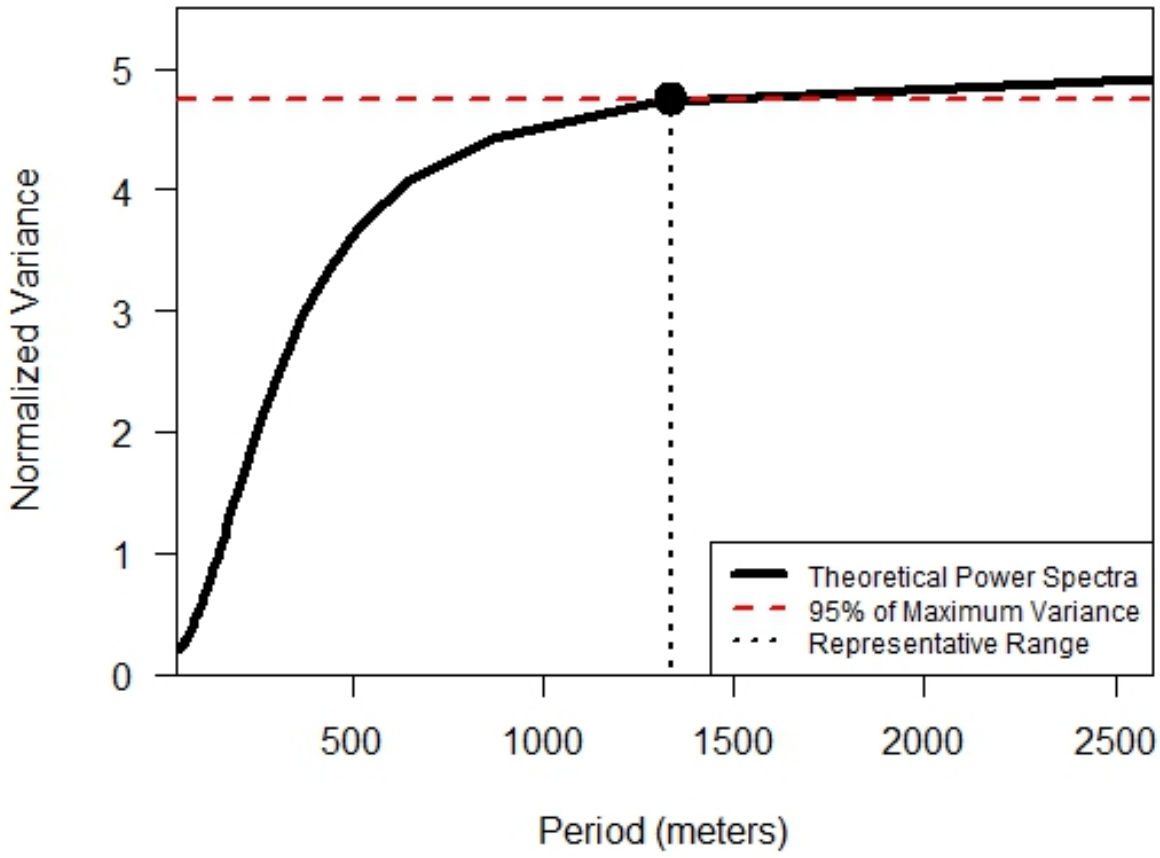

Figure 3.8. The theoretical power spectra of fish density modeled from the first order auto-regressive function. The period at which the expected variance reaches 95% of the maximum expected variance is considered the representative range of the variance.

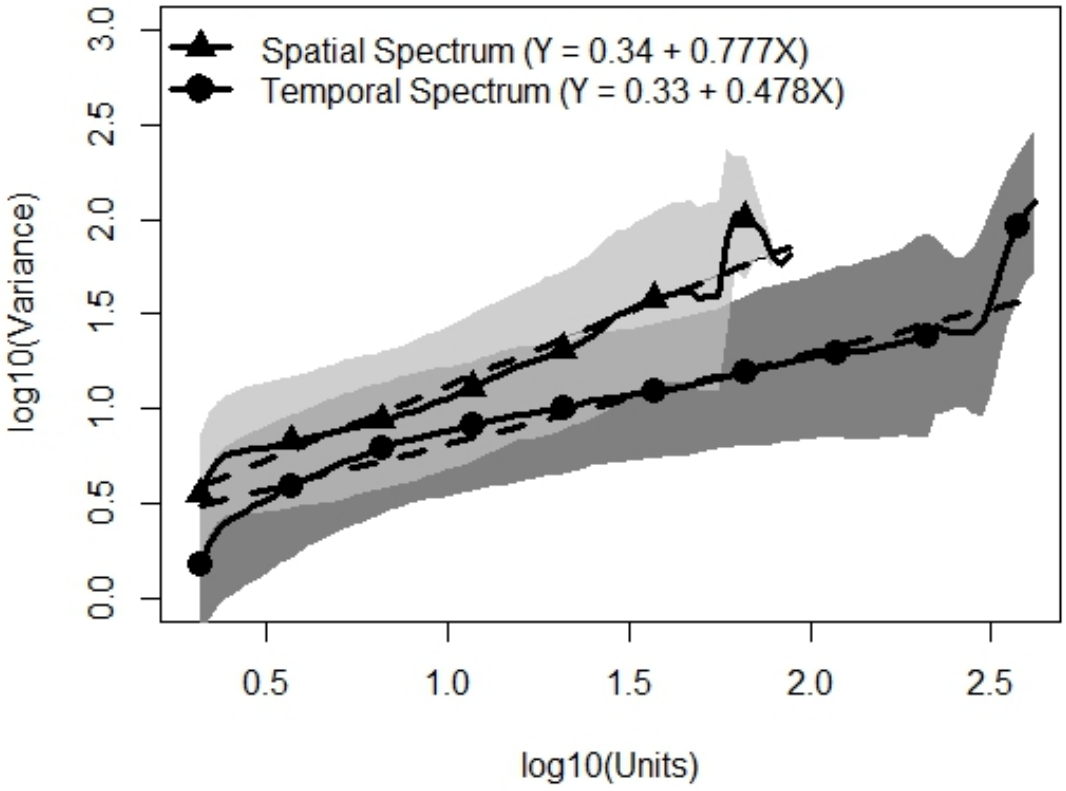

Figure 3.9. Corresponding spatial and temporal power, calculated from the global wavelet spectrum. Spatial and temporal units are 20 m and 1.2 sec, respectively. The spatial period at which we expect to observe identical magnitudes of variance as the maximum temporal period is the scale to which the variance can be considered representative.

Table 3.2. Representative range of a point measurement of fish density in Admiralty Inlet, WA calculated from each of the six examined methods.

Method	Representative Range (meters)	Devices per km^2	Estimated Cost/km^2
Coefficient of Determination Model	288.65	3.90	$292,500
Gray's Sample Size Calculation	403.90	1.95	$146,250
t-test Sample Size Calculation	30.57	340.61	$25.5 million
Power Analysis	88.45	40.68	$3.0 million
Theoretical Spectra	1,388.10	0.015	$1,125
Corresponding Spatial and Temporal Scales	648.70	0.75	$56,250

kilometer. Sensor densities measuring the mean were higher than those needed to monitor the variance, which required 0.75 and 0.015 sensors per square kilometer, suggesting that networks established to measure the mean of a quantity will have adequate spatial coverage to also characterize the variance.

3.4. Discussion

3.4.1. Biological Monitoring at MHK sites

Marine hydrokinetic energy is an emerging industry that is striving to become cost competitive with traditional electricity production. Environmental monitoring programs at MHK sites represent a large portion of pilot site development budgets (*e.g.* NYSERDA 2011), and, if initial sampling is not reduced, will contribute to both operating and decommissioning costs during the life cycle of all projects. Goals of environmental monitoring at MHK sites are to be both efficient and cost effective. Sensor networks are assumed to be more cost effective for ongoing monitoring compared to repeated mobile surveys due to the cost of labor, fuel, and vessel operation. Still, the cost of static monitoring networks may be inflated by the environmental precautionary principle (Underwood 1997, Underwood & Chapman 2003), where any error in survey design or judgment should be made in favor of environmental protection. Uncertainty surrounding the required density of sensors in a static monitoring network potentially inflates the cost of implementation for capital limited, fledgling industries. Quantifying the representative range and the error introduced through spatial interpolation removes uncertainty from the network design, which will ultimately save resources. Depending on the spatial extent of the network and the cost of purchasing, deploying, retrieving, and analyzing data from each sensor, the representative ranges estimated in this study represent significant cost savings compared to the *ad hoc* network designs of current MHK biological monitoring programs.

The density of monitoring sensors at MHK sites also has implications for the economic feasibility of developing MHK pilot sites. The estimated cost of purchasing, deploying, and retrieving an acoustic sensor is approximately $75,000 (J.K. Horne 2014 *personal communication*, NYSERDA 2011, Verdant Power 2010a). The proposed Admiralty Inlet tidal turbine site covers 0.09 square kilometers, which would require 31 sensor packages using the

most conservative paired *t*-test sample approach, 4 using the power analysis, and 1 using Gray et al.'s (1992) calculations and Anttila et al.'s (2008) coefficient of determination models. This range of instrument densities represents a cost difference of over $2.25 million. To put these numbers into perspective, the Roosevelt Island Tidal Energy project in East River New York deployed an array of 24 acoustic transducers (NYSERDA 2011) to monitor a 0.086 square kilometer site (FERC 2012) as one component of a $2.35 million monitoring plan that also costs $340,000 annually for maintenance and operation (Verdant Power 2010b). This instrument density converts to a representative range of 33.77 m, consistent with the most conservative representative range calculated in this study. Monitoring program costs among surveys designed with different representative ranges will be further exaggerated when pilot programs are scaled to larger commercial domains. Based on calculations from Admiralty Inlet, a monitoring network with complete spatial coverage designed to measure mean fish density within a one square kilometer commercial installation would cost $2.575 million, $1.7 million, $300,000, or $150,000 depending on the method chosen to calculate representative range. Networks measuring the variance of fish density at the same site would require one sensor package at a cost of $75,000.

3.4.2. Comparison of Methods

The principal objective of most monitoring networks is to detect and quantify change through space or time relative to baseline conditions at a location or time prior to any perturbation. The only method included in this study that identifies the statistical power of a network to detect change is the repeated measures ANOVA power analysis. If quantifying statistical power is a monitoring program objective, then power analysis is the best method for the design of monitoring sensor networks. In practice, site-specific sampling programs incorporating control sites and stratified paired sensors will result in a higher statistical power than the paired *t*-test power calculation presented here (Skalski & McKenzie 1982, Underwood 1991, Underwood 1994).

The six methods used to calculate representative range varied in their assumptions and results. Four techniques examined the representative range of point measures estimating the mean, and the remaining two measured the representative period of the variance (Table 3.1).

The final method used spatial autocorrelation to identify the range at which measurements became statistically independent, assuming that the range at which spatial autocorrelation approaches zero is the range at which measurements become statistically independent. Spatial autocorrelation is dependent on the location, resolution, and spatial extent of the data (Ciach & Krajewski 2006, Ciannelli et al. 2008). In ecosystems where variance increases with spatial extent (Wiens 1989), such as those with spatial drift or a gradient, the representative range will increase as the survey area is expanded. The domain of a network must be delineated before the representative range can be used for network design.

The matching of temporal to spatial variance scales assumes that spatial and temporal variances are equivalent. Links between spatial and temporal periods of physical and temporal processes have been demonstrated (*e.g.* NASA 1988, Steele et al. 1994, Wu 1999). Wiens (1989) noted that long-term studies conducted over small spatial scales have low predictive power, whereas studies covering large spatial extents over short temporal periods have high pseudo-predictability because repeated samples were distributed in close temporal proximity. While Wiens (1989) emphasized the importance of analyzing spatiotemporal data at equivalent spatial and temporal scales, he lamented that there was no method to define them. Defining the relationship between spatial and temporal variance spectra provides that function.

The six methods used to estimate representative ranges are not exhaustive, but represent techniques available for *a priori* network design using data from baseline mobile surveys. *A posteriori* methods to optimize the density of established networks exist (*e.g.* Sulkava et al. 2011), but are limited to network optimization as opposed to initial design. These *a posteriori* methods are beyond the scope of this study, but should be used after a network is operational to test network performance and to optimize the spatial allocation of sampling effort. Janis and Robeson (2004) identify instances when a network could not be considered representative based on the magnitude of variability operating below the network grain (*i.e.* analogous to the nugget effect). Sulkava et al. (2011) proposed a framework for the optimization of existing static networks using k++ cluster analysis.

3.4.3. Optimizing Network Design for Monitoring Method

Network design will always include subjective choices including the minimum detectable effect, allowed sampling or interpolation error, and acceptable rate of Type I or Type II errors. Current sensor networks for MHK monitoring programs are typically designed using resource or logistic constraints (*e.g.* NYSERDA 2011), without attention to the statistical repercussions. The layout and spacing of sensor packages in monitoring networks should not be determined by resource budgets, but by the sampling required to meet the network's design objectives. The purpose of examining representative range methods was not to eliminate decision-making, but to modularize network design in a series of decisions based on network objectives. The first decision is to choose a quantity or quantities that can be used to detect change (*e.g.* fish density; Figure 3.10). Once a quantity of interest is chosen, then a representative metric must be identified to index that quantity through time (*e.g.* mean S_v). This metric may be the quantity itself or a derived metric that a sensor is capable of measuring. Once the metric is identified, the property of the metric (*e.g.* mean or variance) needs to be chosen. Historically, declines in the mean of quantities, such as density or biodiversity, have been associated with negative biological effects, and provide a focus to monitoring plans (Green 1979). Changes in the variance of ecological quantities may affect the health and stability of ecosystems (Underwood 1991, Schindler et al. 2010), making the variance of ecological quantities pertinent metrics of change.

All six methods predicted different representative spatial ranges, so the choice of method must match the objective and metric used to identify change in a monitored quantity. If the network objective is to measure spatial variance, then the theoretical spatial spectra should be used to place sensors at the spatial interval that will maximize observed variance. If the network objective is to interpolate the temporal variability of a metric over space, then equivalent periods of variance should be used. The major difference between mean and variance methods is that the variance methods identify the period at which variance measurements can be considered equivalent, neither variance method calculates statistical power.

If the mean of a quantity is the principle concern, then several methods are available to describe changes in the mean through time and space. These methods include random sampling

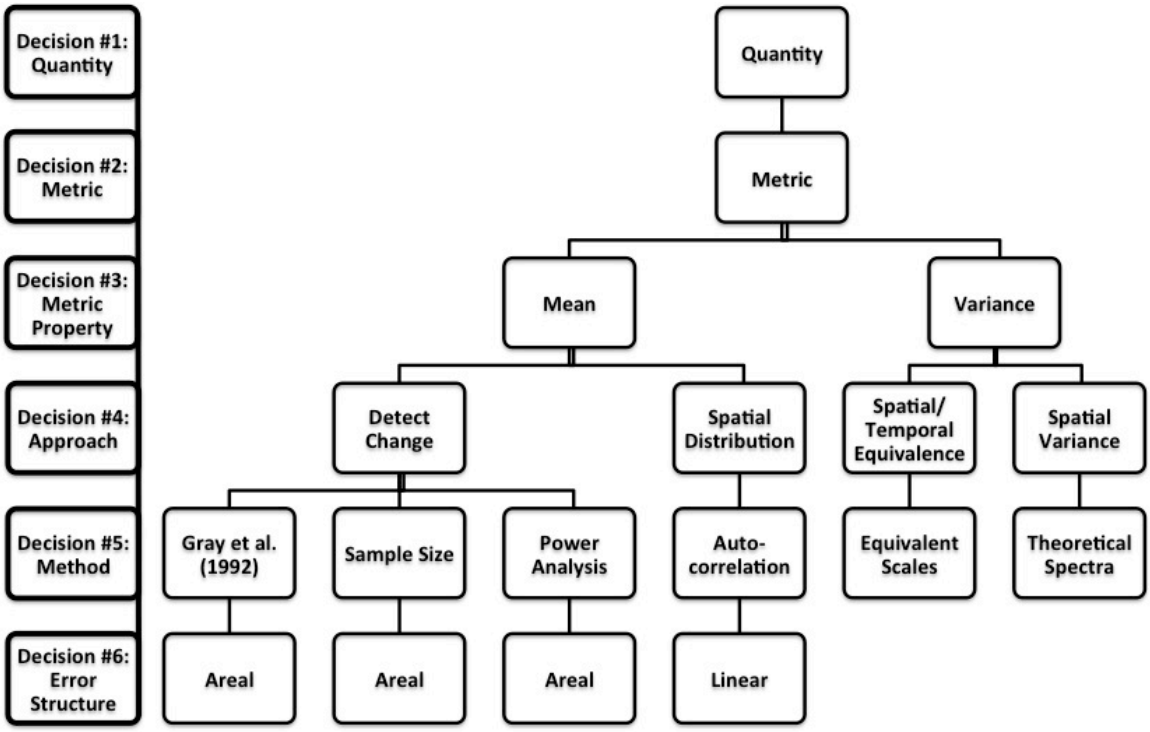

Figure 3.10. Hierarchal decision tree to simplify static sensor network planning, progressing from identification of the focal quantity to identifying the error formula to quantify network uncertainty introduced by interpolating between sensors.

to identify change, and spatial autocorrelation to describe how the distribution of a quantity varies through space. If the detection of change in a quantity is the objective (*i.e*. did this quantity change after perturbation), then ANOVA sampling size calculations should be considered in the network design. ANOVA-based random sampling approaches quantify the number of sensors required to detect a change assuming a repeated-measures sampling design that compares differences between pre- and post-perturbation measurements. The density of monitoring instruments is estimated as the quotient of the domain divided by the number of sensors. If the goal of a network is to identify a change, the most appropriate of the three random sampling methods examined in this study is the power analysis method, which includes decisions about the statistical power, resolvable effect size, and prevalence of false positives. The ANOVA-based random sampling methods sample from the entire spatial domain, and thus are testing the significance of change across the entire domain. Given that interpolating point measurements across a domain will introduce interpolation error, any statements about the quantity across the domain should include estimates of aerial interpolation error to convey uncertainty surrounding the monitored quantity.

If spatial modeling of a quantity at every point through the domain is a design objective (*e.g.* modeling species' spatial distributions), then the spatial autocorrelation approach should be used. Spatial autocorrelation directly quantifies spacing between sensors, which can then be used to calculate the total number of sensors for a specified domain. Either the lagged correlation coefficient or lagged coefficient of determination can be used as a metric of representative range, but a threshold of what constitutes "representative" needs to be established for either metric. The coefficient of determination is recommended as a representative metric due to its straightforward interpretation as the proportion of explained variance. Unlike previous studies that used a significant deviation from a perfect correlation as a benchmark for representative range (Jacobs 1988), this study used the range at which observations became statistically independent as the representative range. Once the representative range is quantified, interpolation error at any point can be estimated as a function of range to increase the understanding of uncertainty in spatial models.

Nekton vertical distributions changed as a function of environmental covariates, and it is reasonable to assume that horizontal distributions and representative ranges may also be influenced. Preliminary analysis demonstrated that nekton densities were autocorrelated over greater distances during slack tides, increasing the representative range of the echosounder. This increase may be due to changes in horizontal distribution of nekton over a tidal cycle. An alternative explanation is that tidal currents add a layer of confounding variability to spatially-indexed data as a ship samples through space. A mobile survey makes the assumption that measurements are instantaneous, ostensibly assuming that temporal variability does not alter the underlying distribution in the time it takes to sample space. Tidal currents potentially add variability, as nekton are transported with tidal currents. This convolving of time and space confound mobile observations of spatial variability and autocorrelation at any instance in time. Given that nekton flux with tidal currents vary through time, an unknown bias is added to the autocorrelation in density measurements through time. This bias cannot be corrected from measurements of tidal velocity from an ADCP, as fish and macrozooplankton are not passive particles that drift freely in the tidal currents. The net result is that tidal currents may influence the horizontal distribution of nekton, which alters the representative range of a stationary sensor, and spatial autocorrelation measurements may be negatively biased by tidal currents. There is no way to distinguish between the two sources of bias in this survey. The influence of tidal currents on representative range estimates may be an interesting point of future research.

This study provides an approach to design a monitoring network using a set of objective decisions. The six methods included in the approach were compared using fish density data from a MHK pilot site, but this approach can be applied to the design of any bio-physical sensor network. Distributed sensor networks are increasingly used to collect high-scope, spatiotemporal data to quantify ecological pattern and to aid in the understanding of processes influencing observed patterns across ranges of spatial and temporal scales (Porter et al. 2005). Optimizing these networks to meet their design objectives will manage network expectations, increase network performance, increase the cost-effectiveness of distributed networks, and simplify network design. Most importantly, this study provides the tools for ecologists to quantify error

introduced by spatially interpolating point measurements, and document the rationale used to determine the density of sensors in distributed monitoring networks.

Chapter 4: Summary & Conclusions

4.1. Summary & Conclusions

This thesis used data from the proposed Admiralty Inlet tidal MHK site to characterize nekton distributions, compare acoustic technologies, and to propose a framework for nekton domain monitoring. Assuming stationary acoustic surveys will be used for long-term monitoring, this framework modularized the design of domain monitoring programs into informed decisions about objectives, monitoring metrics, instrumentation, and the number of sampling instruments needed.

Nekton density, vertical location, dispersion, and aggregation were chosen as biologically pertinent quantities to characterize pelagic nekton density distributions. Four acoustically derived metrics, mean S_v, center of mass, inertia, and aggregation index, were used to measure these four quantities through time and space. Pre-installation measurements of these four metrics provide a baseline to compare with post-installation measurements to gauge the effects of a MHK device installation and operation. Effects on the physical environment are easier to predict than ecological effects because ecological functions and trophic relationships are more complex than physical (Ward 1978), making the monitoring of biological quantities more important to identify unexpected biological effects. Changes in metric values could represent ecological effects on the system. Decreases in the density of nekton potentially reflects a deleterious effect of a turbine on local nekton, by repulsion or injury (Osenberg & Schmitt 1996), and changes in the density of predators or prey can propagate to other trophic levels (Ward 1978, Frank 2005). Changes in the density, patchiness, or vertical distribution of nekton may alter foraging behavior or efficiency (Wellenreuther & Connel 2002), especially in turbulent environments (Pitchford et al. 2003). In this context, domain monitoring has the capability to identify ecologically significant changes in the distribution of nekton that may not be visible to near-field monitoring, which concentrate on identifying direct strikes or impingement (Viehman & Zydlewski 2014).

Of the available acoustic technologies, the calibrated scientific echosounder was found to be robust to tidal currents and more sensitive to identify patterns in nekton distributions. Although ADCP and acoustic cameras may be opportunistically available for pelagic monitoring, neither had the sensitivity to resolve temporal patterns observed by the echosounder. Simultaneous

measurements of nekton density and vertical distribution by the echosounder and ADCP or acoustic camera were weakly correlated (*i.e.* R^2 ranging from < 0.0001 to 0.029; Table 2.5 & 2.6). This result was not completely unexpected as these instruments were deployed approximately 200 m apart. Given the autocorrelation decay with distance (*c.f.* Figure 3.3 bottom), concurrent measurements separated by 200 m are expected to demonstrate a correlation (*i.e.* coefficient of determination) of 0.063. Still, the ADCP and acoustic camera did not have the sensitivity to resolve well-established nekton vertical migrations, measured smaller variability magnitudes in covariates when compared to the echosounder. Of the acoustic technologies compared, a scientific echosounder is the only instrument suitable for domain monitoring of pelagic nekton.

The baseline study examining nekton density and vertical distribution was conducted for 30 days. In the future, parallel post-installation measurements can be compared to this baseline to quantify a turbine's impact on the local nekton population. Statistical comparisons of pre- and post installation measurements require knowledge of the natural variance of the nekton community. Wavelet analysis and MARSS models quantitatively described periodicities in monitoring metrics through time. Quantifying periodic variance using time series models provided understanding of the ecosystem, and an increased ability to detect and potentially predict ecological change (Ward 1978). In this case study, nekton moved lower in the water column and became less dispersed in strong tidal currents, increasing the expected mean rate of interactions between an organism and a device during periods of peak energy production. In contrast, the variance of nekton density spiked during the neap tide. Assuming that episodic volatile periods have a higher probability of deleterious interactions, the risk of extreme encounters between nekton and a device is maximized during neap tides. Knowledge of nekton variability and estimates of risk can be used in the design of a a monitoring plan to increase monitoring effort during high-risk periods to increase the statistical power to detect and identify biological effects (Lindenmayer & Likens 2009).

A major challenge in designing environmental monitoring programs is determining the appropriate number of sensors needed to monitor a site. *A priori* estimates of stationary sensor density require knowledge of spatial variability and autocorrelation, which can be acquired from a

mobile baseline survey. Six techniques were compared to calculate the required density of stationary instruments depending on the monitored quantity (*i.e.* changes in the mean or variance), and the objective of the monitoring program. Using this approach, MHK regulators can identify the appropriate representative range needed to meet the monitoring objectives and determine the density of instruments for a given domain. Consistent with the precautionary principle (Underwood 1997), we found that a pilot turbine site in East River, NY (*c.f.* NYSERDA 2011) deployed a sensor density consistent with the most conservative representative range calculated using data from the turbine site at Admiralty Inlet, WA (33.78 m at the NY site compared to 30.57 m at the WA site). A representative range of 30.57 m is equivalent to deploying 340.61 sensors per square kilometer. But given the objective of most monitoring networks to detect change, this study shows that a sensor density less than 12% of this estimate (*i.e.* 40.68 sensors per kilometer) is predicted to detect a 1 dB change in nekton density with 90% power. Using a baseline mobile survey to quantitatively determine the density of monitoring sensors keeps the monitoring network in Goldi-locks zone, balancing statistically rigorous monitoring standards in the most cost-effective manner possible. To ensure an effective and efficient monitoring program over the duration of a MHK site lifecycle (approval, installation, operation, decommissioning), a mobile baseline study is a critical component that adds statistical power and financial value to all mandated monitoring programs.

Extending this work beyond the design of a monitoring plan, this study establishes an analytical framework built around wavelet analysis and MARSS time series models to quantify change in populations and to identify high biological risk. Assuming volatility can be used as a metric of risk, scale-averaged wavelet power can be used as a proxy for instantaneous ecological risk. Additional scrutiny or mitigation procedures can be applied in instances of heightened ecological risk, increasing the power and responsiveness of a monitoring program to potentially catastrophic events. The global wavelet spectrum can also be used to infer physical processes that have a detectable effect on nekton communities, which can then be included in MARSS time-series models. MARSS models can be used to concurrently model measurements from each stationary instrument package, so all stationary instruments can be included in model

parameterization. Concurrently modeling multiple time series adds more information to model parameterization and thus more certainty. Interpolation errors, calculated using network density derived from representative range calculations, can be used as the observation error term in MARSS models to quantify sampling uncertainty. Using MARSS models to model monitoring metric values after a device has been installed provides the ability to identify biological effects that may not be detected using simple statistical tests. To illustrate by example, Underwood (1991) proposed a series of responses to environmental perturbations, including negative discontinuities (*i.e.* precipitous decline in a quantity over a short period due to a perturbation), long-term trends, or fluctuations. Each of these responses can be included in MARSS models, and the significance of each response can be tested using likelihood ratios between models incorporating and excluding the hypothesized response.

The next logical step in developing environmental monitoring for MHK sites is to compare the statistical power of the analytic techniques used to detect changes in ecologically pertinent quantities or metrics measured by sensor networks to identify the most powerful analytical tool. In biological monitoring, detecting and identifying change is the principle objective of sensor networks, but the power or sensitivity of a program to detect change is limited by sampling design (Underwood 1994, Zhang & Zhang 2012) and the associated analytical tool used to identify it. Future research should compare the power of statistical methods to identify change in data streams from sensor networks. Statistical methods that explain or partition variability in a data stream increase statistical power in results, such as repeated measure ANOVAs (Stewart-Oaten et al. 1986, Underwood 1994, Grüss et al. 2014), autoregressive time series models (*e.g.* MARSS models; Holmes et al. 2012), or change point detection algorithms (Lund et al. 2007, Shao & Zhang 2010). ANOVA models are used to partition variability in a quantity and identify biological change using Beyond BACI studies (*i.e.* Before-After-Control-Impact; Underwood 1991, Underwood 1994, Grüss et al. 2014). Change point detection algorithms, algorithms designed to identify the point at which the mean or variance of a series change, identify instances when the mean or variance of a time series shifts after accounting for environmental covariates (Shao &

Zhange 2010), even in autocorrelated and periodic time series (Lund et al. 2007). The alignment of change points with known anthropogenic disturbances can indicate an ecological effect.

If using variance measurements as a metric for change, then discontinuities in the variance of a series coinciding with the installation or operation of a device can be detected using beyond Before-After-Control-Impact designs (Underwood 1991, Underwood 1994, Underwood & Chapman 2003), the Downton-Katz test (Downton & Katz 1993), or statistical tests to detect local volatility through time (Liu et al. 1999). Analytical simulations, simulating the sampling and analysis of a sampling field with known spatial properties, could be used to test the statistical power of each analytic method using Markov chain Monte Carlo (Hastings 1970). These simulated fields can be generated from the measurements of spatial and temporal variability of nekton collected in this study.

Finally, statistically significant deviations in monitored quantities may not equate to biologically significant effects. Small changes in a quantity of a community may be ecologically inconsequential or even beneficial to certain community constituents (Inger et al. 2009). Ultimately, it is the responsibility of governmental regulators to avoid or mitigate biologically significant effects of MHK installation and operation. Further work is needed to quantify the threshold of change that has an effect or impacts the structure or stability of components within or entire aquatic ecosystems. The minimum detectable effect size can then be compared to ecologically-derived thresholds of biological impacts to test the efficacy of monitoring thresholds, operational modification, and mitigation plans. Ultimately, the density of sensors and the variables that are measured should match the sensitivity of a monitoring network to detect ecologically significant change.

References

Anttila, S., Kairesalo, T., and Pellikka, P. 2008. A Feasible Method to Assess Inaccuracy Caused by Patchiness in Water Quality Monitoring. *Environmental Monitoring and Assessment* 142 (1): 11–22.

ABPmer. 2010. Collision Risk of Fish with Wave and Tidal Devices. ABP Marine Environmental Research Ltd. Report No. 1516, Southampton, UK.

Axenrot, T., Didrikas, T., Danielsson, C., and Hansson, S. 2004. Diel Patterns in Pelagic Fish Behaviour and Distribution Observed from a Stationary, Bottom-Mounted, and Upward-Facing Transducer. *ICES Journal of Marine Science: Journal Du Conseil* 61 (7): 1100–1104.

Babson, A.L., Kawase, M., and MacCready, P. 2006. Seasonal and Interannual Variability in the Circulation of Puget Sound, Washington: A Box Model Study. *Atmosphere-Ocean* 44 (1): 29-45.

Bachmaier, M., and Backes, M. 2008. Variogram or Semivariogram? Understanding the Variances in a Variogram. *Precision Agriculture* 9 (3): 173–175.

Banse, K. 1964. On the Vertical Distribution of Zooplankton in the Sea. *Progress in Oceanography* 2: 53–125.

Barau, A. S., and Ludin, A. N. M. 2012. Intersection of Landscape, Anthropocene and Fourth Paradigm. *Living Reviews in Landscape Research* 6 doi:10.12942/lrlr-2012-1

Bence, J.R. 1995. Analysis of Short Time Series: Correcting for Autocorrelation. *Ecology* 76 (2): 628-639.

Betz, A. 1966. Introduction to the theory of flow machines. Pergamon Press, Oxford.

Benoit-Bird, K. J., and Au, W.W.L. 2004. Diel Migration Dynamics of an Island-Associated Sound-Scattering Layer. *Deep Sea Research Part I: Oceanographic Research Papers* 51 (5): 707–19.

Boehlert, G.W., and Gill, A.B. 2010. Environmental and Ecological Effects of Ocean Renewable Energy Development: A Current Synthesis. *Oceanography* 23 (2): 68-81.

Bos, A.R., and Gumanao, G.S. 2012. The Lunar Cycle Determines Availability of Coral-Reef Fishes at Fish Markets. *Journal of Fish Biology* 81 (6): 2074–2079.

Brando, V. E., and Phinn, S. 2007. Guest Editorial: Coastal Aquatic Remote Sensing Applications for Environmental Monitoring and Management. *Journal of Applied Remote Sensing* 1(1).

Brooks, C.F. 1947. Recommended climatological networks based on the representativeness of climatic stations for different elements. *Transactions of the American Geophysical Union* 28 (6): 845-846.

Brierley, A.S., Brandon, M.A., and Watkins, J.L. 1998. An Assessment of the Utility of an Acoustic Doppler Current Profiler for Biomass Estimation. *Deep-Sea Research Part I* 45 (9): 1555–1573.

Brierley, A. S., Saunders, R.A., Bone, D.G., Murphy, E.J., Enderlein, P., Conti, S.G., and Demer, D.A. 2006. Use of Moored Acoustic Instruments to Measure Short-Term Variability in Abundance of Antarctic Krill. *Limnology and Oceanography: Methods* 4: 18–29.

Burgos, J.M., and Horne, J.K. 2007. Sensitivity Analysis and Parameter Selection for Detecting Aggregations in Acoustic Data. *ICES Journal of Marine Science: Journal Du Conseil* 64: 160–168.

Burwen, D.L., Fleischman, S.J., and Miller, J.D. 2010. Accuracy and Precision of Salmon Length Estimates Taken from DIDSON Sonar Images. *Transactions of the American Fisheries Society* 139 (5): 1306–14.

Cazelles, B., Chavez, M., Berteaux, D., Ménard, F., Vik, J.O., Jenouvrier, S., and Stenseth, N.C. 2008. Wavelet Analysis of Ecological Time Series. *Oecologia* 156 (2): 287–304.

Certain, G., Bellier, E., Planque, B., and Bretagnolle, V. 2007. Characterizing the Temporal Variability of the Spatial Distribution of Animals: An Application to Seabirds at Sea. *Ecography* 30 (5): 695–708.

Chambers, J.M., Cleveland, W.S., Kleiner, B. and Tukey, P.A. 1983. *Graphical Methods for Data Analysis.* Wadsworth & Brooks/Cole, Belmont, California.

Ciach, G. J., and Krajewski, W.F. 2006. Analysis and Modeling of Spatial Correlation Structure in Small-scale Rainfall in Central Oklahoma. *Advances in Water Resources* 29 (10): 1450–1463.

Ciannelli, L., Fauchald, P., Chan, K.S., Agostini, V.N., and Dingsør, G.E. 2008. Spatial Fisheries Ecology: Recent Progress and Future Prospects. *Journal of Marine Systems* 71 (3-4): 223–236.

Cochrane, N.A., Sameoto, D.D., and Belliveau, D.J. 1994. Temporal Variability of Euphausiid Concentrations in a Nova-Scotia Shelf Basin Using a Bottom-Mounted Acoustic Doppler Current Profiler. *Marine Ecology Progress Series* 107 (1-2): 55–66.

Damian, D., Sampson, P.D., and Guttorp, P. 2003. Variance Modeling for Nonstationary Spatial Processes with Temporal Replications. *Journal of Geophysical Research: Atmospheres (1984–2012)* 108 (D24).

DeLacy, A.C., Miller, B.S., and Borton, S.F. 1972. Checklist of Puget Sound Fishes. Seattle, WA: University of Washington Division of Marine Resources.

Denman, K.L. 1975. Spectral Analysis: A Summary of the Theory and Techniques. Fisheries and Marine Service Technical Report 539. Marine Ecology Laboratory, Bedford Institute of Oceanography, Dartmouth, Nova Scotia.

Dickey, T.D., and Bidigare, R.R. 2005. Interdisciplinary Oceanographic Observations: The Wave of the Future. *Scientia Marina* 69 (S1): 23–42.

Doksæter, L., Godø, O.R., Olsen, E., Nøttestad, L., and Patel, R. 2009. Ecological Studies of Marine Mammals Using a Seabed-Mounted Echosounder. *ICES Journal of Marine Science: Journal Du Conseil* 66 (6): 1029–36.

Downton, M.W., and Katz, R.W. 1993. A Test for Inhomogeneous Variance in Time-averaged Temperature Data. *Journal of Climate* 6: 2448-2464.

Fairweather, P. G. 1991. Statistical Power and Design Requirements for Environmental Monitoring. *Marine and Freshwater Research* 42 (5): 555–567.

FERC (Federal Energy Regulatory Commission). 2008. Licensing Hydrokinetic Pilot Projects. Retrieved from: www.FERC.gov. April 14th, 2008.

FERC (Federal Energy Regulatory Commission). 2012. Order Issuing Pilot Project License: Verdant Power, LLC. Project No. 12611-005.

FERC (Federal Energy Regulatory Commission). 2014. Order Issuing Pilot Project License: Public Utility District No. 1 of Snohomish County, Washington. Project No. 12690-005.

Flagg, C.N., Wirick, C.D., and Smith, S.L. 1994. The Interaction of Phytoplankton, Zooplankton and Currents from 15 Months of Continuous Data in the Mid-Atlantic Bight. *Deep Sea Research Part II: Topical Studies in Oceanography* 41 (2): 411–35.

Foote, K.G. 1983. Linearity of Fisheries Acoustics, with Addition Theorems. *The Journal of the Acoustical Society of America* 73 (6): 1932–1940.

Foote, K.G., Knudsen, H.P., Vestnes, G., MacLennan, D.N., and Simmonds, E.J. 1987. Calibration of Acoustic Instruments for Fish Density Estimation: A Practical Guide. *ICES CRR No. 144 ICES CRR* No. 144.

Francois, R.E., and Garrison, G.R. 1982. Sound Absorption Based on Ocean Measurements Part II: Boric Acid Contributions and Equation for Total Absorption. *Journal of Acoustical Society of America* 72: 1879-1890.

Frank, K. T. 2005. Trophic Cascades in a Formerly Cod-Dominated Ecosystem. *Science* 308(5728), 1621–1623.

Frid, C., Andonegi, E., Depestele, J., Judd, A., Rihan, D., Rogers, S.I., and Kenchington, E. 2012. The Environmental Interactions of Tidal and Wave Energy Generation Devices. *Environmental Impact Assessment Review* 32 (1): 133–39.

Gandin, L.S. 1970. The Planning of Meteorological Station Networks. World Meteorological Organization Technical Note No. 111, Geneva, 35pp.

Garcillán, P.P. and Ezcurra, E. 2003. Biogeographic regions and ß-diversity of woody dryland legumes in the Baja California peninsula. *Journal of Vegetation Science* 14: 859-868.

Gilman, D.L., Fuglister, F.J., and Mitchell JR., J.M. 1962. On the Power Spectrum of “Red Noise”. *Journal of Atmospheric Sciences* 20:182-184.

Gooch, S. Thomson, J., Polagye, B., and Meggitt, D. 2009. Site Characterization for Tidal Power. Oceans 2009, MTS/IEEE Biloxi – Marine Technology for Our Future: Global and Local Challenges. pp. 10.

Gray, J.S., McIntyre, A.D., and Stirn, J. 1992. *Biological assessment of marine pollution – with particular reference to benthos*. FAO Technical Paper No. 324: Manual of Methods in Aquatic Environment Research. Rome.

Green, R.H. 1979. Sampling Design and Statistical Methods for Environmental Biologists. Wiley: Chichester.

Gringarten, E, and Deutsch, C.V. 2001. Teacher’s Aide Variogram Interpretation and Modeling. *Mathematical Geology* 33 (4): 507–534.

Gruss, A., Robinson, J., Heppell, S. S., Heppell, S. A., and Semmens, B. X. 2014. Conservation and fisheries effects of spawning aggregation marine protected areas: What we know, where we should go, and what we need to get there. *ICES Journal of Marine Science*. doi:10.1093/icesjms/fsu038

Halvorsen, M.B., Casper, B.M., Woodley, C.M., Carlson, T.J., and Popper, A.N. 2012. Threshold for Onset of Injury in Chinook Salmon from Exposure to Impulsive Pile Driving Sounds. *PLoS ONE* 7 (6): e38968.

Hastings, W.K. 1970. Monte Carlo Sampling Methods Using Markov Chains and Their Applications. *Biometrika* 57(1): 97-109.

Haury, L. R., McGowan J.A., and Wiebe, P.H. 1978. Patterns and Processes in the Timespace Scales of Plankton Distributions. In Steele, J.H. (eds), *Nato Conference Marine 03*, 277–327. Plenum Press, New York.

Hershfield, D.M. 1965. On the Spacing of Raingauges. Symposium Design of Hydrological Networks no. 67 of I.A.S.H.

Hewitt, J. E., Thrush, S.E., and Cummings, V.J. 2001. Assessing Environmental Impacts: Effects of Spatial and Temporal Variability at Likely Impact Scales. *Ecological Applications* 11 (5): 1502–16.

Hocke, K., and Kämpfer, N. 2011. Hovmöller Diagrams of Climate Anomalies in NCEP/NCAR Reanalysis from 1948 to 2009. *Climate Dynamics* 36 (1-2): 355–364.

Hoffman, F. M., Kumar, J., Mills, R. T., and Hargrove, W. W. 2013. Representativeness-based sampling network design for the State of Alaska. *Landscape Ecology* 28(8): 1567–1586.

Holmes, E.E., Ward, E.J., and Wills, K. 2012. MARSS: Multivariate Autoregressive State-Space Models for Analyzing Time-Series Data. *The R Journal* 4: 11–19.

Horne, J. K., and Schneider, D.C. 1995. Spatial Variance in Ecology. *Oikos* 74 (1): 18–26.

Hovmöller, E. 1949. The Trough-and-Ridge Diagram. *Tellus* 1 (2): 62–66.

Hubbell, S.P. 2001. The Unified Neutral Theory of Biodiversity and Biogeography. Princeton University Press.

Hudgins, L., Friehe, C.A., and Mayer, M.E. 1993. Wavelet Transforms and Atmospheric Turbulence. *Physical Review Letters* 71: 3279-3282.

Huff, F.A., and Neill, J.C. 1957. Rainfall Relations on Small Areas in Illinois. *Bulletin of Illinois State Water Service no. 44.*

Hutchinson, P. 1972. Comment on 'The Relative Efficiency of the Density of Rain-gauge Networks, *Journal of Hydrology* 17 (3): 243–246.

Inger, R., Attrill, M.J., Bearhop, S., Broderick, A.C., Grecian, W.J., Hodgson, D.J., Mills, C., et al. 2009. Marine Renewable Energy: Potential Benefits to Biodiversity? An Urgent Call for Research. *Journal of Applied Ecology* 46: 1145-1153.

Jacobs, J.D. 1989. Spatial Representativeness of Climatic Data from Baffin Island, NWT, with Implications for Muskoxen and Caribou Distribution. *Arctic* 42 (1): 50–56.

Janis, M., and Robeson, S. 2004. Determining the Spatial Representativeness of Air-Temperature Records Using Variogram-Nugget Time Series. *Physical Geography* 25 (6): 513–530.

Kaartvedt, S., Røstad, A., Klevjer, T.A., and Staby, A. 2009. Use of Bottom-Mounted Echo Sounders in Exploring Behavior of Mesopelagic Fishes. *Marine Ecology Progress Series* 395: 109–18.

Kagan, R.L. 1966. An Evaluation of Representativeness of Precipitation Data. Works of the Main Geophysical Observatory. USSR. Vol. 191.

Kagan, R.L. 1972. Precipitation – Statistical Principles. In WMO Publication No. 324: The Casebook on Hydrological Network Design Practice. World Meteorological Organization, Geneva.

Kitsiou, D., Tsirtsis, G., and Karydis, M. 2001. Developing an Optimal Sampling Design. A Case Study in a Coastal Marine Ecosystem. *Environmental Monitoring and Assessment* 71 (1): 1–12.

Koslow, J. A. 2009. The Role of Acoustics in Ecosystem-Based Fishery Management. *ICES Journal of Marine Science: Journal Du Conseil* 66 (6): 966–73.

Landres, P.B., Morgan, P., and Swanson, F.J. 1999. Overview of the Use of Natural Variability Concepts in Managing Ecological Systems. *Ecological Applications* 9 (4): 1179.

Legendre, P. 1993. Spatial Autocorrelation: Trouble or New Paradigm? *Ecology* 74 (6): 1659.

Levin, S. 1992. Promoting the Science of Ecology. *Ecology* 73 (6): 1943–1967.

Lie, A., Kim, D., Schnetzer, A., and Caron, D.A. 2013. Small-scale Temporal and Spatial Variations in Protistan Community Composition at the San Pedro Ocean Time-series Station Off the Coast of Southern California. *Aquatic Microbial Ecology* 70 (2): 93–110.

Lindenmayer, D. B., & Likens, G. E. 2009. Adaptive monitoring: a new paradigm for long-term research and monitoring. *Trends in Ecology & Evolution* 24(9), 482–486.

Liu, Y., Gopikrishnan, P., Cizeau, P., Meyer, M., Peng, C., and Stanley, H.E. 1999. Statistical properties of the volatility of price fluctuations. *Physical Review E* 60 (2), 1390.

Liu, Y., San Liang, X., and Weisberg, R.H. 2007. Rectification of the Bias in the Wavelet Power Spectrum. *Journal of Atmospheric and Oceanic Technology* 24 (12): 2093–2102.

Love, R.H. 1971. Dorsal-Aspect Target Strength of an Individual Fish. *Journal of the Acoustical Society of America* 3 (2): 816-823.

Lund, R., Wang, X. L., Lu, Q. Q., Reeves, J., Gallagher, C., and Feng, Y. 2007. Changepoint Detection in Periodic and Autocorrelated Time Series. *Journal of Climate* 20(20), 5178–5190.

MacLennan, D. N., Fernandes, P.G., and Dalen, J. 2002. A consistent approach to definitions and symbols in fisheries acoustics. *ICES Journal of Marine Science* 59:365–369.

Mallat, S.G. 1989. A Theory for Multiresolution Signal Decomposition: The Wavelet Representation. *IEEE Transactions on Pattern Analysis and Machine Intelligence* 11 (7): 674–693.

Mapstone, B.D. 1995. Scalable Decision Rules for Environmental Impact Studies: Effect Size, Type I, and Type II Errors. *Ecological Applications* 5 (2): 401.

Martin, A. P., Zubkov, M.V., Burkill, P.H., and Holland, R.J. 2005. Extreme Spatial Variability in Marine Picoplankton and Its Consequences for Interpreting Eulerian Time-series. *Biology Letters* 1 (3): 366–369.

Milewska, E., and Hogg, W.D. 2001. Spatial Representativeness of a Long-term Climate Network in Canada. *Atmosphere-Ocean* 39 (2): 145–161.

Mønness, E. and Coleman, S. 2011. A Short Note on Variograms and Correlograms. Notat nr. 1 - 2011. Hedmark University College.

Morgan, P., Aplet, G.H., Haufler, J.B., Humphries, H.C., Moore, M.M., and Wilson, W.D. 1994. Historical Range of Variability: A Useful Tool for Evaluating Ecosystem Change. *Journal of Sustainable Forestry* 2: 87-111.

Morrisey, D.J. 1993. Environmental Impact assessment—A Review of Its Aims and Recent Developments. *Marine Pollution Bulletin* 26 (10): 540–45.

Nakken, O., and Olsen, K. 1977. Target Strength Measurements of Fish. Rapports et Proce` s-Verbaux des Re´ unions Conseil In- ternational pour l'Exploration de la Mer 170: 53-69.

NASA Advisory Council, Earth System Science Committee. 1988. Earth System Science: A Closer View. National Aeronautics and Space Administration, Washington D.C.

Neilson, J.D., and Perry, R.I. 1990. Diel Vertical Migrations of Marine Fishes: An Obligate or Facultative Process? *Advances in Marine Biology* 26: 115-168.

Nekola, J.C., and White, P.S. 1999. The Distance Decay in Biogeography and Ecology. *Journal of Biogeography* 26 (4): 867-878.

Nekola, J.C., and McGill, B.J. 2014. Scale Dependency in the Functional Form of the Distance Decay Relationship. *Ecography* 37 (4): 309–320.

NOAA. 1987. Puget Sound: Issues, Resources, Status, and Management. Proceedings of a NOAA Estuary of the Month Seminar Series No. 8. U.S. Department of Commerce, Washington D.C.

Normandeau. 2011. Effects of EMFs from Undersea Power Cables on Elasmobranchs and Other Marine Species. US Dept. of the Interior, Bureau of Ocean Energy Management, Regulation, and Enforcement, Pacific OCS Region, Camarillo, CA. OCS Study BOEMHK 2011-09. *US Department of the Interior, Bureau of Ocean Energy Management, Regulation, and Enforcement, Pacific OCS Region, Camarillo, CA. OCS Study BOEMHK* 9.

Nortek. 2001. Monitoring Sediment Concentration with Acoustic Backscattering Instruments. *Nortek Technical Note*, No. 003.

NYSERDA (New York State Energy Research and Development Authority). 2011. Roosevelt Island Tidal Energy (RITE) Environmental Assessment Project. NYSERDA 9892-1. Albany, New York.

Osenberg, C.W., Schmitt, R.J., Holbrook, S.J., Abu-Saba, K.E., and Russell Flegal, A. 1994. Detection of Environmental Impacts: Natural Variability, Effect Size, and Power Analysis. *Ecological Applications* 4 (1): 16–30.

Osenberg, C.W., and Schmitt, R.J. 1996. Detecting Ecological Impacts: Concepts and Applications in Coastal Environments. Academic Press: San Diego, CA.

Öhman, M.C., Sigray, P., and Westerberg, H. 2007. Offshore Windmills and the Effects of Electromagnetic Fields on Fish. *AMBIO: A Journal of the Human Environment* 36 (8): 630–33.

Percival, D.P. 1995. On Estimation of the Wavelet Variance. *Biometrika* 82: 619–631.

Perrier, V., Philipovitch, T., and Basdevant, C. 1995. Wavelet Spectra Compared to Fourier Spectra. *Journal of Mathematical Physics* 36: 1506–1519.

Pitchford, J. W., James, A., and Brindley, J. 2003. Optimal foraging in patchy turbulent environments. *Marine Ecology Progress Series* 256: 99–110.

Platt, T., and Denman, K.L. 1975. Spectral Analysis in Ecology. *Annual Review of Ecology and Systematics*: 189–210.

Polagye, B., Van Cleve, B., Copping, A., and Kirkendall, K. (editors). 2011. Environmental effects of tidal energy development. U.S. Department of Commerce, NOAA Technical Memo. NMFS F/SPO-116.

Polagye, B., and Thomson, J. 2013. Tidal Energy Resource Characterization: Methodology and Field Study in Admiralty Inlet, Puget Sound, WA (USA). *Proceedings of the Institution of Mechanical Engineers, Part A: Journal of Power and Energy* 227 (3): 352–67.

Porter, J., Arzberger, P., Braun, H.W., Bryant, P., Gage, S., Hansen, T., Hanson, P., Lin, C.C., Lin, F.P., Kratz, T., Michener, W., Shapiro, S., and Williams, T. 2005. Wireless Sensor Networks for Ecology. *BioScience* 55(7): 561-572.

Posadas, P., Crisci, J.V., and Katinas, L. 2006. Historical Biogeography: A Review of Its Basic Concepts and Critical Issues. *Journal of Arid Environments* 66 (3): 389–403.

Rhodes, J. R., and Jonzén, N. 2011. Monitoring Temporal Trends in Spatially Structured Populations: How Should Sampling Effort Be Allocated Between Space and Time? *Ecography* 34 (6): 1040–1048.

Rodda, J.C. 1971. Report on Precipitation. *Institute of Hydrology Report No. 11.* pp. 29.

Roughgarden, J. 1977. Patchiness in the Spatial Distribution of a Population Caused by Stochastic Fluctuations in Resources. *Oikos* 29: 52-59.

Rycroft, H.B. 1949. Random Sampling of Rainfall. *Journal of South African Forestry Society* 18: 71-81.

Sampson, P., Damian, D., and Guttorp, P. 2001. Advances in Modelling and Inference for Environmental Processes with Nonstationary Spatial Covariance. In Allard, D., Monestiez, P., Froidevaux, R. (eds), GeoENV2000: Third European Conference on Geostatistics for Environmental Applications.

Saunders, S. C., Chen, J., Drummer, T. D., Gustafson, E. J., and Brosofske, K. D. 2005. Identifying scales of pattern in ecological data: a comparison of lacunarity, spectral and wavelet analyses. *Ecological Complexity* 2(1), 87–105.

Schindler, D. E., Hilborn, R., Chasco, B., Boatright, C. P., Quinn, T. P., Rogers, L. A., and Webster, M. S. 2010. Population Diversity and the Portfolio Effect in an Exploited Species. *Nature* 465(7298), 609–612.

Schneider, D.C. 1990. Spatial Autocorrelation in Marine Birds. *Polar Research* 8: 89-97.

Schneider, D.C. 2009. Quantitative Ecology. Academic Press, London.

Shao, X., and Zhang, X. 2010. Testing for Change Points in Time Series. *Journal of the American Statistical Association* 105(491): 1228–1240.

Simmonds, J., MacLennan, D. 2005. Fisheries Acoustics: Theory and Practice. Blackwell Publishing, Oxford.

Siljamo, P., Sofiev, M., Ranta, H., Linkosalo, T., Kubin, E., Ahas, R., Genikhovich, E., Jatczak, K., Jato, V., and Neková\vr, J. (2008). Representativeness of point-wise phenological Betula data collected in different parts of Europe. *Global Ecology and Biogeography* 17(4), 489–502.

Skalski, J.R., and McKenzie, D.H. 1982. A Design for Aquatic Monitoring Programs. *Journal of Environmental Management* 14(3): 237-251.

Smith, M. P. L. 1991. Environmental Impact Assessment: The Roles of Predicting and Monitoring the Extent of Impacts. *Marine and Freshwater Research* 42 (5): 603–14.

Soininen, J., McDonald, R., and Hillebrand, H. 2007. The Distance Decay of Similarity in Ecological Communities. *Ecography* 30 (1): 3–12.

Steele, John H. 1991. Can Ecological Theory Cross the Land-sea Boundary? *Journal of Theoretical Biology* 153 (3): 425–436.

Steele, J.H., Henderson, E.W., Mangel, M., and Clark, C. 1994. Coupling Between Physical and Biological Scales [and Discussion]. *Philosophical Transactions of the Royal Society of London. Series B: Biological Sciences* 343 (1303): 5–9.

Stewart-Oaten, A., Murdoch, W.W., and Walde, S.J. 1995. Estimation of Temporal Variability in Populations. *The American Naturalist* 146 (4): 519–535.

Stommel, H. 1963. Varieties of Oceanographic Experience: The Ocean Can Be Investigated as a Hydrodynamical Phenomenon as Well as Explored Geographically. *Science* 139 (3555): 572–576.

Sulkava, M., Luyssaert, S., Zaehle, S., and Papale, D. 2011. Assessing and Improving the Representativeness of Monitoring Networks: The European Flux Tower Network Example. *Journal of Geophysical Research* 116: G00J04.

Sullivan, L. M. 2006. Estimation From Samples. *Circulation* 114 (5): 445–449.

Swanson, F.J., and Sparks, R.E. 1990. Long-term Ecological Research and the Invisible Place. *BioScience* 40 (7): 502–508.

Thiel, M., Macaya, E.C., Acuna, E., Arntz, W.E., Bastias, H., Brokordt, K., Camus, P.A. et al. 2007. The Humboldt Current System of Northern and Central Chile: Oceanographic Processes, Ecological Interactions and Socioeconomic Feedback. *Oceanography and Marine Biology* 45: 195–344.

Torrence, C., and Compo, G.P. 1998. A Practical Guide to Wavelet Analysis. *Bulletin of the American Meteorological Society* 79 (1): 61–78.

Tversky, A., and Kahneman, D. 1974. Judgment Under Uncertainty: Heuristics and Biases. *Science* 185 (4157): 1124-1131.

Underwood, A.J. 1989. The Analysis of Stress in Natural Populations. *Biological Journal of the Linnean Society* 37 (1-2): 51–78.

Underwood, A. J. 1991. Beyond BACI: Experimental Designs for Detecting Human Environmental Impacts on Temporal Variations in Natural Populations. *Marine and Freshwater Research* 42 (5): 569–587.

Underwood, A. J. 1994. On Beyond BACI: Sampling Designs That Might Reliably Detect Environmental Disturbances. *Ecological Applications* 4 (1): 4–15.

Underwood, A.J. 1997. Environmental Decision-Making and the Precautionary Principle: What Does this Principle Mean in Environmental Sampling Practice? *Landscape and urban planning* 37 (3-4): 137–146.

Underwood, A.J., and Chapman, M.G. 2003. Power, Precaution, Type II Error and Sampling Design in Assessment of Environmental Impacts. *Journal of Experimental Marine Biology and Ecology* 296 (1): 49–70.

Urmy, S. S., Horne, J.K., and Barbee, D.H. 2012. Measuring the Vertical Distributional Variability of Pelagic Fauna in Monterey Bay. *ICES Journal of Marine Science: Journal Du Conseil* 69 (2): 184–196.

Verdant Power. 2010A. Roosevelt Island Tidal Energy Project (FERC No. 12611): Final Kinetic Hydrokinetic Pilot License Application, Volume 4, Part 1 of 3. Verdant Power, LLC, New York.

Verdant Power. 2010B. Roosevelt Island Tidal Energy Project (FERC No. 12611): Final Kinetic Hydropower Pilot License Application, Volume 2, Part 2 of 2. Verdant Power, LLC, New York.

Viehman, H.A., and Zydlewski, G.B. 2014. Fish Interactions with a Commercial-Scale Tidal Energy Device in the Natural Environment. *Estuaries and Coasts.* doi: 10.1007/s12237-014-9767-8.

Walker, D.D., Loftis, J.C., and Mielke Jr, P.W. 1997. Permutation Methods for Determining the Significance of Spatial Dependence. *Mathematical Geology* 29 (8): 1011–1024.

Ward, D.V. 1978. Biological Environmental Impact Studies: Theory and Methods. Academic Press: New York.

WDFW. 2012. Species of Concern. Retrieved from http://wdfw.wa.gov/conservation/endangered/ on August 26, 2014.

Wellenreuther, M., and Connell, S. D. 2002. Response of predators to prey abundance: separating the effects of prey density and patch size. *Journal of Experimental Marine Biology and Ecology* 273(1): 61–71.

Wiens. J.A. 1976. Population Responses to Patchy Environments. *Annual Review of Ecology and Systematics* 7: 81-120.

Wiens, J. A. 1989. Spatial Scaling in Ecology. *Functional Ecology* 3 (4): 385–397.

Wilson, B. Batty, R. S., Daunt, F. and Carter, C. 2007. Collision Risks Between Marine Renewable Energy Devices and Mammals, Fish and Diving Birds. *Report to the Scottish Executive*. Scottish Association for Marine Science, Oban, Scotland, PA37 1QA.

Wilson, J.C., Elliott, M., Cutts, N.D., Mander, L., Mendão, V., Perez-Dominguez, R., and Phelps, A. 2010. Coastal and Offshore Wind Energy Generation: Is It Environmentally Benign? *Energies* 3 (7): 1383–1422.

Wu, J. 1999. Hierarchy and Scaling: Extrapolating Information Along a Scaling Ladder. *Canadian Journal of Remote Sensing* 25 (4): 367–380.

Zar, J.H. 2010. Biostatistical Analysis (5th Edition). Pearson: Upper Saddle River, New Jersey.

Zhang, J., and Zhang, C. 2012. Sampling and sampling strategies for environmental analysis. *International Journal of Environmental Analytical Chemistry* 92(4): 466–478.